INVESTIGATING OFF-RESONANCE FAT MODULATIONS IN THE TURBOSPI SIGNAL TO IMPROVE R_2* MAPPING FOR QUANTITATIVE CELL TRACKING

by

Zoë Maire Black O'Brien-Moran

Submitted in partial fulfillment of the requirements
for the degree of Master of Science

at

Dalhousie University
Halifax, Nova Scotia
December 2017

© Copyright by Zoë Maire Black O'Brien-Moran, 2017

Table of Contents

List of Tables

List of Figures

Abstract

Immune cells can be labelled with superparamagnetic iron oxide (SPIO) nanoparticles and detected *in vivo*. Tracking the migration of immune cells is valuable for understanding the immunogenic response to both cancer and cancer therapies in longitudinal studies. While many sequences are sensitive to SPIO contrast, they have limited specificity and the analysis is solely semi-quantitative.

Quantitative cell tracking is better for analyzing immune recruitment, but reports of validated quantification of SPIO labelled cells are rare. This work uses TurboSPI, a multi-echo single point imaging technique that can provide quantification through R_2* mapping at high temporal resolution. Since R_2* varies linearly with SPIO concentration, R_2* maps can be translated into maps of cell density.

TurboSPI was initially tested *in vivo* to assess cytotoxic T lymphocyte (CTL) tracking in response to immunotherapeutics. Analysis revealed that current mono-exponential R_2* fitting techniques performed poorly in the presence of fat. Off-resonance signal from fat creates modulations in the signal time course that are detrimental to fitting an accurate R_2* decay.

In silico methods were used to better understand and account for these fat contributions. We performed Monte Carlo simulations to investigate how the signal time course changes with varying fractions of fat signal. We fit the simulated data using a hybrid Dixon-R_2* signal decay model for simultaneous estimation of R_2* and fat fraction (*ff*). The proposed hybrid fitting technique gives accurate and stable estimates of both *ff* and R_2* across a variety of simulated conditions.

Finally, we translated the hybrid technique to real data using *in vitro* samples of SPIO labelled cells and oil. The data were fit using both the simple mono-exponential decay model and the proposed hybrid technique. The proposed technique gives more stable R_2* estimates for SPIO labelled cells when fat is present at fractions greater than 15%.

This work represents the first instance of simultaneous R_2* and fat estimation using TurboSPI. Improved R_2* estimates will lead to more accurate quantitative cell tracking in future *in vivo* studies.

List of Abbreviations and Symbols Used

Acronyms

APC - antigen presenting cell

bSSFP - balanced steady-state free precession

CHESS - chemical shift selective

CS - compressed sensing

CTL - cytotoxic T lymphocyte

DC - dendritic cell

DPX - DepoVax

EM - electromagnetism

FID - free induction decay

FS - fat saturation

GFP - green fluorescent protein

GS - gold standard

GT - ground truth

GRE - gradient recalled echo

LMD - local magnetic dose

NMR - nuclear magnetic resonance

MRI - magnetic resonance imaging

PD-1 - programmed death-1

RF - radio-frequency

RMSE - root-mean-square error

nRMSE - normalized root-mean-square error

ROI - region of interest

SDM - slow diffusion model

SDR - static dephasing regime

SE - spin echo

SNR - signal to noise ratio

SOP - standard operating procedure

SPI - single point imaging

USPIO - ultra-small superparamagnetic iron oxide

SPIO - superparamagnetic iron oxide

STE - stimulated echo

TE - echo time

TR - relaxation time

tSNR - temporal SNR

TurboSPI - multiple spin-echo single point imaging sequence

Symbols

α - fat frequency offset

B_o - main magnetic field

D - diffusion coefficient

R - cell radius

R_1 - longitudinal relaxation rate

R_2 - transverse relaxation rate

R_2* - effective transverse relaxation rate

T_1 - longitudinal relaxation time

T_2 - transverse relaxation time

T_2* - observed transverse relaxation time

T_{2W}* - observed transverse relaxation time for water species

T_{2F}* - observed transverse relaxation time for fat species

$\Delta\chi$ - change in magnetic susceptibility

ζ - volume fraction

Acknowledgements

If it takes a village to raise a child then it requires a similar amalgamation of people to produce a thesis. I would like to thank those who helped with this one.

First, my co-supervisors, Dr. Kim Brewer and Dr. James Rioux. Kim welcomed me into the Biomedical MRI Research Lab (BMRL) and helped guide this project (through a number of iterations) into its final form. I am very grateful for her expertise in cellular and molecular imaging, without which this project would not have been possible. James joined the supervisory team when I began working with TurboSPI. I benefited greatly from his expertise and tools developed during his PhD work: TurboSPI sequence, *Relax!*, simulation framework, and the extended slow diffusion model. Both Kim and James suffered through many first drafts (of abstracts, posters, presentations, this work) and were patient but instructive in their guidance. As well, they answered many stressed emails during experiments, for which I am equally appreciative and apologetic.

My committee members, Dr. Chris Bowen and Dr. Marianne Stanford, may have quite different specialties, but they similarly offered valuable input, advice, and direction to this interdisciplinary topic.

I would like to thank the BMRL group for their assistance and conversations during the past two years. In particular, Dr. Marie-Laurence Tremblay and Christa Davis, who helped tremendously with the cell work and animal imaging, respectively.

Finally I must acknowledge my family and friends who offered support and encouragement, often from many miles away and my boyfriend, Chris Friesen, who provided a healthy balance of motivation, necessary distraction, and A^+ coffee.

Chapter 1

Introduction

1.1 Cell Tracking

The idea of *cell voyeurism* [1] is central to understanding various biological mechanisms such as migration of therapeutic cellular agents or the immune response. Studying singular cellular processes *in vitro* is an effective first step to understanding the various roles and activities of immune cells. However studying these processes *in vivo* offers a further benefit: context.

A common first step in tackling a scientific problem is to first isolate the system of interest, e.g. the well known "Spherical Cow" in physics (or the single voxel simulations encountered later in this thesis). The basic process must be understood before complicating the problem. The similarity between this concept and that of studying immune migrations *in vitro* is the lack of context. While the basic mechanisms must be first understood in an isolated environment, eventually the context is necessary to understand the full scope of the system. Studying cellular processes *in vivo* offers the ability to study immune cell recruitment and migration patterns in their native environment.

Immune cell migration is an important aspect to launching an immune response [2]. Analyzing the migrations of different subtypes of immune cells in longitudinal studies is helpful in understanding the underlying biological processes of the immune system that occur in response to disease and treatments.

This chapter begins with a motivation for cell tracking, an introduction to labelling cells with contrast agent for MRI, the history, and the associated limitations. The following section will present early work of this project that further illustrates cell tracking challenges. In particular, the two sequences used in this thesis will be introduced: *bSSFP* and the more novel *TurboSPI*. Early analysis of TurboSPI data revealed specificity and accuracy issues in the presence of fat. The bulk of this thesis involves investigating methods to account for fat related signal.

1.2 Cell Tracking Motivation

Tracking immune cells in response to immunotherapy is of particular interest for a number of reasons. While the immune system exists to protect the body from sickness and disease, it has a history of failure as a complete defence against cancer, which can overwhelm the immune system often by masking its tumour antigens. Stimulating the immune system to recognize and eliminate cancer is a method that has been long sought after, though only recently brought to the clinical stage [3].

Immunotherapies are a promising addition to the conventional repertoire of cancer-fighting treatments (chemotherapy, radiotherapy, and surgery). These immunotherapy treatments act indirectly in that they do not target the tumours themselves, but manipulate the immune system such that the natural disease eliminating cells can target the tumours directly [4]. Such treatments can either aid effector cells in recognizing tumour antigens or inhibit suppressive activities of regulatory cells (as described in Section 3.1). In North America alone, over 700 treatments are being developed which fall into the immunotherapy category [3]. However, since immunotherapies that have been tested clinically to date have low response rates [5], there is work to do. Understanding response mechanisms is vital in learning how to boost the immunogenic retaliation against cancer [6].

Determining *which* immune cell population to track primarily depends on the research question, e.g. "are we interested in imaging *killer* immune cells or *suppressor* immune cells?". Secondly, it can depend on whether or not the cells have an interesting interaction with the chosen cancer model and treatments. In this work we study cytotoxic CD8+ cytotoxic T lymphocytes (CTLs) in a C3 cancer model with two immunotherapies: a checkpoint inhibitor and peptide-based vaccine (discussed in Section 3.1). Quantifying the recruitment of antigen-specific CTLs is particularly interesting because they are one of the key cell types involved in the immunogenic response to cancer, specifically with cell death. [7, 8].

1.3 Contrast Agents

The use of contrast agents is a common theme in many forms of imaging. Different agents are used for unique clinical indications to enhance contrast in regions

associated with certain pathologies [9]. In MRI these agents are usually indirect, that is they are not imaged themselves, but create contrast by affecting the relaxation of nearby protons.

Contrast agents used for cellular imaging include paramagnetic agents, compounds that contain fluorine-19 (^{19}F), and superparamagnetic iron oxide (SPIO) [10]. Paramagnetic agents, such as Gd^{3+}, operate as primarily T_1 agents, reducing the T_1 relaxation time and resulting in hyper-intense signal, or *positive contrast* [10]. ^{19}F-MRI cell tracking measures the contrast agent (^{19}F nuclei) directly rather than measuring its effect on surrounding protons using traditional ^{1}H-MRI.

This work focuses on techniques that image cells labelled with SPIO, the most common contrast agent for use in cell tracking in MRI [1].

1.3.1 Superparamagnetic Iron Oxide

The active part of an SPIO nanoparticle is its iron oxide crystal core (magnetite or maghemite). The crystal core is surrounded by a biopolymer coating to prolong their time in the body and obstruct, or slow, opsonization [1].

These contrast agents are typically used for enhanced T_2 and T_2*-weighted imaging. They have large magnetic susceptibilities, χ, a material-specific proportionality constant that describes a materials magnetization in an applied field [11].

$$\vec{M} = \chi \vec{B} \tag{1.1}$$

The SPIOs induce field inhomogeneities [12, 13] that locally alter the main magnetic field and consequently affects the relaxation rate ($R_2^* = 1/ T_2^*$) of protons in their neighbourhood [14, 15]. This rate is described in further detail in Section 2.2. By shortening the T_2* time of nearby protons they provide *negative contrast* (i.e. it is associated with hypo-intense signal) [1].

SPIOs come in a variety of sizes and are loosely categorized according to diameter into micron-sized SPIO ($\approx 1\ \mu$m), SPIO (50-150 nm), and ultrasmall SPIO (<50 nm) [1,16,17]. USPIOs will be used in this project as they are appropriate for the size and nuclear-to-cytoplasmic ratio of T cells (lymphocytes that mature in the thymus). Phagocytic cells are labelled with large diameter SPIO since this ratio is smaller and because they preferentially phagocytose larger particles [18, 19].

As mentioned above, the act of cell-labelling is an interesting application of SPIOs to track the movements of cell populations, thereby gleaning valuable information on cellular recruitment *in vivo* [1]. This is very useful for understanding various biological processes involved in disease and recovery.

In this work, we study SPIO labelled CTLs in a syngeneic, non-orthotopic mouse model of cervical cancer. After labelling with SPIO through *in vitro* incubation [1], the cells are injected into mice and can be detected as regions of hypo-intensity or high R_2* values, depending on the MRI sequence used. Most SPIO cell labelling techniques should not drastically affect the viability [20] or normal activity of the cells [21]. Therefore, the presence of cell related signal (negative contrast on a bSSFP image or high R_2* on a map from TurboSPI) may be interpreted as an accumulation of labelled lymphocytes through regular recruitment in an immune response.

1.3.2 SPIO Cell Tracking History

In its *simplest implementation*, imaging SPIO is not novel itself. Some of the first publications that report using MR to image the effects of SPIO agents date to the 1980's [22–31] and early 1990's [32–38]. The earlier studies characterized the properties of SPIO nanoparticles, their effect on proton relaxivity, and imaging methods. The later studies proposed applications in liver and spleen imaging. Labelling cells with SPIO became a burgeoning field by the late 1990s [39–43] and early 2000s [44–49].

More recent advances in the field of MRI cell tracking are marked by new MR acquisition sequences and analysis techniques. The goal of these techniques is to enable accurate cell quantification and detect SPIO labelled cells with less ambiguity.

1.4 Challenges of Cell Tracking

Cell tracking is not without limitations that must be addressed or, at the very least, acknowledged. Wang et al [50] categorized four major cell tracking challenges, defined in Table 1.1.

Wang suggests that basis of each limitation is *either* physiologic-pathologic or technical (relating to the imaging physics and methods). However, a more thorough interpretation is that the true challenge arises from the combination of physiologic and technical effects.

Table 1.1: Cell Tracking Limitations

Live vs. Dead	Inability to distinguish dead cells from live cells
False Positives	Misinterpretation of MR Signal
Cell Division	Dilution of contrast agent
Quantification	Accurately quantifying cells in an ROI using MR signal

Dying and dead cells can retain SPIO nanoparticles and release them into the vicinity. MR cell tracking cannot distinguish healthy from sick cells. However, if the dead cells release their SPIO, some MR methods, namely R_2* and R_2 mapping, can distinguish this free (extracellular) SPIO from that contained in live cells. This is because the R_2* and R_2 relaxation rates (to be discussed further in Section 2.2) differ for free SPIO versus compartmentalized SPIO (within the cell) [12, 51, 52]. The ratio $\frac{R_{2*}}{R_2}$ is large for compartmentalized SPIO but small for free SPIO, and as such the effect of SPIO bound in cells can be differentiated from loose SPIO [51–53].

Various other *false positives* can arise from a combination of physiology-pathology and technique based effects. For example, phagocytic cells such as monocytes [54], macrophages [55], dendritic cells (DCs) and neutrophils [10] can phagocytose free SPIO that has been discarded by dead cells. In fact, this is the mechanism of action for certain types of cellular MRI [50]. However, this behaviour is not intended when cell labelling occurs *in vitro*. An obvious repercussion of free SPIO phagocytosis is that the detected SPIO labelled cells will be a combination of the cells of interest (those that were originally labelled *in vitro*) and these phagocytic cells.

Cell division can also cause misinterpretation in cellular MRI due to dilution of the SPIO, sometimes occuring asymmetrically [50, 56]. The lower concentration of SPIO carried by daughter cells may be under the threshold of detection [57]. Cell division is particularly detrimental when quantification is attempted via R_2* mapping [58]. Quantification based on R_2 [20] or R_2* [59] mapping uses linear calibration curves to convert R_2* values to cell concentration per voxel. The phantoms used for calibration have varying cell concentrations (number of cells/ml within the tube) but the iron concentration (SPIO per cell) is constant. If the iron concentration changes *in vivo* then the original calibration curve is no longer an accurate representation of the system and can lead to errors converting R_2* to cell number.

This work focuses on tracking immune cells a mere 24 hours after cell injection, allowing enough time for biological uptake but not long enough for the above processes to significantly affect analysis. However, it is important to note that certain physiologic limitations have more serious ramifications for long-term studies in which the subject is scanned multiple days (or longer) after the SPIO cells have been administered [60].

Some false positives are not derived from the original SPIO particles themselves but from endogenous sources of the desired contrast. For example, MR cell tracking methods that detect SPIO labelled cells as signal voids or hypo-intense regions can give erroneous results in the presence of necrotic tissue which can present similarly hypo-intense, as illustrated in Section 1.5.1. Decreased specificity is a drawback of many superparamagnetic or paramagnetic cell tracking methods [61] and accounting for false positives often requires integration with biological techniques for validation. One option to counter these specificity problems is to measure labelled cells directly by using non-proton imaging, most popularly ^{19}F. In this method cells are labelled with ^{19}F compounds and imaged by ^{19}F-MRI [61–63]. ^{19}F offers positive contrast with improved specificity due to the lack of background ^{19}F signal [63, 64]. Unfortunately, the increased specificity of ^{19}F cell tracking is countered by a significant decrease in sensitivity compared to proton-MRI based methods [62]. Some groups suggest tracking hyperpolarized silicon nanoparticles [65, 66] which can address specificity with improved sensitivity (as noted in Section 2.1.3), albeit with unique disadvantages such as the rapid loss of hyperpolarization.

Lastly, quantifying labelled cells *in vivo* is advantageous for cell tracking studies since it offers further power in analyzing biological processes such as cellular recruitment. Rather than merely noting a qualitative change in image contrast that indicates *where cells have gone*, quantitative cell tracking can tell you *how many*. A degree of quantification is necessary when performing any study that requires intra-group and(/or) inter-group comparisons. For example, longitudinal studies tracking different cell-types or responses to different treatment methods.

Frustratingly, quantitative cell tracking is just as challenging as it is desirable [50]. Some issues with quantitation are physiological-pathological, as mentioned above, but quantifying cells *in vivo* is technically challenging as well. Qualitative cell tracking

analysis can become *semi-quantitative* when baseline images are taken prior to introducing the SPIO-labelled cells and signal intensity histograms in the *before* and *after* images are compared [67], as is shown in Section 1.5.1. Other semi-quantitative methods estimate relative iron mass by comparing signal intensity with SPIO to a matched control without SPIO and use an MRI signal decay model [68]. Unfortunately, these semi-quantitative techniques offer only relative SPIO quantification, require baseline scans, and are susceptible to false positives. Quantitative imaging can be performed with ^{19}F, however sensitivity remains an issue for this technique.

Relaxation mapping is popular for quantifying cells labelled with SPIO. Since the relaxation rate, R_2* (discussed in Section 2.2), increases as a function of cell concentration [52, 59], this relationship can be utilized to convert R_2* maps to cell density maps. R_2* mapping generally requires acquiring multiple images at different echo times and fitting the exponential signal decay at each voxel in an image. Since the R_2* maps are used to estimate cell concentration, the fidelity of the mapping technique is key to accurate and successful quantification. This work investigates R_2* mapping by TurboSPI, a technique which is first described in Section 1.5.2.

1.5 Rationale

1.5.1 Previous Work: bSSFP

A number of groups have performed SPIO labelled cell tracking using the balanced steady steady free precession (bSSFP) sequence that is discussed further in Section 2.6.1 [48, 67–73]. bSSFP type sequences are noted for being sensitive to superparamagnetic iron oxide contrast and have also been used to image effects of SPIO [28].

While bSSFP is ideal for its sensitivity to iron loaded cells and high signal-to-noise ratio (SNR), it suffers from some of the limitations discussed in Section 1.4, specifically false positives results and a lack of quantitative capabilities.

False Positives

Studies of immune cell recruitment include monitoring cell migration in response to cancer, in response to therapeutic agents [67, 74, 75], or even as the therapeutic agents themselves [10, 76–78]. In the late stages of growth tumours can have

heterogeneous environments with regions of edema, necrosis, apoptosis, and hemorrhage [71, 79]. As stated in Section 1.4, endogenous sources of contrast can create ambiguities in cell tracking. This uncertainty necessitates additional testing not only to confirm the presence of SPIO loaded cells, but also to rule out other sources.

Specific understanding of the tumour structure in the model of interest is helpful, e.g. solid tumours that exhibit central necrosis (also known as a necrotic core) [80–83]. Background knowledge can provide intuition when analyzing MRIs for labelled cells, but this intuition must be validated with data. One method to corroborate a suspicion of a necrotic core is positron emission tomography (PET).

PET is a form of nuclear medicine that uses a well designed radio-pharmaceutical tracer. A radionuclide is carried through the body via a chemical tracer, thus travelling the normal route of the chosen pharmaceutical [84]. Along this route the radioisotope emits radiation in the form of charged particles which undergo a secondary interaction in the sample, emitting high energy electromagnetic (EM) radiation, that signals where the pharmaceutical has travelled and accumulated [85]. The most commonly used radio-pharmaceutical in oncology is ^{18}F fluorodeoxyglucose (FDG) [84,86]. The tracer to which the ^{18}F radionuclide is attached is a glucose analog and it is not cancer-specific, but rather indicates areas in the body with high rates of metabolic activity. The utility of ^{18}F FDG PET in oncology arises from the high metabolic rate of tumour cells, which require large amounts of fuel (glucose) for fast growth [86].

Previous literature has illustrated central necrosis using PET, noting a central region of low metabolic activity in an otherwise active tumour [87, 88].

Complimentary PET data were obtained in a cell-tracking study (Chapter 3) using an MR-compatible PET insert for simultaneous PET/MRI. Figure 1.1 shows an example data set from this study. In the bSSFP images (subfigures a-c), the negative contrast in the tumour centre is ambiguous: it could suggest SPIO labelled cells or necrotic tissue. We cannot confidently know the source without further information from necropsy or other imaging methods. In this case, low activity in the PET overlay (subfigures d-f) confirms a necrotic core, illustrating a case of false positive detection by bSSFP.

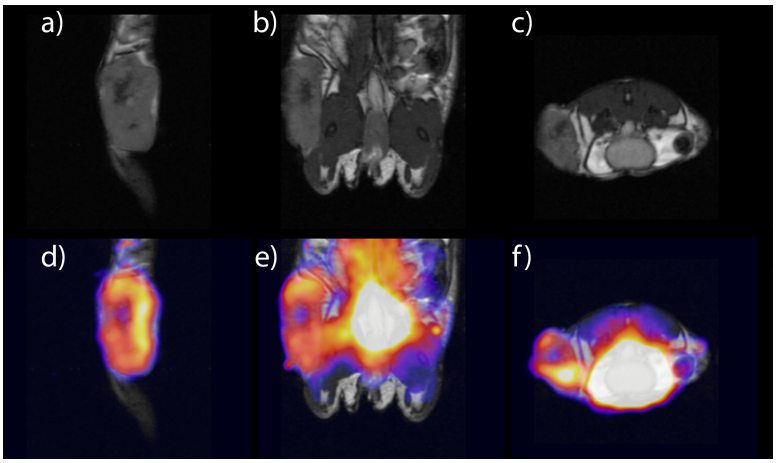

Figure 1.1: Upper row: MRI obtained using bSSFP. Bottom row: 18F-FDG PET/MRI overlay in matched planes using PET data obtained simultaneously.

Previous Analysis Methods

Additionally, the analysis techniques available with a sequence like bSSFP are not quantitative. The most basic analysis of these images is qualitative, simply noting regions of negative contrasts in unexpected (i.e. without SPIO) areas, for example the tumour site or the lymph nodes.

As mentioned in Section 1.4, analysis can become semi-quantitative by using methods of comparison, to a baseline scan (before SPIO) or control region. Figure 1.2 illustrates an example of semi-quantitative analysis of cell recruitment using bSSFP with a baseline scan. The orange (24 hours post cell injection) histogram is skewed and the peak is shifted toward darker contrast values. Unfortunately, these techniques offer only relative, not absolute, quantification and are subject to ambiguities.

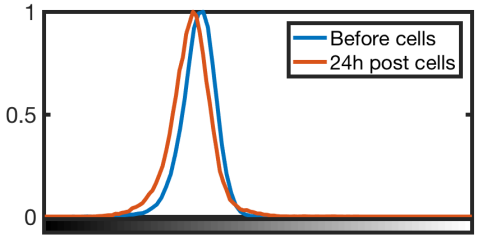

Figure 1.2: Normalized bSSFP signal intensity histograms of the a C3 flank tumour ROI before (blue) and 24 hours after (orange) injection of SPIO labeled cells.

1.5.2 TurboSPI

For the reasons listed above, we took a two-sequence approach to cell-tracking. While bSSFP images are useful for anatomical context and for their qualitative and semi-quantitative approach, a new sequence, TurboSPI, adds further quantitative capability. TurboSPI will be discussed in more detail in Section 2.6.2, but a brief introduction to the benefits and challenges of this sequence will be given here.

TurboSPI is a multi-echo single point imaging (SPI) technique that was first developed for porous media [89] after it was shown that SPI is capable of quantitative relaxation mapping for materials with short T_2* [90]. TurboSPI was then adapted for quantification of SPIO [91] and more recently for *in vivo* cell tracking applications [92]. SPI type sequences are capable of imaging broad line-width samples with less artifact and thus higher quality than traditional techniques [89]. Multi-echo TurboSPI can achieve R_2* mapping with high temporal resolution. These factors make TurboSPI a good candidate for the high fidelity R_2* mapping needed for SPIO labelled cells, as discussed in Section 1.4. While single point imaging is very slow, the acquisition time can be significantly accelerated by employing *compressed sensing* processing techniques [92]. Since compressed sensing involves reconstructing undersampled data we can acquire fewer k-space data points, which makes TurboSPI feasible for *in vivo* imaging.

TurboSPI had been tested *in vivo* before the start of this thesis, but Chapter 3 presents the first example of this sequence being used for a large *in vivo* study. This study uncovered limitations - nay challenges, of TurboSPI, particularly when performing R_2* mapping in the presence of fat. While fat suppression is performed in the TurboSPI sequence, there are limits to its efficacy due to line-broadening in the samples (Section 5.2.1).

Figure 1.3 illustrates that specificity of the R_2* map can deteriorate in the presence of fat. Incorrect fits occurred largely in the fat pads adjacent the tumour and lymph nodes. Interestingly, in this mouse there appears to be greater cell migration to the periphery of the tumour. Therefore, the erroneous voxels are especially problematic since they are near areas of potential cellular detection. Figure 1.3 indicates a voxel with SPIO labelled cells near fat (*region 1*), a signal from pure fat (*region 2*), and another possible combination of SPIO labelled cells and fat (*region 3*).

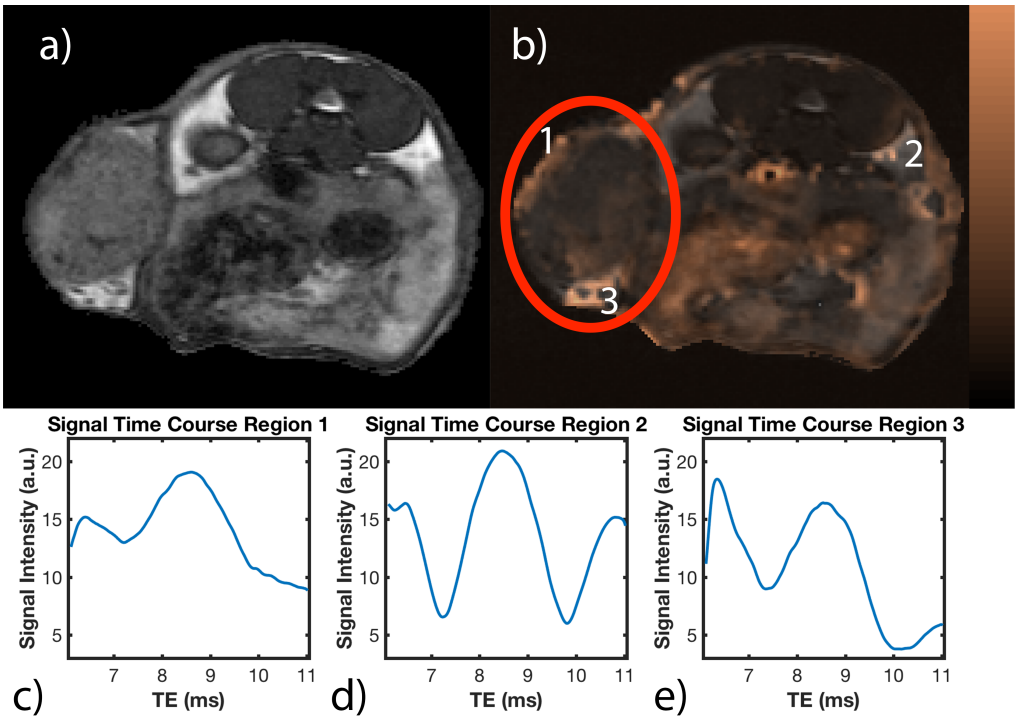

Figure 1.3: Upper row: a) bSSFP MRI b) R2* map (intensity: 0 - 600 s^{-1}) overlaid on the axial bSSFP slice. The tumour is highlighted by the red circle. Bottom row: the MR signal time course for region 1 (c), region 2 (d), and region 3 (e)

Preliminary analysis of these TurboSPI data may therefore drastically inflate cellular recruitment estimates, likely due to the presence of fat. Although TurboSPI can distinguish between necrosis and SPIO labelled cells, the current mapping technique can not reliably separate the fat signal from that of the cells. False positives from fat are easily recognized when visually analyzing individual signal time courses, but automating this analysis and fitting the effect is difficult. Therefore, we must better understand and characterize fat contributions in the TurboSPI signal.

1.6 This Thesis

We use three studies to investigate fat contributions in the TurboSPI signal and develop tools to account for their effect. These studies use *in vivo*, *in silico*, and *in vitro* methods, respectively. First, we illustrate the problem further with the *in vivo* data and show initial attempts at fat correction.

Next, we will study the system using *in silico* methods, mainly Monte Carlo

simulations. These methods allow us to study the signal contributions with a greater degree of control. We can add varying amounts of off-resonance fat signal to simulated data and observe changes in the resulting signal time course. Likewise, we can change the volume fraction of labelled cells to simulate different R_2* decay factors. With these data we can test different strategies for fat correction. By combining Dixon water-fat separation with R_2* decay fitting we hope to develop a novel analysis scheme for more robust R_2* estimates.

Lastly, we will test the methods developed *in silico* on *in vitro* data consisting of gelled solutions with varying amounts of oil, water, and labelled cells. *In vitro* data provide a compromise with respect to data complexity - less control and precision than simulations but more than an animal model. We will fit the data using both the original mono-exponential decay model and the novel technique to compare their performance for different fat fractions. The overall goal is to refine TurboSPI analysis methods so that future cell tracking studies will benefit from improved accuracy in the presence of fat.

Chapter 2

Theory

2.1 NMR

A discussion of magnetic resonance imaging (MRI) is incomplete without first introducing the concept of nuclear magnetic resonance (NMR). NMR describes the behaviour of MR active nuclei in a magnetic field. The I in MRI refers to spatially resolving the NMR signal.

2.1.1 The Quantum Framework

The process exploits the quantum mechanical (QM) manifestation of *spin* (intrinsic angular momentum). Nucleons are spin-$\frac{1}{2}$ particles described by their eigenstate: spin-up $|\frac{1}{2}\rangle$ or spin-down $|-\frac{1}{2}\rangle$. The (MR active) nuclei used in NMR have an odd number of nucleons and in MRI the spin-$\frac{1}{2}$ ^{1}H nucleus is primarily studied. Nuclear spin, $\mathrm{m}_I = \pm\,\frac{1}{2}$, is described as the eigenvalue of the I_z QM operator [93] [94].

$$I_z\,|\psi\rangle = m_I\hbar\,|\psi\rangle \tag{2.1}$$

A semi classical interpretation considers a "spinning" charged particle (proton), whose circulating current creates a small magnetic field, or *magnetic moment*, $\vec{\mu}$. The proton spins are often likened to tiny classical bar magnets. The magnetic moment $\vec{\mu}$ is associated with the spin by the gyromagnetic ratio γ a proportionality constant specific to the nucleus of study. For the nuclei studied in typical (^{1}H) NMR $\frac{\gamma}{2\pi} = 42.58\ \frac{MHz}{T}$ [95].

$$\vec{\mu} = \gamma\vec{I}. \tag{2.2}$$

In the absence of an external magnetic field, $\vec{B}$, the two spin-states are of equal energy and randomly aligned. However, if an external field is imposed, B_o, states align

in parallel (low energy) or *antiparallel* (high energy) with a slight majority aligned in parallel for its lower energy.

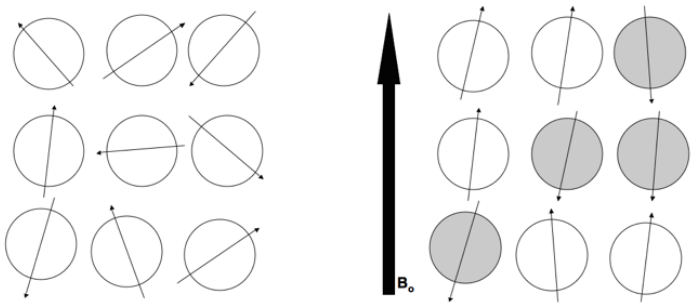

Figure 2.1: A schematic of proton spins randomly aligned in the absence of a magnetic field (left) and their response to an imposed field ($\mathbf{B}_o$) aligning either in parallel or antiparallel to the direction of ($\mathbf{B}_o$) (right).

The energy difference between these two states arises from the splitting of energy levels in a magnetic field, known as the *Zeeman Effect* [94]. The energies ($\mathbf{H}\left|\psi\right\rangle = E\left|\psi\right\rangle$) are calculated using the Hamiltonian responsible for this effect $\mathbf{H}_B$, where $\hbar = \frac{6.626\times10^{-34}}{2\pi}$Js is a form of Planck's constant.

$$\mathbf{H}_B = -\vec{\mu}\cdot\vec{B} \tag{2.3}$$

$$\mathbf{H}_B = -\gamma\mathbf{I}\mathbf{z}B_0 \tag{2.4}$$

$$\mathbf{H}_B\left|\psi\right\rangle = -\gamma\hbar m_I B_0\left|\psi\right\rangle \tag{2.5}$$

$$E = \mp\gamma\hbar\frac{1}{2}B_0 \rightarrow \Delta E = \gamma\hbar B_0 \tag{2.6}$$

A simple calculation equating ΔE to the equation for transition energy uncovers ω_L, which is equal to the Larmor frequency, the characteristic frequency of resonance described in the next section.

$$\Delta E = hf = \hbar\gamma B_o \tag{2.7}$$

$$\therefore f = \frac{\gamma}{2\pi}B_o \tag{2.8}$$

$$\omega_L = \gamma B_o \tag{2.9}$$

The field strength of the pre-clinical MR scanner at the BMRL is B_o=3 T, therefore the ω_L = 127.74 MHz.

2.1.2 The Classical Framework

If the magnetic moment $\vec{\mu}$ is considered classically as a "bar magnet" then the applied magnetic field B_o produces a torque on the moment, which causes $\vec{\mu}$ to precess in alignment with the magnetic field [96, 97]. The alignment is imperfect and there is an angle θ between the vectors as in Figure 2.2.

$$\vec{\tau} = \vec{\mu} \times \vec{B} \tag{2.10}$$

Continuing to think classically and now geometrically, the torque is used to uncover the Larmor frequency. The torque describes how the angular momentum (L for consistency with classical notation) changes with time [98].

$$\vec{\tau} = \frac{d\vec{L}}{dt} = \gamma \vec{L} \times \vec{B} \tag{2.11}$$

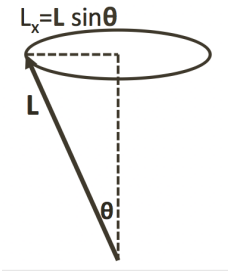

Figure 2.2: A schematic of the precessional motion of the classical angular momentum vector, **L**, and its radius of motion used to calculate the Larmor frequency.

The precessional motion occurs with the frequency of repetition described in Eq. 2.12 by thinking of torque as the speed of the precession (Eq. 2.11) and distance as $2\pi r \rightarrow 2\pi L_x \sin\theta$ [96] [98]:

$$f = \frac{\tau}{2\pi L sin\theta} \tag{2.12}$$

This frequency can be related back to the same Larmor frequency described above using 2.10 (and the cross product rule):

$$f = \frac{\mu B_0 \ \cancel{sin\theta}}{2\pi L \ \cancel{sin\theta}} \tag{2.13}$$

Finally, substitute Equation 2.2 for μ, while using the classical L for classical angular momentum. The resulting angular frequency is the equal to that found above for the transition energy.

$$\omega_L = \gamma B_0 \tag{2.14}$$

2.1.3 Net Magnetization

Of course one is not detecting single protons when performing NMR experiments but rather a group of many protons. The work in this thesis focuses on the macroscopic behaviour of relaxation. Therefore, a more thorough explanation considers an ensemble of protons which can each occupy one of the two (Zeeman) energy levels. The probability of occupation and populations of these spin-states and are determined by Boltzmann thermal equilibrium statistics [95].

$$\frac{N_\downarrow}{N_\uparrow} = e^{-\gamma\hbar B_o/k_B T} = e^{-\Delta E/k_B T} \tag{2.15}$$

Here, k_B and T are the Boltzmann constant ($1.38\times10^{-23}\frac{J}{K}$) and temperature, respectively. For our experimental conditions of T=293 K and B_o = 3T, this ratio of anti-aligned to aligned states is approximately 0.99998. The excess of $N_\uparrow$ states is only slight: e.g. for 1000000 $N_\downarrow$ states, there are approximately 1000020 $N_\uparrow$ states. The population difference can be enhanced through hyperpolarized MRI, which is especially useful to increase sensitivity when imaging nuclei with lower γ and/or abundance.

Since the effective magnetization comes from an excess of aligned spin-states, the net magnetization vector ($\vec{M}$) is aligned "up" with B_o and the magnetization at equilibrium can be derived from Equation 2.15 [95].

$$M_o = \frac{1}{V}\frac{\gamma^2\hbar^2 B_o}{4k_B T}N_{tot} \tag{2.16}$$

Which shows how magnetization magnitude is proportional to the applied B_o field and inversely proportional to temperature.

2.1.4 B_1 Application and Evolution of $\vec{M}$

$\vec{M}$ can be broken into longitudinal and transverse components, labelled $\vec{M}_z$ and $\vec{M}_{xy}$ respectively [98] [99].

$$\vec{M}_z = M_z\vec{z} \textbf{ and } \vec{M}_{xy} = M_x\vec{x} + M_y\vec{y} \tag{2.17}$$

At equilibrium $\vec{M}$ is aligned with $\vec{B}$ and therefore all magnetization is in the longitudinal direction. That is:

$$M_z = M_o \textbf{ and } M_{xy} = 0 \tag{2.18}$$

To measure magnetization $\vec{M}$ the NMR signal is obtained by perturbing the magnetization vector out of B_o alignment using an orthogonal radiofrequency (RF) pulse, as was first introduced by both Bloch [100] and Purcell [101].

Energy shifts between the two spin-states occur by absorption of EM radiation at the given Larmor frequency, ω_L. This input energy is absorbed by the lower energy (aligned) states to move them into the higher energy state. Consequently, the magnetization $\vec{M}$ changes since the relative population of $\uparrow$ and $\downarrow$ states have changed.

When considered in the "rotating frame", i.e. a frame of reference that rotates at ω_L, the effect of the RF pulse (called B_1) is a "tipping" of the vector $\vec{M}$ towards the transverse plane [95] [99]. The degree to which $\vec{M}$ tips into the transverse plane is called the flip (or tip) angle α.

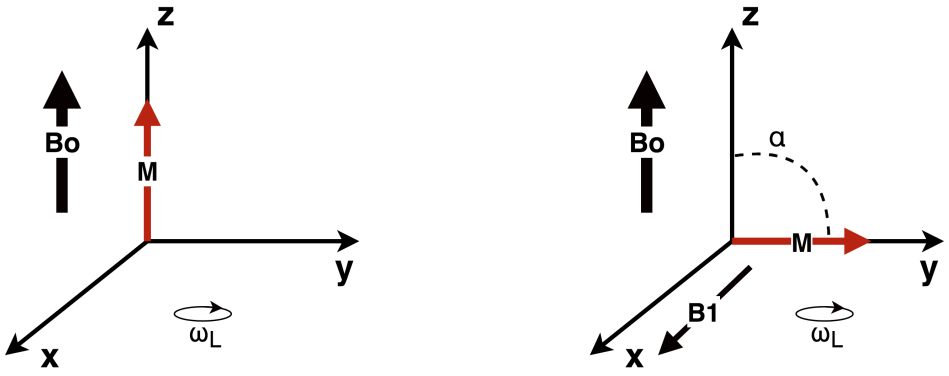

Figure 2.3: Left: a schematic that shows the magnetization vector aligned with B_o before applying B_1. Right: a schematic that shows the tipping of the magnetization vector ($\alpha = 90°$) after applying B_1. Both schematics are shown in the rotating-frame.

After the perturbation by B_1 the magnetization vector $\vec{M}$ precesses back to alignment with the main field in a spiral motion (as viewed in the "lab frame"), regaining longitudinal magnetization and losing transverse magnetization. The time-evolution of $\vec{M}$ is dictated by the famous Bloch equation [100] [102], where T_1 and T_2 are time constants that describe the return (or *relaxation*) to equilibrium.

$$\frac{d\vec{M}}{dt} = \gamma\vec{M} \times \vec{B} - \frac{M_x\hat{x} + M_y\hat{y}}{T_2} - \frac{(M_0 - M_z)\hat{z}}{T_1} \tag{2.19}$$

2.2 Relaxation

As described above, after the B_1 field has been applied the system tends back towards equilibrium such that $M_z = M_o$ and this behaviour is studied using Equation 2.19. These time constants vary for different molecular species and image contrast is created by exploiting this variation. Depending on the formalism these are also discussed in terms of relaxation rate such that:

$$R_1 = \frac{1}{T_1} \textbf{ and } R_2 = \frac{1}{T_2} \tag{2.20}$$

R_1 and R_2 describe regaining longitudinal magnetization and losing transverse magnetization, respectively. These processes are also referred to as spin-lattice relaxation (T_1) and spin-spin relaxation (T_2) and are named for the nuclear interactions that drive them [98].

It is useful to separate Equation 2.19 into its longitudinal and transverse components to study the two relaxation rates individually [100]:

$$\frac{dM_x}{dt} = -\frac{M_x}{T_2} \textbf{ and } \frac{dM_y}{dt} = -\frac{M_y}{T_2} \rightarrow \frac{dM_{xy}}{dt} = -\frac{M_{xy}}{T_2} \tag{2.21}$$

$$\frac{dM_z}{dt} = -\frac{(M_z - M_o)}{T_1} \tag{2.22}$$

The behaviour that governs spin-lattice relaxation is the transfer of energy to the system of surrounding molecules (the lattice) by thermal motion and as such it is also historically referred to as thermal relaxation [100] [103].

$$M_z(t) = M_o(1 - e^{-\frac{t}{T_1}}) \tag{2.23}$$

The behaviour that results in transverse decay of spin-spin relaxation is dephasing of the nuclear spins in the magnetization vector [99] [103]. T_2 relaxation is dominated by inter-nuclear (spin with spin) interactions [100]. Nuclear spins are affected by the minute magnetic fields produced by their neighbours and as such exhibit different ω_L [98] i.e. a line-broadening in the frequency domain. These changes in the precession frequency lead to a loss of coherence and a reduction to the net magnetization vector. Intuitively, R_2 relaxation is always faster than R_1 relaxation, since transverse relaxation is lost to the spin-lattice interactions as well as the spin-spin interactions [98].

$$M_{xy}(t) = M_o e^{-\frac{t}{T_2}} \tag{2.24}$$

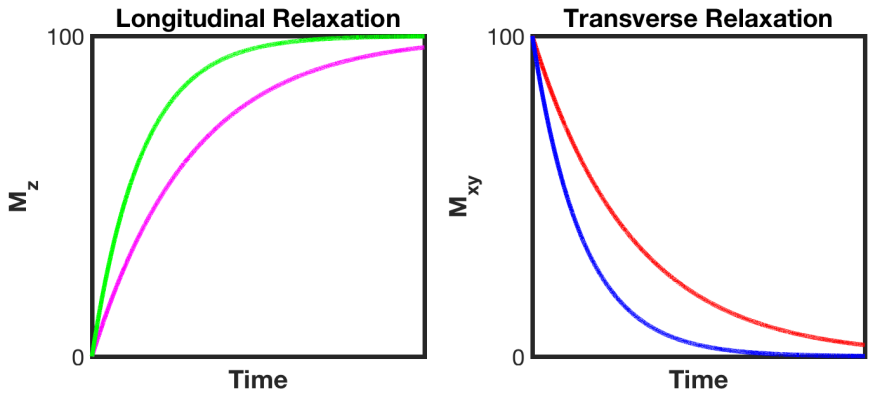

Figure 2.4: Left: Longitudinal relaxation for a species with long T_1 (pink) and short T_1 (green). Right: Transverse relaxation for a species with long T_2 (red) and short T_2 (blue)

Nuclear spin-spin interactions are not the only cause of dephasing; there is another mechanism that is very important to this thesis. Local field inhomogeneities similarly lead to changes in ω_L and consequent phase incoherence [98]. These local field inhomogeneities can be system based imperfections or deliberate manipulations from, for example, injected superparamagnetic iron oxide nanoparticles.

A new relaxation rate, R_2*, is defined to account for the combined effect of spin-spin related dephasing (R_2) and inhomogeneity related dephasing (R_2'). It follows that

T_2* is always less than or equal to T_2. It is equal only in an ideal/perfect magnet and in the absence of tissue induced inhomogeneities.

$$R_{2*} = R_2 + R'_2 \tag{2.25}$$
$$\frac{1}{T_{2*}} = \frac{1}{T_2} + \frac{1}{T'_2}$$

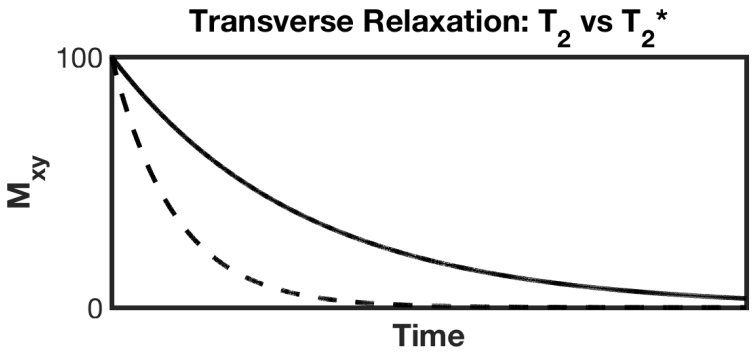

Figure 2.5: T_2 (solid) versus T_2* (dashed) relaxation: local field inhomogeneities increase the transverse relaxation rate

2.2.1 Relaxometry

Most clinical pulse sequences are designed to provide weighted images whose contrast is dominated by a given parameter [104]. This may be sufficient for many clinical indications, but contrast changes can be ambiguous (as discussed in 1.5.1) and, in research especially, it is useful to estimate the parameters directly. Parameter estimation is performed by taking multiple signal measurements while varying an aspect of the pulse sequence. A relevant example is fitting a time constant (T_1, T_2, or T_2*) by taking measurements at multiple time points throughout the decay [98]. The signal (magnetization) decay curve is then fit to these measurements to estimate the parameter of interest.

$$M(t) = M_o e^{-\frac{t}{T_2}} \tag{2.26}$$

Naturally, taking more measurements at various time points secures a more accurate fit. This speaks to a benefit of TurboSPI that was mentioned in Section 1.5.2: high temporal resolution for R_2* mapping.

2.3 NMR Signal

The MR signal is detected from the M_{xy} time-varying magnetic field. The signal equation is commonly written in its simplest form as [105]:

$$S(t) = \int M_{xy}(\mathbf{r}, 0) e^{-i\omega(\mathbf{r})t} d\mathbf{r} \tag{2.27}$$

This is re-written in terms of spin density $\rho(r)$ which is proportional to the initial magnetization, omitting T_2 relaxation at this point.

$$S(t) = \int \rho(\mathbf{r}) e^{-i\omega(\mathbf{r})t} d\mathbf{r} \tag{2.28}$$

2.3.1 Free Induction Decay

The free induction decay (FID) is the simplest form of the MR signal [105]. It is the decay of transverse magnetization after administering and RF pulse [106].

After an RF pulse, the transverse magnetization decays according to Equation 2.24 and the signal evolves as:

$$S(t) = \sin\alpha \int e^{-\frac{t}{T_2(\mathbf{r})}} \rho(\mathbf{r}) e^{-i\omega(\mathbf{r})t} d\mathbf{r} \tag{2.29}$$

Where α is the tip-angle introduced in Section 2.1.4. The magnetization is completely tipped into the transverse plane when $\alpha = 90°$.

$$S(t) = \int e^{-\frac{t}{T_2(\mathbf{r})}} \rho(\mathbf{r}) e^{-i\omega(\mathbf{r})t} d\mathbf{r} \tag{2.30}$$

Therefore if the system is simplified to a single spatial component with $\omega = \omega_L$ [105]:

$$S(t) = M_o e^{-\frac{t}{t_2}} e^{-i\omega_L t} \tag{2.31}$$

2.4 Spatial Information: Magnetic Resonance *Imaging*

MRI uses the above foundation of NMR, but obtains further information by spatially resolving the signal to form an image. Spatial information is obtained using

gradient coils G_{xyz}. The gradients superimpose a linearly varying magnetic field on to the main magnetic field.

$$B(\mathbf{r})' = (B_0 + \mathbf{G} \cdot \mathbf{r}) \tag{2.32}$$

Applying gradient fields changes the magnetic field that a proton experiences due to their position and thus the frequency ω_L changes as a function of position $\omega_L(r)$. This is referred to as *frequency encoding* and this gradient is commonly formalized as being the x-direction [105] [106].

$$S(t) = \int \rho(\mathbf{r}) e^{-i(\omega_{Lo} + \gamma \mathbf{G} \cdot \mathbf{r})t} d\mathbf{r} \tag{2.33}$$

The ω_{Lo} term is not spatially dependent and can be removed from the integral, and this "carrier signal" can be removed from the equation [105].

The equation can be parametrized in terms of spatial frequency, $\vec{k}$ [105]

$$S(\mathbf{k}) = \int \rho(\mathbf{r}) e^{-i2\pi \mathbf{k} \cdot \mathbf{r}} d\mathbf{r} \tag{2.34}$$

Where $\vec{k}$ is connected to t by the frequency encoding gradient:

$$\mathbf{k} = \frac{\gamma}{2\pi} \mathbf{G} t \tag{2.35}$$

This way, the spin density $\rho(r)$ is found by inverse Fourier transform of Equation 2.34:

$$FT^{-1}(S(\mathbf{k})) = \rho(\mathbf{r}) = \int S(\mathbf{k}) e^{i2\pi \mathbf{k} \cdot \mathbf{r}} d\mathbf{k} \tag{2.36}$$

Frequency encoding resolves one direction of a two-dimensional slice of k-space, but the other (typically formalized as the y-direction) is described by phase encoding. The phase encoded signal is also described in k-space by Equation 2.34, however in this case the gradient has a defined brief temporal duration (Δt =T_{pe}) and k is a fixed value that defines the starting point in k-space [105].

$$\mathbf{k} = \frac{\gamma}{2\pi} \mathbf{G} T_{pe} \tag{2.37}$$

Its application for T_{pe} also causes a change in ω_L as a function of position, but once the gradient is turned off the frequencies will return to normal. However, the

phase difference that was caused by differing ω_L will remain and thus k-space has a position dependent phase $\phi(r)$ before frequency encoding is performed [106].

An image is obtained by traversing k-space in specific trajectories that are defined by controlled sequences of RF and gradient pulses at different strengths for different lengths of time. Data are acquired in k-space and inverse Fourier transformed to the more visually intuitive image space that shows ρ(r).

2.5 Sequences

2.5.1 Spin Echo vs Gradient Echo vs Stimulated Echo

An *echo* is another type of NMR signal that is used more often than measuring the FID itself. The two most common forms, *spin-echo* (SE) and *gradient-(recalled)-echo* (GRE), with different mechanisms of production [105]. A third form, the *stimulated-echo* (STE), will also be discussed briefly, as STEs are seen in both the bSSFP and TurboSPI sequences. The SE arises from an additional (second) RF pulse while the STE is caused by three (or more) RF pulses in succession and the GRE arises from a gradient reversal. In this work, TurboSPI depends on mainly on SEs and bSSFP depends on GREs (as demonstrated by their sequence diagrams in Figures 2.8 and) however STEs appear in both sequences as well.

Spin Echo

The SE technique was first introduced by Hahn [107] [108] and adapted by Carr and Purcell [109]. Their procedure uses the original 90° RF pulse with an additional 180° refocusing pulse. The utility of the SE is to create a measurement that is more reflective of T_2 than T_2* and this is done by reversing the effect of inhomogeneity related dephasing (T_2'). The 180° pulse is called a *refocusing* pulse since it is designed to refocus the magnetization vector by regaining the phase coherence that was lost due to inhomogeneity [106].

As mentioned earlier, T_2' dephasing arises from changes in ω_L caused by inhomogeneities in B_o: some spins precess slower or faster than ω_{Lo}. When the refocusing pulse is applied, the magnetization is flipped to the other side of the transverse plane and the faster spins will begin to *catch up* with the slower spins, thereby regaining

coherence [105]. If the echo is to be formed at an *echo time* TE then the 180° pulse should be set at $\frac{TE}{2}$. Additionally, the inhomogeneities should not change with time. The amplitude of the echo is still damped according to T_2, since this effect cannot be recovered.

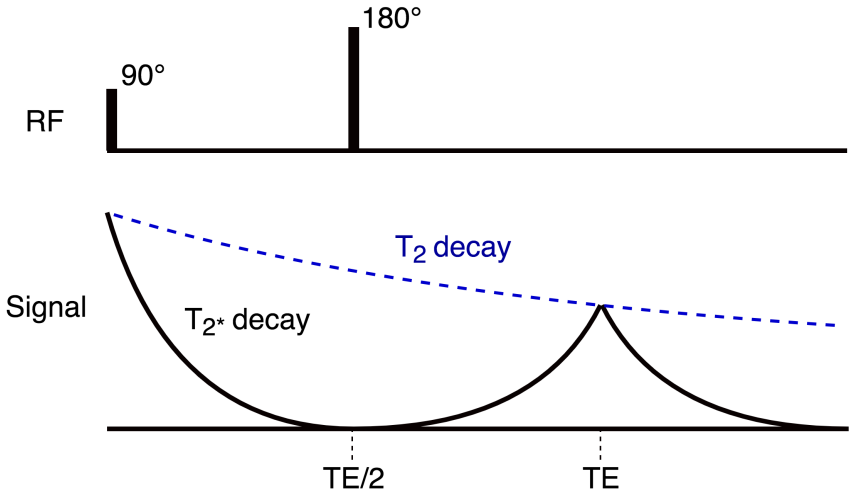

Figure 2.6: The spin echo sequence with paired 90° and 180° RF pulses. The echo is weighted by T_2 since the T_2* effect is refocused at TE. Inspired by [105]

Gradient Echo

The GRE sequence obtains an refocused echo by using so-called *dephasing* and *rephasing* gradients instead of a second RF pulse [110]. While the GRE was first discovered and formalised not long (<10y) after the SE, GRE sequences were not popular in clinical practice until the 1980s-1990s [111]. While SEs and GREs have unique strengths that benefit various research problems (as is seen in this thesis), a particular advantage of the GRE-type sequence is speed. This is because the TE can be controlled by gradient pulse design in addition to the smaller flip angles that are typically used (rather than $\alpha = 90°$) which allow shorter relaxation times (TRs) [105] [112].

In figure 2.7 the first negative gradient causes deliberate accelerated dephasing after the RF pulse. The spins are refocused to coherence by applying subsequent positive gradient that is at least equal in strength and thus, an echo is formed. In this framework, the only phase effect that is counteracted is the deliberate incoherence caused by the dephasing gradient. Since the natural T_2' effects are not refocused, the

amplitude of the echo will be weighted by T_2* rather than T_2 [105]. The enhanced T_2* sensitivity is advantageous when detecting iron labelled cells.

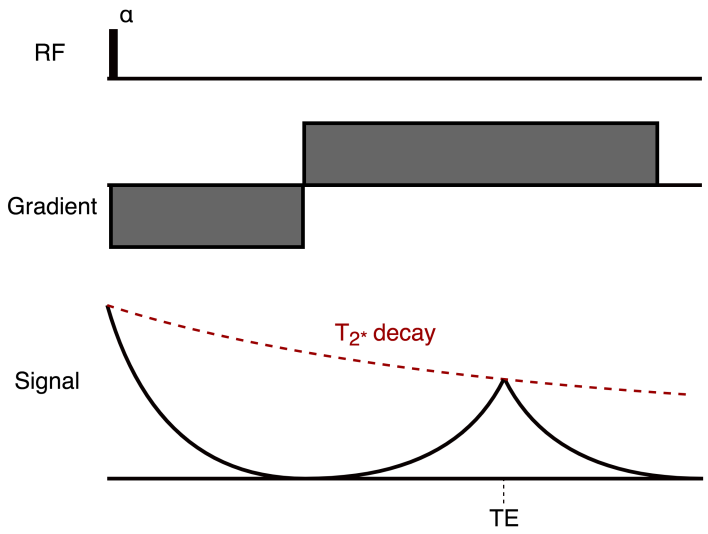

Figure 2.7: The gradient recalled echo sequence with an α RF pulse and paired *dephasing-rephasing* gradients. The echo is weighted by T_2* since only the deliberate dephasing is refocused at TE. Inspired by [105]

Stimulated Echo

STEs result from application of multiple (three, or more) RF pulses and (like other echoes) their contribution to the signal largely depends on pulse sequence parameters, such as RF and acquisition timing [113]. For example, in the simplest case of three 90° RF pulses applied x-direction [113]: 1. the first pulse (with which we are familiar from above) tips magnetization (in *z-direction* to start) toward the *y-direction* and the magnetization vector begins to lose coherence in the transverse plane; 2. the next pulse tips magnetization in the *y-direction* towards the ± *z-direction*; 3. the last (in this simplified example) pulse tips magnetization in the ±*z-direction* to ± *y-direction* and the magnetization rephases to form an STE in the -*y-direction*.

These echoes can be the dedicated echo (as in the stimulated echo acquisition mode (STEAM) sequence [114]), an intended source of signal contribution, as in the bSSFP sequence, or an unwanted side effect that must be addressed. STEs can be addressed by either removing the STE or optimizing it through alignment with SE, as in the TurboSPI sequence.

2.6 Sequences of Interest: bSSFP and TurboSPI

2.6.1 bSSFP

The first sequence used in this work is in the *fast GRE* family: balanced steady-state free precession, also often referred to as TrueFISP, FIESTA, or balanced-FFE. As mentioned above, GRE-type sequences typically benefit from the speed availed by short TR, TE, and low α [115], however the overall acquisition time is increased for bSSFP by the multiple acquisitions needed to counter the banding artifact characteristic to bSSFP. This sequence is ideal for imaging SPIOs [28] [1] since GRE-type sequences are sensitive to susceptibility effects [116]. As discussed in Section 1.5.1, this sequence has been shown to be successful in imaging contrast enhanced cells.

Figure 2.8 shows an example of a 2D slice-selective bSSFP pulse sequence diagram. The *balance* is intuitive when looking at the lobes of the gradients in the pulse sequence: the net gradient area over a full TR is equal to zero.

$$\int_0^{TR} G_i dt = 0 \tag{2.38}$$

All gradients are *rewound* between RF pulses [116], and the *rewinding* gradients are equal and opposite to those applied at the beginning of the sequence.

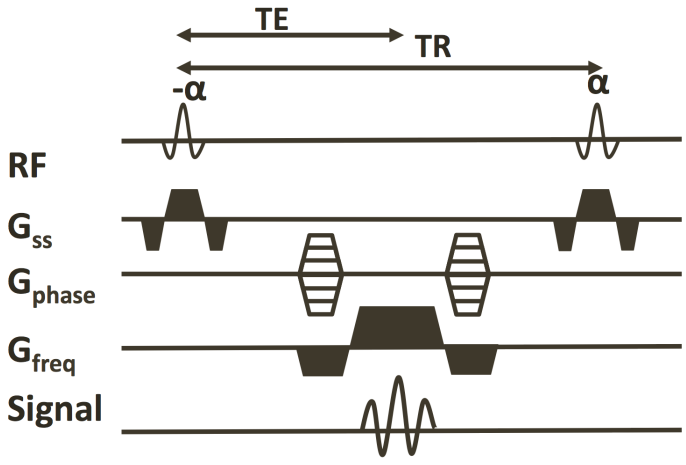

Figure 2.8: An example pulse sequence diagram for a 2D bSSFP sequence showing the balanced gradient lobes in all three directions (G_x, G_y, G_z). The balance is given by the net gradient area = 0 for each of the three gradients over the TR

bSSFP is a steady state form of a gradient echo sequence. In a completely steady-state sequence, the spins in the sample are not given enough time to relax fully to $M_z = M_o$ equilibrium. If the TR is sufficiently short compared to the T_1 and T_2 time constants, the next RF and gradient pulses will arrive before the spins have recovered from the last pulse (the magnetization will not have fully recovered to the longitudinal axis or decayed from the transverse plane) [117]. Therefore, at the next RF pulse some transverse magnetization (M_{xy}) will be pushed longitudinally, while the longitudinal magnetization (M_z) that did recover will be tipped toward the transverse plane as usual. If this process is repeated a number of times then the magnitudes of M_z and M_{xy} become constant from one TR to the next and the system is said to have reached a steady state [117]. The number of RF pulses to obtain steady state magnetization depends on the time constants of the tissues, the flip angle, and the relaxation time [115].

bSSFP has inherently mixed contrast weighting and in standard execution of the sequence, SPIO provides effective negative contrast through locally enhanced T_2 weighting. A simplified version of the steady-state magnetization (M_{SS}) equation for the bSSFP sequence is given below in Equation 2.39 [118]. The simplification occurs because $TR << T_{1,2}$ [118] which is a highly biologically relevant assumption for T_1 (TR = 8ms in this thesis) and is valid to a lesser degree for T_2. This equation shows that the sequence has both T_1 and T_2 dependance, resulting in unique mixed T_2/T_1 contrast weighting [119].

$$M_{SS} = M_o \frac{\sin\alpha}{1 + \cos\alpha + (1 - \cos\alpha)(\frac{T_1}{T_2})} \tag{2.39}$$

While bSSFP belongs to the family of GRE sequences, it is unique in how it approaches residual M_{xy} that remains when using short TR [117]. Other fast GRE sequences (like spoiled GRE (SPGR)) refocus M_z but spoil M_{xy}, resulting in a signal that is primarily T_1 weighted [117, 120]. As discussed above, bSSFP refocuses both magnetization components such that the final signal itself is a mix of overlapping STEs and SEs [117] (even though bSSFP is in the GRE class [120]). By obtaining steady-state in both M_z and M_{xy}, bSSFP is not only a truer steady-state sequence, but also utilizes more of the initial magnetization to earn greater SNR (compared to SPGR which "wastes" some of the initial magnetization).

2.6.2 TurboSPI

As was first introduced in Section 1.5.2, TurboSPI performs multi-echo R_2* mapping with high temporal resolution. R_2* mapping can provide quantitative estimates of cellular recruitment since R_2* increases linearly with SPIO concentration and therefore with increased cell density in a voxel.

Single Point Imaging

TurboSPI uses single point imaging (SPI) for data acquisition: a single k-space data point is collected per RF excitation. Spatial encoding for SPI is performed using only phase encoding gradients, rather than the combination of phase encoding and frequency encoding [121]. SPI techniques are able to overcome B_o inhomogeneity and susceptibility artifacts by virtue of their data encoding scheme [92]. Since susceptibility artifacts are expected when imaging SPIO, this is a significant feature of the sequence.

Recall from equations 2.35 and 2.37 that $\vec{k}$ depends on t for the case of frequency encoding and a constant T_{pe} for the case of phase encoding. Phase encoding is not performed dynamically as a function of t, but rather performs a shift to a new location for each excitation. For this reason, SPI is also called *constant time imaging* (CTI) [121]. Purely phase encoded sequences are therefore immune to artifacts associated with frequency encoding such as *line-broadening* from T_2* effects (among others) [89] [121]. Line-broadening from T_2* results from changes in ω_L and therefore widening of the frequency spectra [105].

Note that Equation 2.29 describes how signals decay with T_2 or T_2* by multiplication with the transverse exponential. Section 2.4 showed the Fourier relationship between k-space and image space with Equations 2.34 and 2.36. A property of the Fourier transform is that multiplication in one domain becomes a convolution in the other [122] [123]. Convolutions cause blurring, or a loss in spatial resolution [123] so it follows that strong T_2* effect can degrade resolution.

Functions that modulate the k-space signal are referred to as *modulation transfer functions* (MTF) and the Fourier pair is the *point spread function* (PSF). The shape of the PSF, particularly its full width at half maximum (FWHM), is often used to

describe image resolution [121] [122]. Therefore, it follows that an idealized "perfect" PSF would have an infinitesimal width, as in the Dirac delta distribution. The corresponding Fourier pair (i.e. the idealized MTF) is constant unity for all spatial frequencies [124]. Gravina described the total PSF as multiple convolutions from different imaging deteriorating effects [121]:

$$PSF_{total} = PSF_{\Delta k} * PSF_t * PSF_D \tag{2.40}$$

Where the $\mathrm{PSF}_{\Delta k}$ term describes k-space sampling, the PSF_D term describes diffusion, and PSF_t describes the effects that cause magnetization to vary with time during readout. Idealized *total* PSF and *total* MTF are impossible in the practical case of real measurements. However, since $\vec{k}$ is not time-dependent during a solely phase encoded acquisition, PSF_t becomes a delta function. Therefore, even though a "perfect" *total* PSF is impossible, the final image is unaffected by artifacts like susceptibility [121].

TurboSPI for R_2* Mapping

Immunity from frequency encoding artifacts is not the only benefit of TurboSPI with respect to quantifying SPIO. As a (multi) spin echo sequence, TurboSPI would traditionally create an R_2 weighted image collected at the center of the echo [89, 91]. However, in more recent implementations [91, 92] multiple data points are collected for each voxel during the *rephasing-dephasing* of the echo such that the SE itself can be resolved in a signal time course. This is available because the acquisition is not performed during frequency encoding. Data are acquired with a sampling frequency of 100 kHz resulting in very fine temporal resolution.

When used for cell quantification TurboSPI data analysis involves fitting the spin-echo decay (Figure 2.9) for each voxel in an image to obtain a map of R_2* values. The map is then converted to cell/voxel estimates using a calibration from a set of phantoms with known cell concentrations. Owing to its "artifact immunity", TurboSPI has a large dynamic range meaning that it can detect and quantify labelled cells in low and high concentrations. This is in contrast to other R_2* mapping techniques that are unable to map voxels with high concentrations of SPIO due to substantial signal loss [91].

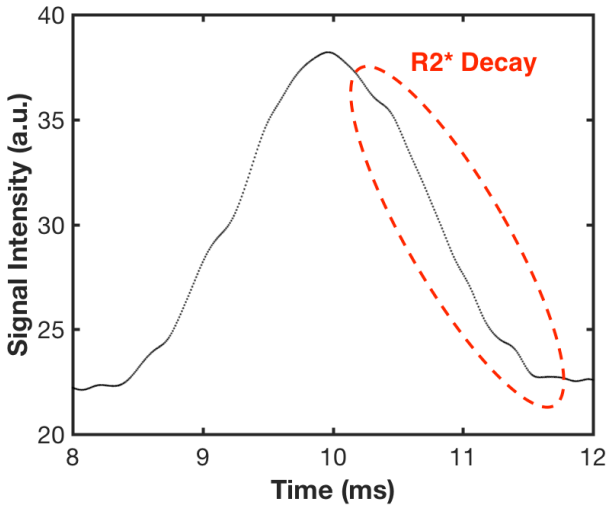

Figure 2.9: An example of TurboSPI data in a signal time course plot for an *in vitro* voxel with SPIO labelled cells with the R_2* decay highlighted. The effective TE is 10ms. While the data are plotted as discrete points, they appear as a line due to the fine temporal resolution. Time course data are fitted for each voxel in an image to obtain an R_2* map.

Accelerated Acquisition

The clear drawback of any SPI technique is time: collecting an image one point at a time is *slow*. Even a 2D N×N image requires N^2 spin echoes from (traditionally) N^2 excitations [89]. The two time-saving mechanisms that combine to make SPI feasible *in vivo* are *a) using a multi-echo sequence* [89] and *b) compressed sensing (CS) acquisition* [92]. The combined effect allows one to *a) collect more points per RF pulse* and *b) require fewer points overall.*

The multi-echo sequence uses an echo train to acquire multiple k-space points per excitation. The data acquisition scheme is ordered such that the echo train steps through k-space in a radial line such that the first echo is acquired near the center and the last echo in the train (which is more attenuated by T_2) is acquired near the edge [92]. This is ideal since the center of k-space describes contrast in the image. Even with this scheme, multi-echo TurboSPI is best when the T_2 is much larger than T_2*. Conveniently, this is the case with SPIO loaded cells (for which R_2* >> R_2) but not for free SPIO particles, as noted in Section 1.4. This divergence is due to the relative scale of the SPIO induced field inhomogeneity versus the distance of water

diffusion. When SPIO nanoparticles are compartmentalized in cells, their magnetic field inhomogeneities will be sufficiently large such that the water cannot diffuse out of the inhomogeneous region during a typical acquisition time scale [12] and thus R_2' behaviour dominates, causing high R_2* but low R_2.

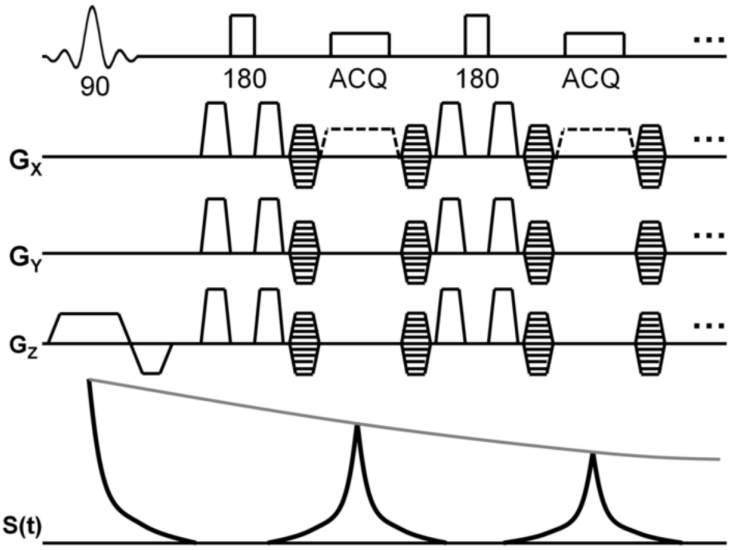

Figure 2.10: TurboSPI sequence with 3D phase encoding gradients. Both T_2 (grey) and T_2* (black) decays and two of the eight spin echoes are shown. The dashed line is an optional readout gradient to obtain a template FSE image at t = $TE_{effective}$. From [92]

Advances in CS image processing enable the undersampling of k-space without significant detriment to image quality. Lustig describes the CS method as requiring *a) image data sparsity*, *b) incoherent artifacts*, and *c) a nonlinear optimization reconstruction such that image sparsity and consistency with acquired data are maintained* [125]. Rioux proved that TurboSPI can conform to these requirements and described how the sequence is particularly amenable to sampling for incoherent artifacts since it can randomly undersample across three dimensions [92]. This is because it doesn't use frequency encoding, of which random undersampling is difficult. CS TurboSPI also uses prior information in the form of a fast spin echo (FSE) pre-scan with matched parameters at a single time point (TE) [92]. Prior information from a guide has utility in prescribing a sampling pattern such that sampling density is

increased in image regions with higher signal. The prior information is also used as an initial condition and constraint in the optimization reconstruction.

2.7 Chemical Shift

Section 1.5.2 introduced a challenge of TurboSPI for *in vivo* applications: the presence of fat. While protons from water molecules account for the majority of the ^{1}H MR signal in an *in vivo* sample, a small portion comes from protons in fat molecules [126]. The current automatic R_2* calculation erroneously fits the signal from fat which confounds the quantification results.

The term *chemical shift* refers to a relative shift, or peak separation, in the frequency spectrum caused by the different magnetic environment that protons experience depending on their chemical structure (shown in Figure 2.11). In fact, the goal of NMR spectroscopy is to classify chemical species using these spectra. However, the effect can have frustrating consequences in imaging. Chemical shift phenomenon arises from the electron cloud that a surrounds a nucleus - electrons from the nucleus itself and its neighbours [127]. The electron cloud produces small magnetic fields that oppose $\vec{B}$ which in turn shield the nucleus [128]. Of course, this changes the effective $\vec{B}$ felt by the proton and the Larmor frequency from Equation 2.9 can be re-written.

$$\omega_{eff} = \gamma B_{eff} \tag{2.41}$$

The chemical shift (δ) is commonly referred to in parts per million (ppm) so that the value can be applied to any field strength.

$$\delta = \frac{\omega - \omega_o}{\omega_o} \tag{2.42}$$

The strongly electronegative oxygen in water compared to the long hydrocarbon chain in fats give rise to very different shielding environments for water protons versus fat protons [126]. The chemical shift for the main peak of the fat spectra is 3.5 ppm (with respect to water) [127] [126] so the frequency difference is approximately 447 Hz at 3T. This means that the signal from fat protons cycles in phase to out of phase with the signal from water protons approximately every 1.1 ms (the half of 447^{-1} s).

$$\Delta f_{WF} = (3.5 \times 10^{-6}) \cdot (42.58 \times 10^{6} \frac{Hz}{T}) \cdot 3T = 447Hz \tag{2.43}$$

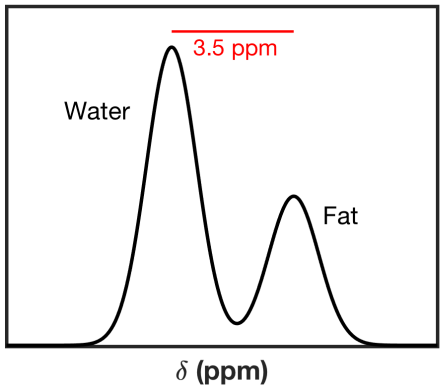

Figure 2.11: A diagram showing water and fat peaks for a simulated *in vivo* sample. The peaks are separated by 3.5 ppm in the δ scale, or 447 Hz at 3T.

The traditional chemical shift artifact (also known as *chemical shift of the first kind*) is voxel displacement in the reconstructed image [129] [130]. This occurs because spatial encoding is performed by creating intentional frequency shifts as a function of position using the gradient field. Since the fat protons resonate at an inherently lower frequency, their spatial position will be mis-mapped. It follows that the displacements occur in the frequency encoding direction, but not the phase encoding direction.

TurboSPI is a purely phase encoded sequence and is thus unaffected by the traditional chemical shift artifact. The fat δ effect on TurboSPI data is one of time dependent contrast, rather than spatial displacement, and it is observed in the signal time course. The fat protons precess in and out of phase with a period of 2.2 ms (Equation 2.43). Signal intensity modulation is seen in time courses as demonstrated by Rioux [91] and also shown in Figure 1.3 d. This is a similar manifestation of the same phase cycling effect that causes *chemical shift of the second kind* or *india ink* artifact at tissue boundaries in GRE sequences for certain TEs [97]. For cell quantification purposes the effective artifact is observed in the R_2* maps when automatic fitting misinterprets the signal modulation from TE $\rightarrow$ (TE + 1.1 ms) as a decay. This is especially problematic if a voxel contains both fat and labelled cells, as suggested in Section 1.5.2.

Employing *fat saturation (fat sat)* is one way to address these off-resonance effects [131]. TurboSPI uses chemical shift selective (CHESS) pulses. This technique involves using an RF pulse that is specifically tuned to the shifted frequency of fat protons (the righthand peak in Figure 2.11). First, the fat saturation RF pulse tips the fat spins into the transverse plane while sparing the water. Next, a *spoiler gradient* spoils the transverse magnetization from fat (M_{xy-fat}), after which the main imaging sequence is performed on the unsaturated water protons. Understandably, this technique is quite sensitive to field homogeneity [131] and susceptibility effects. A CHESS pulse is performed in TurboSPI, but its efficacy is limited by line-broadening in the sample.

2.8 Fat-Water Separation

Fat-water separation is another fat suppression technique that exploits the chemical shift effect [132]. Rather than utilizing the peak separation in the frequency spectrum as is done in fat saturation, this method is based on the oscillating relative phase separation of the two species (described above). The goal is to use multiple measurements (two or more) with known water-fat phase differences to generate separate water and fat images. Clinically, this method has value in creating fat-suppressed images that are often more effective than fat saturation resulting in enhanced lesion detection [132] [133].

When using this type of technique it is important to have an appropriate signal model, such as that described in a comprehensive review by Ma [133]:

$$S(x,y) = [W(x,y) + F(x,y)e^{i\alpha}]e^{i\phi(x,y)}e^{i\phi_0(x,y)} \tag{2.44}$$

Where S is the complex signal, W and F represent relative signal magnitudes from water and fat, α is the phase angle between them, ϕ is a time dependent phase error related to main field inhomogeneities ΔB_0. ϕ_0 is a time independent, but spatially varying, phase error from system imperfections, such as phase shifts between components (e.g. the transmit and receive coils) or RF penetration differences [134] [133].

$$\alpha = \Delta\omega_{WF}\Delta t \tag{2.45}$$

$$\phi = \gamma\Delta B_0\Delta t \tag{2.46}$$

α is known since it depends on the established fat-water frequency difference (Equation 2.43) and Δt. The other parameters in Equation 2.44 (W, F, ϕ, ϕ_0) are spatially dependent unknowns.

In reality, the signal magnitudes, W and F, depend on relaxation times, but this effect is neglected in many forms of the model since Δt is short [133]. Even though this model ignores the T_2* effect, which is relevant to this work and will be discussed further below, it is a clean description of the fat-water signal.

2.8.1 Dixon Formalism

Water and fat separation by chemical shift was first suggested by Dixon in his seminal 1984 paper [135].

In SE sequences this method starts with first obtaining a typical SE image. The typical SE image gives an *in phase* image since both the water and fat spins have been rephased. This is why *chemical shift of the second kind* artifact is not seen in SE sequences. Next, another image is obtained by adjusting the timing of the refocusing pulse with respect to the readout gradient [133] [135]. This shifted acquisition generates an image in which the fat and water spins are *out of phase*. The degree to which they are out of phase depends on the timing delay used. In the original *two-point* Dixon imaging, they are 180° out of phase. These in and out of phase time points are used to calculate the relative signal contribution from water and fat.

The two-point Dixon uses two known α values: 0 and π. These convenient angles allow Equation 2.44 to by simplified greatly using Euler's formula.

$$\begin{aligned} e^{i0} &= \cos(0) + i\sin(0) = 1 \\ e^{i\pi} &= \cos(\pi) + i\sin(\pi) = -1 \end{aligned} \tag{2.47}$$

Such that the signal at 0 and π can be calculated by [133]:

$$S_0 = (W + F)e^{i\phi_0} \tag{2.48}$$
$$S_\pi = (W - F)e^{i\phi_0}$$

The two-point implementation neglects the time dependent ϕ term described above [133] [136]. Dixon showed how water and fat images could be created using simple arithmetic [135]. The ϕ_0 term is excluded by taking the magnitude of S_0 and S_π or W and F.

$$W = \frac{S_0 + S_\pi}{2} \tag{2.49}$$
$$F = \frac{S_0 - S_\pi}{2}$$

It is unreasonable to neglect the ϕ term, that is to assume perfect B_0 homogeneity. That is why the *three-point* Dixon technique was developed [136]. By adding another measurement, this implementation can tackle the ΔB_0 as well. The original three-point formulation (Equations 2.50) collected the 0 and π images with an additional -π image as well [136], but some early methods use a 2π angle [133] [137], and others use asymmetric non-integer values [138]. TurboSPI gives many options for Δt (π, 2π, -π, and more).

$$S_0 = (W + F)e^{i\phi_0} \tag{2.50}$$
$$S_\pi = (W - F)e^{i\phi}e^{i\phi_0}$$
$$S_{-\pi} = (W - F)e^{-i\phi}e^{i\phi_0}$$

Three measurements for the three unknowns (since ϕ_0 is dealt with by taking the magnitude at the end). Here, the additional measurement is used to calculate the ϕ term by $\phi = \frac{arg(S_\pi S^*_{-\pi})}{2}$ so that the W and F images can be calculated as before [133].

Obtaining more time points and performing a fit to the signal model can offer a more accurate estimation of the parameters. However, this is difficult in practice since it requires taking measurements at multiple echoes and can thus be quite slow. Therefore, TurboSPI is particularly amenable to the fitting technique by virtue of the

large number of temporal images that it acquires.

Obtaining more time points also enables the estimation of further parameters. The above formulae neglect T_2* decay. Ignoring decay during the short Δt between time points is acceptable for many tissues, but is the assumption breaks down in regions of high R_2*. For this reason, extended Dixon techniques [134] [139] were developed in which the signal magnitude terms (W and F) are multiplied by the exponential decay factor. Since this work involves imaging high R_2* species, it is important to consider the extended model. Equation 2.44 becomes:

$$S(x,y) = [W(x,y)e^{\frac{-\Delta t}{T^*_{2W}}} + F(x,y)e^{\frac{-\Delta t}{T^*_{2F}}}e^{i\alpha}]e^{i\phi(x,y)}e^{i\phi_0(x,y)} \tag{2.51}$$

Glover argues that the T_2* time should be taken as an average for the water-fat mixture of water, so other Dixon-T_2* studies use a single common exponential term $e^{\frac{-\Delta t}{T^*_2}}$ [134, 139]. However, this thesis allows the water and fat components to have separate decay factors, as shown in Chapters 4 and 5. We will focus on fitting the unique relaxation time for the water species T^*_{2W} which, contrary to an average T_2*, should not change for different fat fractions.

Chapter 3

Pilot Work: *Cytotoxic CD8+ T Cell Tracking*

A pilot study with four treatment groups was performed using both bSSFP and TurboSPI sequences. The goal of the study was two-fold:

1. Investigate the immune response of CTLs in a mouse model

Quantify CTL recruitment in a C3 cancer model for multiple mouse groups receiving different immunotherapy treatments.

2. Pilot TurboSPI in its first large *in vivo* study

Aim 2 is most relevant to the bulk of this thesis. We include TurboSPI in the imaging protocol and note the advantages and challenges of using this sequence. Data from the pilot study largely informed the focus of the fat correction project.

3.1 Background: Cancer Model, Cells, and Treatments

3.1.1 C3 Cancer Model

All mice are implanted with cells from the murine C3 cell line [140, 141]. The C3 cells have been designed to express HPV type 16 (HPV16) [140–143] making it a syngeneic flank model for cervical cancer [144, 145] and thus, well matched to the treatments described below.

Using a flank tumour situated low on the body is ideal for avoiding the lungs, which are difficult to shim and have a large degree of motion even when a mouse is sedated. The flank tumour also creates an unambiguous area of interest which is helpful in a pilot study.

3.1.2 Cytotoxic T Lymphocytes

As mentioned in Section 1.2, we choose the tracking cell population to study specific functions of the immune response. CTLs are interesting because they are directly involved with destroying target cells that carry particular antigens (e.g. C3 cancer cells with R9F). First they must be activated by interacting with antigen presenting cells (APCs) so that they are primed to recognize the antigen.

3.1.3 Immunotherapy Treatments

It is interesting to see how CTL recruitment changes in response to immunotherapies that are designed to enhance cytotoxicity or diminish suppressive activity. Two immunotherapies are studied both as unique treatments and in combination: anti-programmed death-1 (anti-PD-1) checkpoint inhibitor and a DepoVax^{TM} peptide-based vaccine [146]. Previously, CTL recruitment has been studied in a C3 model using MRI with bSSFP (in response to the vaccine) [147] and using biological methods (in response to combination therapies) [143]. Therefore, tracking CTLs in a C3 model with anti-PD-1 and DepoVax is a logical pilot test for TurboSPI quantification.

anti-PD-1

One of the first clinically approved immunotherapy treatments was a checkpoint inhibitor (CPI), or checkpoint blocking antibody [148]. Checkpoint molecules serve a regulatory purpose to control the immune response [149]. Their influence is key to modulating the initiation and duration of an immune response and preventing an over-activation which could result in tissue damage [149] or autoimmunity [150]. Unfortunately, cancer cells can take advantage of these checkpoints by expressing a ligand which can bind to the receptor molecule on an immune cell, initiating inhibition of anti-tumour activity [151]. The CPI studied in this work blocks a popular checkpoint interaction between the *programmed death 1 receptor* (PD-1) expressed on CTLs and the corresponding ligand PD-L1 expressed on C3 cells [148, 152]. As well, anti-PD-1 is particularly interesting with the CTLs since studies have shown that inhibiting PD-L1 expression of dendritic cells (DCs) enhances CTL cytotoxicity [153]. Therefore, anti-PD-1 treatment may enable a stronger response against cancer.

DepoVax^{TM}

DepoVax is not a vaccine itself, but a vaccine delivery system [68, 73, 142, 143, 146, 154]. The unique vaccine platform combines peptide-antigens (to prime T cells) with a proprietary adjuvant (to enhance immune response to the antigen [155]) in a lipid-based (water free) depot [146]. This lipid-based depot allows for slow antigen release [68] to sustain CTL activation and stimulate an enhanced immune response. In this study (and previous work [68, 73, 142, 143, 147]) the vaccine contains R9F, an HPV16 antigen. It is thus well-matched to stimulate an immunogenic response to C3 tumour cells (which express HPV16) by activating antigen-specific CTLs [143].

3.2 Methods

Animal Groups

The animals were housed at the IWK *In Vivo* Facility and practices adhered to approved ethics protocols for animal care. Four groups of mice were imaged: three treatment groups and one group of untreated controls.

- **Untreated** *n=5*
- **Treatment 1**: Anti-PD-1 Checkpoint inhibitor *n=5*
- **Treatment 2**: DPX-R9F Vaccine *n=5*
- **Treatment 3**: Anti-PD-1 + DPX-R9F *n=5*

Each imaging group (C57BL/6 mice, *I Group*) had disease and treatment matched transgenic green fluorescent protein (GFP) donors (C57BL/6 UbC-GFP mice) that were used for harvesting CTLs (*C Group*) and APCs (*A Group*). All mice received a subcutaneous injection of 5×10^5 C3 cells in 100μL in the left flank.

Treatment Group 1 received an intraperitoneal injection of 200 μg of anti-PD-1 in sterile PBS on days 7, 9, 11, 21, 25 post C3 implantation. Treatment Group 2 received a subcutaneous injection of 50 μL of vaccine to the right flank on day 15. Treatment Group 3 received both the anti-PD-1 and DPX-R9F treatments. C3 cell implants and treatments for donor mice were staggered one week early for continuity.

General Protocol

Figure 3.1 shows the high-level timeline for the protocol and Figure A.1 in the Appendix shows a more detailed schedule. Mice were imaged twice: at days 21 and 28 post implant. Therefore two cell isolation procedures were performed per imaging group and mice received two injections.

Cell isolation was performed according to an internal standard operating procedure (SOP) (Appendix A.2) nine days before labelled cell injection. CTLs were harvested from the inguinal, mesenteric, brachial, axillary, and submandibular lymph nodes of the GFP donor mice. The CTLs were cultured *in vitro* for six days for proliferation. APCs were isolated from the spleens of GFP donor mice on the fourth day post CTL isolation and cultured *in vitro* for 48 hours. On the sixth day post isolation CTLs were primed with APCs (1:10 APC:CTL) and R9F antigen for 48 hours. On the eighth day post isolation the primed CTLs were loaded with commercially available 30 nm SPIO nanoparticles (Molday ION Rhodamine B, Biopal) via passive *in vitro* incubation for 24 hours. Approximately $8{\times}10^6$ SPIO labelled CTLs were injected into imaging mice via tail vein injection. Mice were imaged 24 hours after injection to allow for biological uptake.

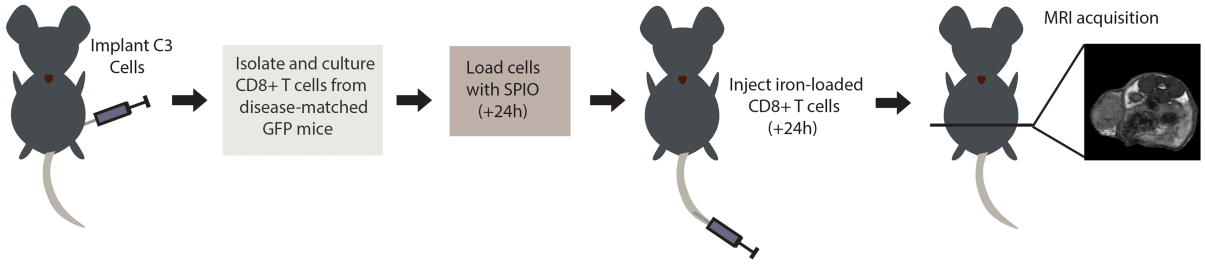

Figure 3.1: A simple schematic of the general method showing the steps from tumour implantation to imaging

3.2.1 Imaging

All MR data were acquired on the 3T pre-clinical Agilent MR scanner at the BMRL. PET data were acquired for select mice (Figure 1.1) using the MR compatible Cubresa NuPET for simultaneous PET/MR imaging. Mice were sedated with an

MR compatible isofluorane anesthetic hookup and physiologic monitoring was performed using small animal monitoring equipment (SA Instruments Inc).

Each *I group* was imaged at day 21 and day 28 post C3 implant. The mice also receive a baseline scan just before injection of SPIO labelled cells and approximately 24 hours before the "main" scans (for cell detection). The baseline is most important for bSSFP data since analysis is based on the relative increase of negative contrast associated with CTL recruitment. However, the baseline scan is also helpful in determining an average R_2* value in C3 flank tumours without SPIO.

Sequences

The proposed two-sequence approach for cell-tracking includes bSSFP (performed first) and TurboSPI (performed second). The relevant imaging parameters for the bSSFP and accelerated TurboSPI sequences are given in Tables 3.1 and 3.2. Additionally, the TurboSPI protocol includes a 3D FSE pre-scan with matched parameters (at one time point) and an unaccelerated 2D TurboSPI (at all time points).

Table 3.1: bSSFP Pulse Sequence Parameters

TR (ms)	TE (ms)	α	N	Matrix	FOV (mm^3)	Time (min)
8	4	30°	4	256×170×170	38.4×25.5×25.5	64

Table 3.2: TurboSPI Pulse Sequence Paramters

TR (ms)	TE (ms)	ETL	ESP	Matrix	FOV (mm^3)	Accel	Time (min)	FSat
250	10	8	10	96×96×48	30×30×30	8	28:54 3DTSPI 4:53 2DTSPI 2:29 FSE	90° sinc low power

3.2.2 Analysis

bSSFP analysis would typically involve signal histogram analysis for the ROI in addition to volumetric analysis of tumour growth. However, since the focus of this

thesis is cell tracking by TurboSPI, the semiquantitative bSSFP contrast analysis will not be presented. For this project bSSFP data were mainly used for anatomic localization, though qualitative observations about contrast in the tumour were noted.

Figure 3.2 describes the major steps in TurboSPI data analysis. The process begins with the CS reconstruction described by Rioux et al [92] in which the FSE scan is used as a guide. It is then useful to observe signal time courses for voxels of interest within the tumour, particularly those with corresponding negative contrast on the bSSFP scan. A voxel with suspected SPIO content is found and appropriate boundaries are chosen to fit the decay. R_2* mapping is performed at each voxel by fitting the linear exponential decay between the set boundaries (after the echo). These first two steps (CS Reconstruction and R_2* mapping) are performed in *Relax!*, which is a Matlab graphical user interface (GUI) originally developed by Dr. James Rioux.

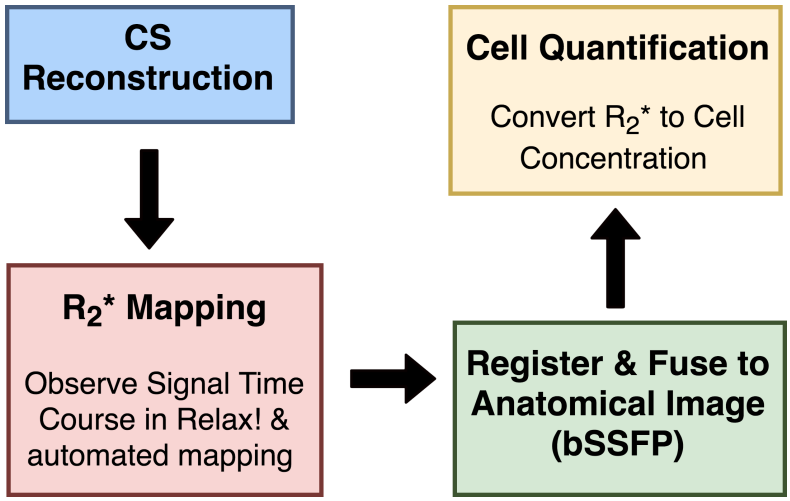

Figure 3.2: A flow chart stating the four major steps to analyzing CS-TurboSPI data: CS Reconstruction, R_2* Mapping, Registration and Fusion, and Cell Quantification

Next, the bSSFP and TurboSPI data are registered and fused in VivoQuant (Invicro). This step reveals an ancillary utility of the FSE scan: it serves as an intermediary for registering the TurboSPI image to the bSSFP image. The data are then fused to exploit the complementary strengths of each technique.

Cell quantification requires a conversion from R_2* to cell concentration (SPIO labelled cell per voxel). This conversion is based on a R_2* calibration with known cell concentrations. Figure 3.3 gives the calibration curve for CTLs: R_2* values for 10

unique concentrations of labelled CTLs in NMR tubes. The R_2* values were obtained individually for each tube by taking the NMR linewidth, or full width half maximum, of the main peak in the frequency spectrum.

$$R_2* = LW\pi \tag{3.1}$$

The R_2* map can be converted to a map of cells/voxel using the linear calibration and the appropriate voxel size (312.5 μm$\times$312.5μm$\times$625μm for this experiment). R_2* is not a specific SPIO metric, but one that correlates linearly with SPIO. The tumour itself has "background" R_2* that must be considered before the final conversion. In this study, we subtracted an average baseline tumour R_2* that was obtained by scanning mice before injection of labelled cells.

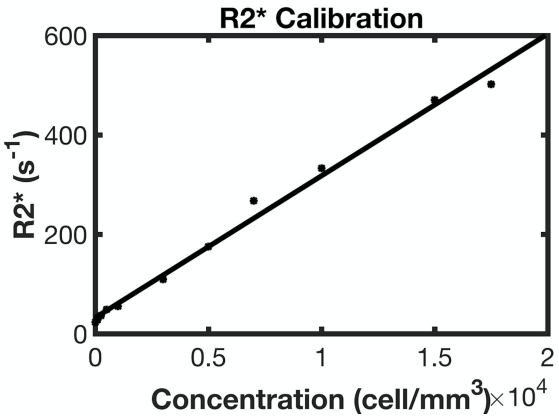

Figure 3.3: A simple plot showing the R_2* calibration for 10 phantoms with different concentrations of SPIO labelled CTLs. $R^2 = 0.994$

It is important that a unique calibration be performed for each cell tracking experiment. This is because the R_2* will vary for different cell types. The effects of SPIO on surrounding protons (and thus the R_2* value) varies with cell loading, as will be demonstrated in Chapter 4. As well, the amount of SPIO a cell contains is a function of cell size, cytoplasmic to nuclear ratio, phagocytic properties, and loading conditions. For example, CTLs contain approximately 5 pg/cell after they are incubated at 4×10^6 cells/mL with 0.075 mg/mL SPIO-Rhodamine B. Since the R_2* effect depends on the mass of iron per cell, it follows that the calibration curve is only valid when the experimental conditions are replicated for each cell injection.

3.3 Results and Discussion

TurboSPI data were not susceptible to the same specificity issues seen in bSSFP data with respect to necrosis. However, initial estimates of cellular recruitment were drastically inflated: some tumours appeared to contain nearly all of the injected cells, which is not realistic. Fortunately, a benefit of TurboSPI is the additional information availed by the fourth (temporal) dimension which allowed us to determine the cause. This is unlike bSSFP data which require auxiliary methods to describe any irregularities confidently.

After scrutinizing the signal time course data, we determined that the overestimates were due to erroneous fits in fat voxels. We found voxels that could contain both SPIO labelled cells and fat particularly concerning. In some mice the bSSFP and TurboSPI data showed increased cellular recruitment to the tumour periphery, indicating suboptimal infiltration. Unfortunately, in the flank tumour there is high fat content at the tumour periphery since the tumour cells are implanted near the fat pad. As well, the inguinal lymph nodes are surrounded by a fat pad which is equally concerning since they are interesting sites with respect to the immune response because they can become enlarged with T cells. In fact, previous studies using pre-clinical MRI found swelling of the vaccine draining inguinal lymph node in response to DPX, which may indicate a more active immunogenic response [68, 73].

The data *were* acquired with a fat saturation pulse, but given that large fat modulations remain in the time course, its efficacy is clearly limited. An initial post hoc fat suppression was attempted: *fat elimination*. This method was implemented before R_2* mapping. Complex temporal data at each voxel were analyzed for the characteristic fat modulation with a period of approximately 2.2 ms. Any voxels that were flagged by this test were exempt from fitting. Figure 3.4 shows R_2* overlays with and without the elimination. While this method was successful at removing fat voxels, it had the unwanted effect of removing voxels with potential mixed content (of cells and fat) which can occur with large voxels. As well, in some cases the strict elimination removed voxels containing no perceptible fat and thus mapping with elimination introduced suspected underestimates in cell numbers.

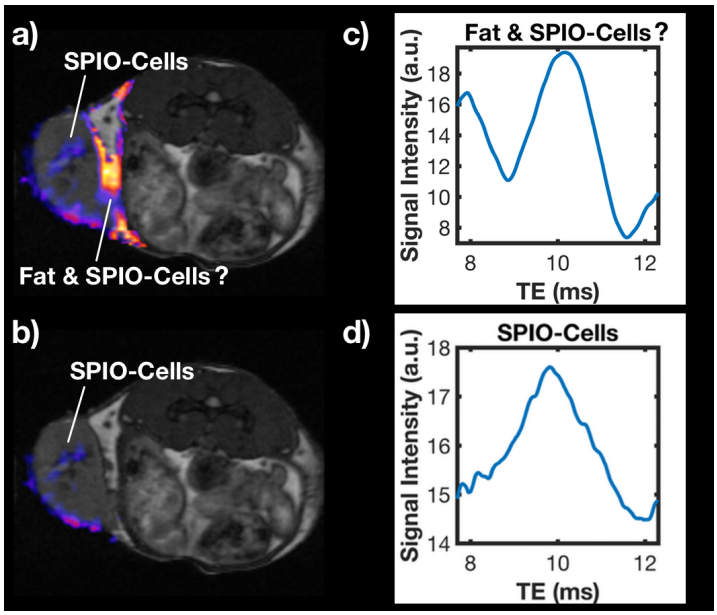

Figure 3.4: Left- bSSFP MRI with R_2* map of the ROI (tumour and surrounding tissue) overlaid with a) no fat corrections and b) simple "fat elimination". Right: Signal time course from voxels at c) inner tumour periphery and d) tumour center. Both techniques recognize d) as labeled cells while c) may suggest a combination of cells and fat or a poor fidelity fat voxel. The fat elimination (b) simply ignores voxels like those in c), however the uncorrected technique (a) fits this as *only cells*. Additionally, strict *elimination* removes many non-fat voxels in the tumour center.

Figure 3.5 shows CTL migration from day 21 to 28. First we note that data were least variable with the combination treatment (Treatment Group 3) and most variable with the Untreated Group. This indicates differences in consistency of response between mice groups. Ideally, all mice (or eventually, all patients) will respond predictably to a given treatment with little variability. Currently, many individual immunotherapy treatments suffer from high individual variability. While slight individual differences are inevitable, the aim is relatively uniform response across a treatment group, rather than individual subject success or failure. In this work, combination treatment exhibited the most uniform response with respect to CTL recruitment, indicating a more preferential response.

While there are no significant differences in mean recruitment between groups, we note that CTL migration appears to increase with the combination treatment while the others decrease. This could suggest that the DPX-R9F + anti-PD-1 combination encourages a more sustained response. However, the finding is purely speculative

as the trend is not supported by a statistically significant difference and further data would be required to corroborate the observation. Weir et al published similar findings using biological methods to evaluate CTL recruitment in response to combination therapies [143]. They found a statistically significant increase in CTL recruitment with the combination treatment for *R9F-specific CD8+ cells*, but not for CD8+ cells that were not specific to the antigen. While our CTLs *should* be primed to be antigen specific, further biological validation will be important in the future to ensure that cells remain primed in the suppressive tumour microenvironment. As well we must note that, in Weir's study, the combination treatment included metronomic cyclophosphamide (mCPA) in addition to anti-PD-1 and DPX-R9F. Including mCPA has been shown to limit immune suppression induced by tumours without reducing R9F-specific CTLs induced by the DPX-R9F vaccine [142]. Therefore, it may be interesting to include mCPA in the treatment plan for future studies.

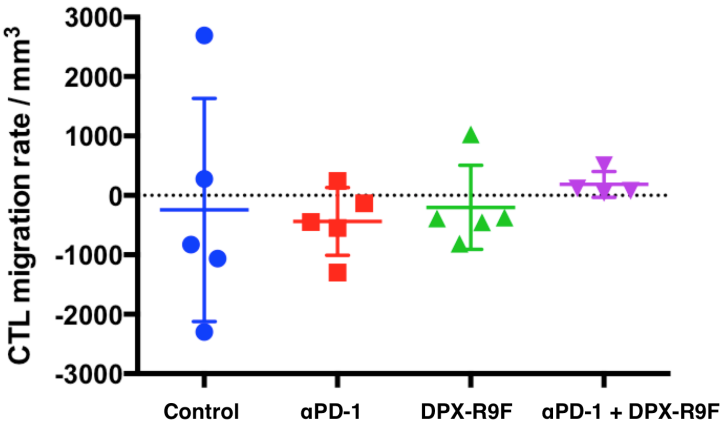

Figure 3.5: CTL migration from day 21 to day 28 post-implant for Untreated, anti-PD-1, DPX-R9F, and anti-PD-1+DPX-R9F. ROI Analysis and Plot by M-L Tremblay.

3.4 *In Vivo* Summary and Conclusions

Aim 1: Investigate the immune response of CTLs in a mouse model

We used TurboSPI to quantify CTL recruitment in four treatment groups: untreated, anti-PD-1, DPX-R9F, and combination anti-PD-1–DPX-R9F. The combination treatment exhibited the smallest intra-group variability, however no significant

differences in recruitment rate were found between groups. Comparison with a previous study that used biological methods [143] suggests this finding may indicate that our CTLs may not be completely antigen-specific. However, fat was detrimental to fitting accurate R_2* and thus to obtaining accurate *in vivo* cell numbers.

Aim 2: Pilot TurboSPI in its first large *in vivo* study

Despite the associated challenges, using TurboSPI clearly offers far more information than bSSFP alone. TurboSPI has greater specificity for SPIO labelled cells versus necrosis, but the R_2* mapping has poorer specificity with respect to fat. Specificity for labelled cells versus fat increased when implementing a simple fat elimination technique, but sensitivity for the labelled cells decreased. Off resonance fat signal adversely impacts R_2* mapping and this effect needs to be addressed to improve quantification accuracy. The first steps will be isolating the system *in silico* to investigate how varying amounts fat affect our signal time courses and then developing techniques for fat correction.

Chapter 4

In Silico Study

The challenges described in Chapter 3 illustrate the need for better fat correction methods in TurboSPI analysis. The fat saturation pulse is not fully effective and post hoc fat elimination was not robust. The remainder of this thesis will focus on improvements to Step 2 in the TurboSPI analysis flow chart (Figure 3.2): R_2* mapping. Specifically, we aim to to improve fit performance in the presence of fat. This is done through *in silico* methods before moving on to *in vitro* data.

4.1 General Methods

The first aim is to determine the fat contribution to the signal, particularly in the time course that is used for fitting R_2*. The second aim is to account for the fat contribution, which involves an estimate of relative fat signal through Dixon type fat-water decomposition.

It is instructive to address these issues *in silico* due to the experimental flexibility availed by simply changing parameters such as cell-size, susceptibility, and concentration. It would be extremely time consuming to run comparable physical experiments and impossible to do so with the same degree of accuracy and precision afforded by *in silico* methods. As alluded to in Section 1.1, it is helpful to begin by simplifying the problem: start with the *ideal experiment* in the absence of noise or B_o inhomogeneity. These methods can then be translated to higher levels of complexity. All calculations for this study were performed in Matlab.

4.1.1 Specific Acknowledgements

The simulation framework was originally developed for blood vessels (with application to fMRI) by Patterson [156] and adapted for spherical perturbers by Rioux [157] [158]. The analytic model was developed by Rioux [157] [158] and was an

extension earlier work by Kiselev [159]. These were invaluable tools with which to study relaxation near SPIO labelled cells.

4.1.2 Simulation

These calculations use Monte Carlo methods, in that they simulate stochastic processes using random sampling [160]. The results are therefore associated with statistical uncertainty that decreases with the number of samples [161]. The stochastic processes at play in this study include both the *random walks* [161] diffusion of water (and thus the signal generating protons) and the geometry of the field of *perturbers* (in this case SPIO-loaded cells) [158]. A $\delta = 3.5$ ppm fat signal will be added to an existing simulation framework and analytic model.

Main Simulation Parameters:

- **Perturber Size ($\boldsymbol{R}$)**: The perturber is that which alters the magnetic field. In the simulation framework, this could be a spherical SPIO nanoparticle, a spherical SPIO-loaded cell, or in previous implementations, a cylindrical blood vessel. For this study, the effective perturber size is the cell radius since the SPIO is compartmentalized within the cell.

- **Volume Fraction (ζ)** This is the fractional volume of the "voxel" that is occupied by perturbers. This directly correlates to the parameter of interest for *in vitro* and *in vivo* experiments: the number of SPIO labelled cells per voxel.

- **Susceptibility ($\Delta\chi$)** Susceptibility difference between the perturber and the inert medium. $\Delta\chi$ offers an *in silico* analog to represent iron loading. It can be likened to mass of SPIO/cell using *in vitro* susceptometry data: 1. Obtain a total $\Delta\chi_T$ for a phantom. 2. Obtain the cell volume fraction $\zeta = \mathrm{V}_{cell} N_{cell}/V_{tot}$. 3. Divide $\Delta\chi_T/\zeta$ to find $\Delta\chi$ for a single cell. 4. Note mass SPIO/cell for given $\Delta\chi$. For example, $\Delta\chi \approx 0.004$ for 3-5 pg/cell.

In our simulations, $\Delta\chi$ is used to calculate the field offset [162] [163].

$$B(\vec{r}, R, \theta) = \frac{4\pi}{3}\Delta\chi B_0(\frac{R}{r})^3(3\cos^2\theta - 1) \tag{4.1}$$

$\vec{r}$ is the distance between the perturber and point at which the field is calculated, R is the perturber size defined above, and θ is the angle between $\vec{B}$ and $\vec{r}$. Since $\Delta\chi$ affects $\vec{B}$, it is the *active* parameter that causes the enhanced R_2' relaxation [12] [163].

$$R_2^{'} = \gamma\frac{2\pi}{9\sqrt{3}} \cdot LMD \tag{4.2}$$

Where *local magnetic dose* (LMD) of the contrast agent describes magnetization from the SPIO [12] [163].

$$LMD = \zeta\Delta M \tag{4.3}$$

- **Timing parameters (*TE* and δt)** The simulation computes signal time course (magnetization as a function of time) and thus the TE of the sequence is relevant. δt is akin to a sampling interval: a time-step between magnetization measurements along the protons random walk.

- **Diffusion Coefficient (*D*)** This is the diffusion coefficient of the sample. It is used to generate the random walks path taken by the proton through the grid of perturbers. The expected distance travelled through diffusion during each time step is by:

$$\textbf{step} = \sqrt{6D\delta t} \tag{4.4}$$

- **Number of Protons (*N*)** The number of protons used in a simulation; i.e. the number of repeated samples/ simulation iterations.

- ***Fat Fraction (ff)*** This is a new addition. The frequency shifted complex signal from fat (S_f) is added to the complex water signal from the simulation (S_w). The *ff* represents the fraction of signal that arises from fat such that the total signal is given by Equation 4.5, where S_f is also scaled by N.

$$S = (1 - ff) \cdot S_w + ff \cdot S_f \tag{4.5}$$

The simulation does not explicitly consider T_1 relaxation and while it does include T_2 relaxation in the framework, the value is set quite large such that the effect is effectively neglected. Since $T_2 >> T_2^*$ for SPIO compartmentalized in cells, this is a reasonable simplification.

Simulation Process

The simulation is based on a framework developed by Boxerman [164] for cylindrical perturbers (blood vessels) which in turn was based on previous work by Weisskoff [162] for spherical perturbers. Weisskoff acknowledges that similar Monte Carlo simulations were performed by others [165] [166] [167]. While the original implementation of the simulation tool used in this work was for cylindrical perturbers [156], it was adapted back to the spherical geometry for cellular imaging [157].

The process involves first generating a randomly distributed grid of spherical perturbers (cells) of size R with a defined volume fraction ζ. They exist in a cube (simulated "voxel") where length of the cube edge is scaled by perturber size and the expected distance of proton diffusion during the time course. This distance is calculated using Equation 4.4 while substituting TR for δt.

Once the grid of perturbers is created, the simulation generates a random diffusion path for the proton to step around the spheres without ever stepping *into* a sphere.

Next, the magnetic field is calculated at each Δt step (and thus each new position) of the proton's journey using Equation 4.1 considering $\Delta\chi$, R, and sphere - proton distance $\vec{r}$. This B calculation is done for each sphere and summed to give the total magnetic field experienced by the proton. That is, Equation 4.1 becomes:

$$B_{NS} = \sum_{n}^{NS} \frac{4\pi}{3} \Delta\chi B_0 (\frac{R}{r_n})^3 (3\cos^2\theta_n - 1) \tag{4.6}$$

Where NS is the number of spherical perturbers based on ζ, R, and voxel size. The calculation is done for each Δt such that there is a vector $B_{NS}(t)$.

Finally, $B_{NS}(t)$ is used to calculate the dephasing in the magnetization during the FID ($t_0 \rightarrow t = TE/2$) and rephasing-dephasing in the SE ($t = TE/2 \rightarrow 3TE/2$) of the TurboSPI sequence using the accumulated phase change throughout the sequence.

$$\phi(t) = 2\pi\gamma B^{'}(t) \tag{4.7}$$

Where

$$B^{'}(t) = \sum_{k=1}^{t} B_{NS}(k)\delta t \tag{4.8}$$

T_2 decay is added to the output, but the T_2 value is kept large such that the decay is slow, as discussed above.

The deliverable is a complex magnetization time course for the single voxel computed from the initial 90° RF pulse to t = 3TE/2. The whole process is repeated N times and the N complex magnetization time courses are summed together to give the final result for all protons. An example of the output for N = 3×10^4 is given in Figure 4.1.

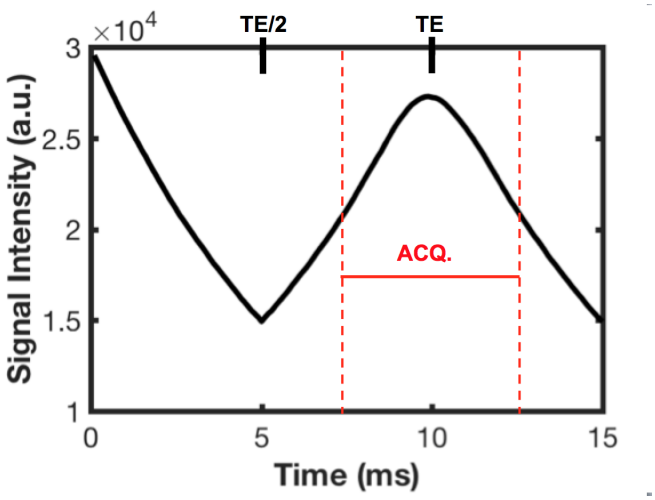

Figure 4.1: An example of the simulation output showing the FID and SE for t = 0 → 3TE/2. Input parameters: R = 4 μm, $\Delta\chi = 30\times10^{-3}$, $\zeta = 1.5\times10^{-5}$. Red dashed lines highlight the typical acquisition window for real (*in vitro*/*in vivo*) data

4.1.3 Model

The aim of an analytic model is to describe the above signal behaviour in a deterministic fashion without need for experimentation through physical means or time consuming Monte Carlo simulations.

The model used in this thesis is based on the slow diffusion model (SDM) developed by Kiselev [159] which describes relaxation from susceptibility related dephasing

by a microvascular framework. This framework is similar to the blood vessel network described above with application to fMRI. Rioux extended the SDM to describe spherical perturbers for application to quantitative cell tracking studies by TurboSPI [157]. The slow diffusion model itself is an alternative to the static dephasing regime (SDR) developed by Yablonsky [163], which neglects the diffusion of water molecules. By neglecting diffusion, the SDR is consequently incapable of describing the signal behaviour during the full SE, even though it can give the signal through the FID and at t = TE. Therefore, the SDR is not greatly applicable to TurboSPI studies in which it is the behaviour *throughout* the SE that is most interesting.

The extended SDM model depends on similar system parameters as those described for the Monte Carlo simulation (R, $\Delta\chi$, ζ, D, TE). $\Delta\chi$, D, and R are substituted by new variables, $\delta\omega$, λ. $\delta\omega$ is the characteristic frequency offset [163] for the sphere:

$$\delta\omega = \frac{4}{3}\pi\gamma\Delta\chi B_0 \tag{4.9}$$

And λ describes the diffusion as a dimensionless paramter [157]:

$$\lambda = \frac{D}{R^2\delta\omega} \tag{4.10}$$

These are used in an analytic function that describes the signal from excitation through the spin-echo:

$$f^{SE} = \int_0^{\pi} d\theta \frac{\sin\theta}{2} \int_0^1 \frac{du}{u^2}(1 - e^{-iu(3\cos^2\theta-1)(\tau-\tau_E)-3\lambda\tau^3 F(\tau_E/\tau)u^{8/3}(5\cos^4\theta-2\cos^2\theta+1)}) \tag{4.11}$$

Where the unitless variables (u, τ,τ_E) and function, F(τ_E/τ), are defined as [157]:

$$\begin{aligned} u &= \frac{R^3}{r^3} \\ \tau &= t\delta\omega \\ \tau_E &= TE\delta\omega \\ F &= 1 - \frac{3}{2}(\frac{\tau_E}{\tau})^2 + \frac{3}{4}(\frac{\tau_E}{\tau})^3. \end{aligned} \tag{4.12}$$

A derivation of f^{SE} is beyond the scope of this thesis, but can be found in [158]. The relevance of the function for this work is to show that it is amenable to an added

fat oscillation and agreeable with the simulation over a wide range of experimental conditions. Additionally, the extended slow diffusion model informs certain modifications to the analysis methods discussed in Sections 4.3.1 and 4.3.2.

Equation 4.11 can be calculated via numerical integration and the analytic function is modified to the show the familiar signal, now including N and ζ factors for scaling:

$$S(t) = Ne^{-\zeta f^{SE}} \tag{4.13}$$

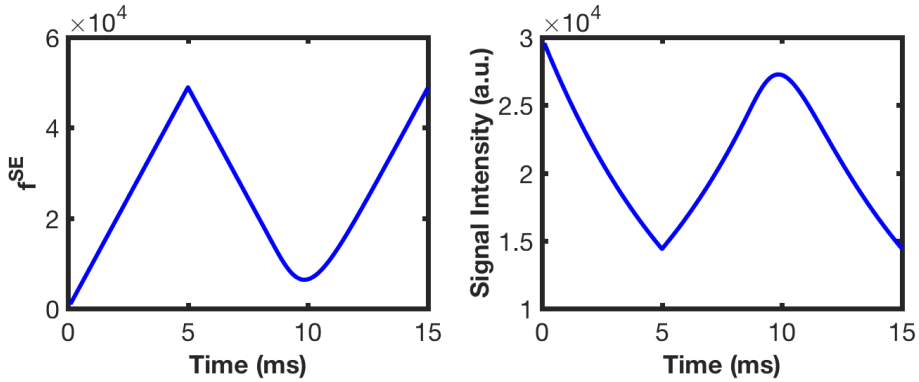

Figure 4.2: An example of the model output showing the f^{SE} function (left) and corresponding signal (right). Input parameters: R = 4, $\Delta\chi = 30\times10^{-3}$, $\zeta = 1.5\times10^{-5}$.

The model agrees well with the simulation for large magnetized spheres using a reasonable diffusion value of D = 1.5×10^{-3} μm$^2/\mu$s, but the signal curves begin to diverge for smaller particles ($< 2\mu$m) with low to moderate susceptibility values.

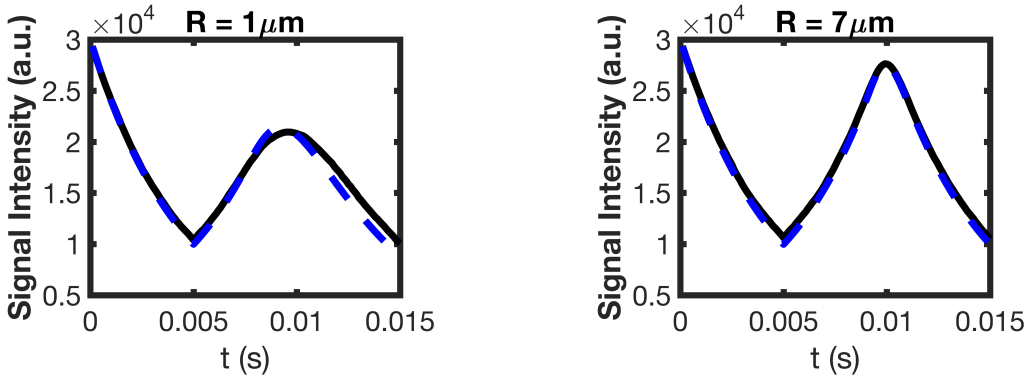

Figure 4.3: Signal time course curves for the Monte Carlo simulation (black) and model (Blue, dashed) for small radii (left) and mid-size radii (right). N = 3×10^4, $\zeta = 1.5\times10^{-5}$ $\Delta\chi = 0.04$. The model deviates from the simulated data for a small perturber

4.1.4 Added Fat

An off-resonance fat oscillation can be added to both the simulation and the model for different fat fractions using Equation 4.5. The fat frequency is obtained using the frequency shift given in Equation 2.43:

$$f_{fat} = \gamma B_0 - \Delta f_{WF} \tag{4.14}$$

And the fat oscillation itself is calculated by:

$$S_f = e^{-i2\pi f_{fat} t} \tag{4.15}$$

The fat oscillation is multiplied by a phase factor before it is added to the simulated or modelled signal curve so that the signal peak aligns with the SE.

Signal curves for the simulation and model continue to agree when fat is added as shown by the time course plots given in Figure 4.4 for a various fat fractions The shape of these curves is similar to *in vitro* data for similar fat fractions.

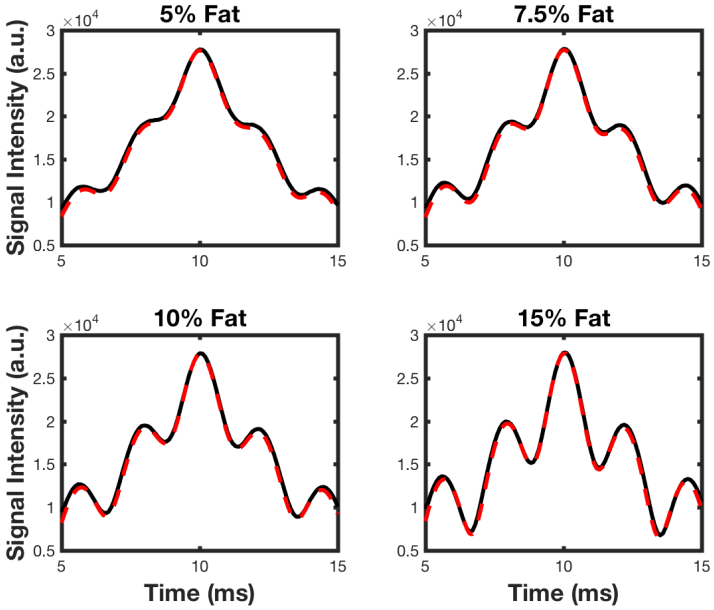

Figure 4.4: Signal time course plot for the simulation (black) and model (red dashed) with fat fractions of 5%, 7.5%,10%, 15%. N = 3×10^4, R = 9μm, ζ = 1.5×10^{-5} $\Delta\chi$ = 0.05. A 2.2 ms period of the fat signal is observed. The "acquisition window" has been shortened to show the SE in a more conventional window as seen for *in vitro*/*in vivo* data.

Changing Parameters

We can compare the model to the simulation over the spin echo using a normalized root mean square error (nRMSE) to examine how well the signal curves agree for a wide range of parameters as is done in Figure 4.5. This was done using a 2D histogram for various size and susceptibility values. Error is quite low (nRMSE <0.03) in the region of interest (reasonable physical parameters) as indicated by the black box on Figure 4.5. The nRMSE rises above 0.04 only for R $\leq$ 1.5μm, which is smaller than any cells we track but larger than individual SPIO nanoparticles. Agreeability appears to increase slightly for low $\Delta\chi$ values, but the best agreement (nRMSE $\leq$0.02) is seen for unreasonably high $\Delta\chi$ and would behave similarly for large ζ values.

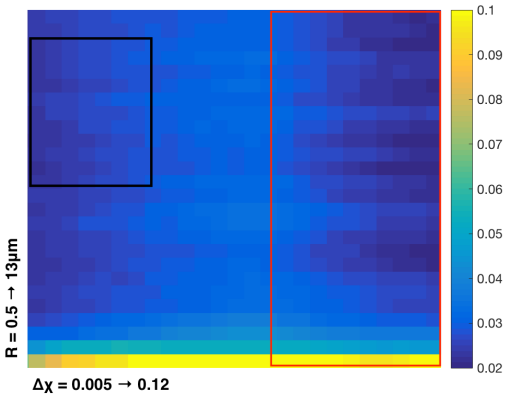

Figure 4.5: A 2D histogram shows the nRMSE between the simulation and model as a function of R and $\Delta\chi$. Reasonable parameters are highlighted by a black box. The red box highlights how agreeability increases further for high susceptibilities (or similarly for high ζ), but these are for example only as they are physically unreasonable. All data were acquired with N = 3×10^4, f = 15%, ζ = 1.5×10^{-5}, D = 1.5×10^{-3}.

It is also useful to consider how the time courses change in shape as a function of R, $\Delta\chi$, and ζ when fat is added as is done in Figures 4.6, 4.7, and 4.8 respectively. These comparisons are instructive since the ability to fit T_2* decay is highly dependent on the time course shape. The plots also illustrate how it can be quite difficult to parse the effects of many changing parameters at once, especially in the presence of fat. However, for the *in vivo* experiments we assume that cell size and cell loading are known, since we are using a known cell type and loading concentration. Therefore, volume fraction and fat fraction are the two effective unknowns.

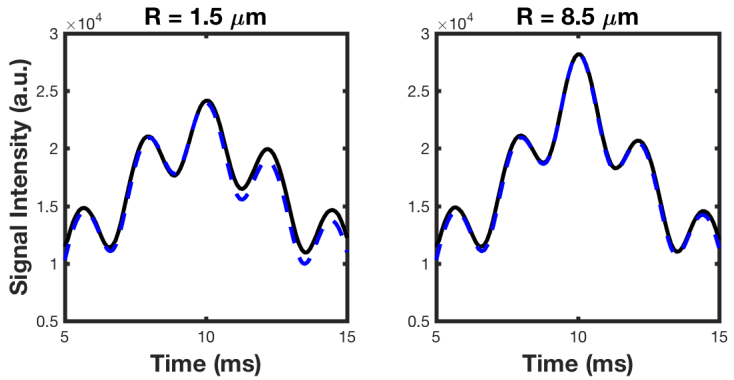

Figure 4.6: How changing R affects signal time course. *$R = 1.5\ \mu m$ (left), $8.5\ \mu m$ (right)*; $\Delta\chi = 0.04$; $\zeta = 1.5{\times}10^{-5}$; f = 10%.

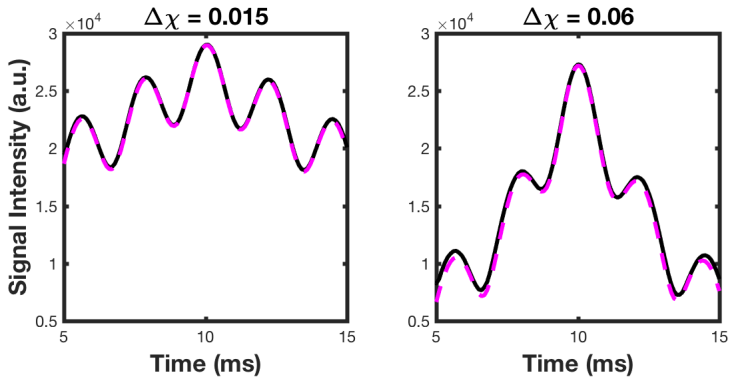

Figure 4.7: How changing $\Delta\chi$ affects signal time course. *$\Delta\chi = 0.015$ (left), 0.06 (right)*; R = 7 μm; $\zeta = 1.5{\times}10^{-5}$, f = 10%.

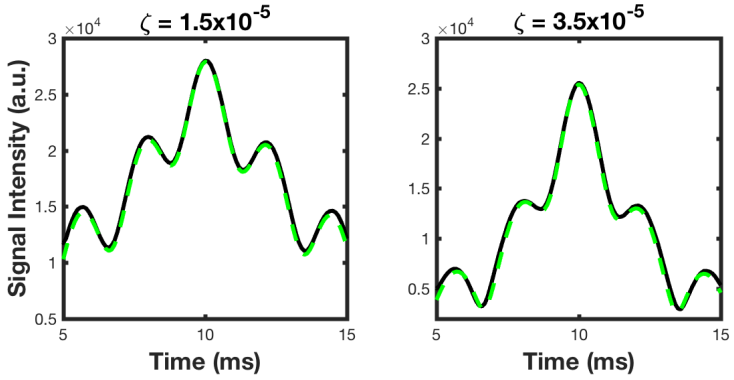

Figure 4.8: How changing ζ affects signal time course. *$\zeta = 1.5{\times}10^{-5}$ (left), $3.5{\times}10^{-5}$ (right)*; R = 7 μm; $\Delta\chi = 0.04$; f = 10%.

Thus far, the simulated and modelled signal have effectively ignored T_2 effects, which allows us to isolate T_2* effects. However, it is not always appropriate to ignore T_2 relaxation completely and it is straightforward to review the effect by adding the exponential decay factor $e^{\frac{-t}{T_2}}$. Note how the amplitude of the SE has decayed in Figure 4.9, since the T_2 dephasing cannot be recovered.

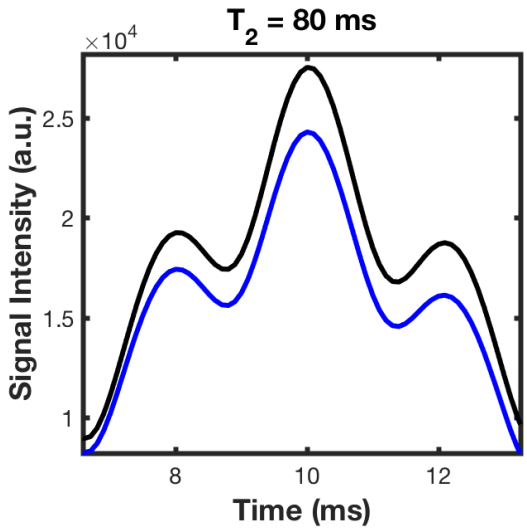

Figure 4.9: Introducing T_2 effect to the signal time course. Negligible ($T_2 > 1$s) effect (black) and strong ($T_2 = 80$ms) effect (blue). R = 7 μm; $\Delta\chi = 0.05$; $\zeta = 1.5\times10^{-5}$; f = 10%.

We can similarly add a T_2* effect to the fat signal. This can either be done to match the effect on water (such that $e^{\frac{-\Delta t}{T^*_{2W}}} = e^{\frac{-\Delta t}{T^*_{2F}}}$) or as a unique relaxation for the fat isochromat ($e^{\frac{-\Delta t}{T^*_{2W}}} \neq e^{\frac{-\Delta t}{T^*_{2F}}}$), as discussed in Section 2.8.1.

4.1.5 Analysis Goals

The aim of this project is to estimate the number of cells per voxel (or perturbers per simulated voxel) in the presence of fat. While the analytic model certainly agrees well with the simulation over a wide range of conditions, it is difficult to fit real (and simulated) data to extract and decouple the parameters of interest. That is, we are mainly interested in ζ, but this parameter must be separated from contributions of R, $\Delta\chi$, and D (through λ and $\delta\omega$). Adding the fat term introduces a further complication

and parameter to fit. In particular, notice the similarity in shape for high $\Delta\chi$ and ζ (Figures 4.7 and 4.8 right panel). For this reason, we will focus our analysis to the fat-water model in Equation 4.5 with T_2* decay from Equation 2.51 to determine *fat fraction* and *T_2**. For *in vivo* studies, we can then obtain *cell number* using the calibration curve.

4.2 Estimation and Signal Subtraction

Our first analysis goal was to reliably estimate the fat fraction such that *ff* becomes a known variable and we could use it to obtain an accurate value for T_2*. *In silico* data offered an ideal framework for this endeavour: since we input known amounts of fat signal, it is straightforward to assess the efficacy of the fat fraction recovery. Likewise, in moving on to the T_2* estimate, we can compare to data without added fat oscillation.

4.2.1 Two-Point Dixon

We started with the simple two-point Dixon method that was described in Section 2.8.1. This was mainly performed as a simple proof of concept to show that TurboSPI data (*in silico* and beyond) is amenable to Dixon type analysis. The ancillary objective was to ascertain the degree to which T_2* line-broadening affects the method.

For the two-point method we used the 0 and π versus 0 and -π angles which correspond to t = TE and t = TE $\pm$ 1.1 ms time points. Table 4.1 gives an example of the initial fat estimates using this technique for both sets of phase angles.

Table 4.1: Recovery of Known Fat Fractions: 2pt. Dixon. R = 7μm; $\Delta\chi$ = 0.05; ζ = 1.5$\times 10^{-5}$

Fat% Input	Fat%: Sim. π	Fat%: Sim -π	Fat%: Model π	Fat%: Model -π
0	8.02	7.77	8.15	8.04
10	18.00	17.57	18.07	18.01
30	37.48	37.08	37.57	36.54
70	74.32	74.14	74.40	74.39
100	99.97	99.97	99.97	99.97

Clearly, this technique is susceptible to overestimating the fat fraction. Furthermore, it appears to overestimate *ff* as a function of relative perturber content. That is, the recovered fractions are closer to the known input values for higher relative fat content. High fat content corresponds to low relative water content and thus diminished T_2* effect since the perturber simulation is performed for the water component.

This is illustrated in Figure 4.10 (right) which demonstrates how the difference between the estimated and known fat fractions (Δff) increases as a function of water fraction. It also shows the linear relationship between the estimated *ff* and known *ff*.

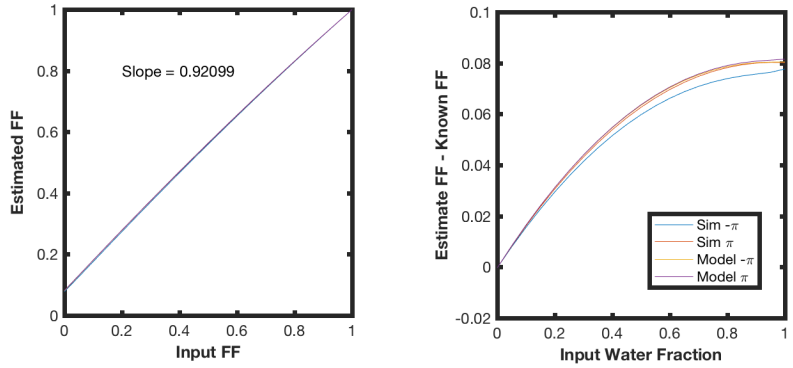

Figure 4.10: Left: a plot of estimated *ff* versus knwon *ff* showing linearity and a slope of 0.92. Right: a plot of the different between estimate and input FF versus water fraction showing how Δff increases with increased water content (and thus simulated SPIO effect). R = 7μm; $\Delta\chi = 0.05$; $\zeta = 1.5\times10^{-5}$

These results are not necessarily surprising. Rather than interpreting Figure 4.10 as the Δff increasing with increased water content, we can describe Δff as increasing with increased SPIO effect from T_2* line-broadening of the water species. After all, it is the SPIO in the cells that drive the disparity between known and estimated fat fraction. Therefore, it is not sufficient to investigate the effect for just one set of parameters, since just as Δff increases here for a larger water (and thus "cell") to fat ratio, it will change for different experimental conditions.

Figures 4.11, 4.12, and, 4.13 illustrate how these plots change for different susceptibility values, volume fractions, and radii, respectively. In each case, we observe a decreased slope (farther from unity) for the estimated versus input *ff* when the SPIO effect is enhanced from increased $\Delta\chi$, R, or ζ.

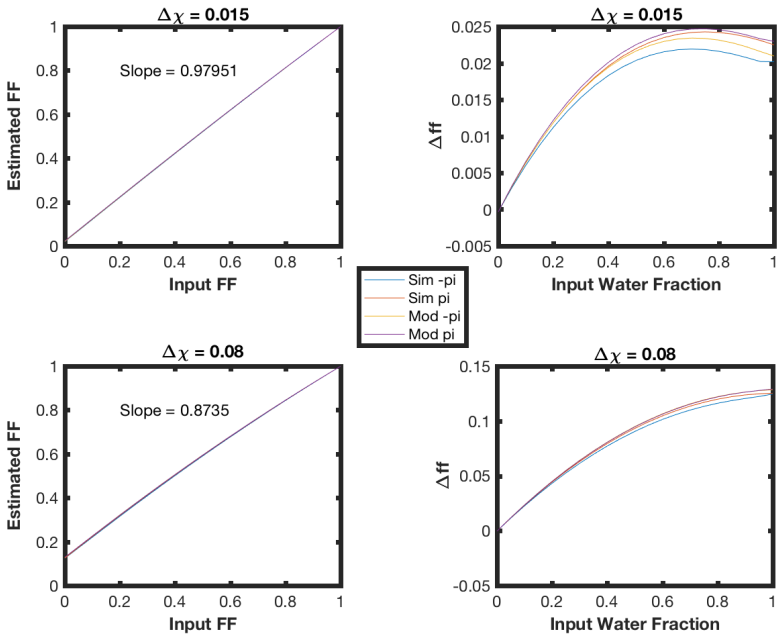

Figure 4.11: Comparison of SPIO effect on *ff* recovery for different susceptibility values that shows Estimated FF vs. Known FF and how Δff changes with relative water and "cell" fraction. R = 7μm; $\Delta\chi$ = 0.015 (top), 0.08 (bottom); $\zeta = 1.5\times10^{-5}$

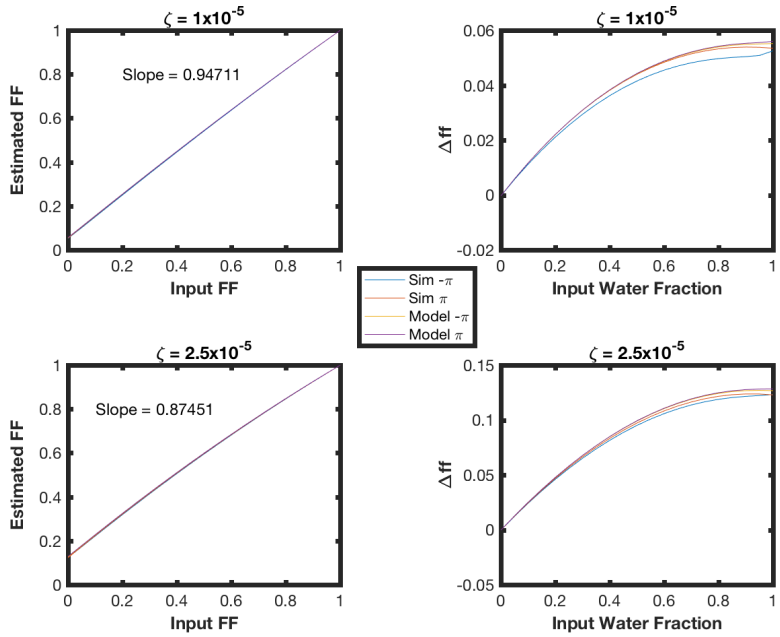

Figure 4.12: Comparison of SPIO effect on *ff* recovery for different volume fractions that shows Estimated FF vs. Known FF and how Δff changes with relative water and "cell" fraction. R = 7μm; $\Delta\chi$ = 0.05; $\zeta = 1.0\times10^{-5}$ (top), 2.5×10^{-5} (bottom)

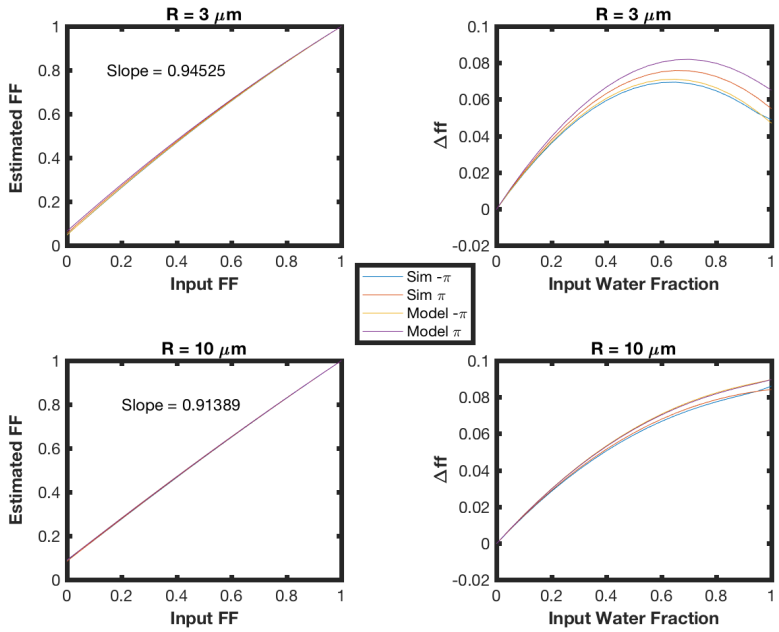

Figure 4.13: Comparison of SPIO effect on *ff* recovery for different radii that shows Estimated FF vs. Known FF and how Δff changes with relative water and "cell" fraction. R = 3μm (top), 10μm (bottom); $\Delta\chi = 0.05$; $\zeta = 1.5\times10^{-5}$

The technique never overestimates the fat content beyond 100%, as is demonstrated in these plots of *estimated* versus *input ff* in which the maximum value is always ≈ 1. Therefore, the initial offset (y-intercept) and the slope both change (offset increases when slope decreases). These plots are consistently linear: the R^2 goodness of fit value is greater than 0.997 for all cases. Therefore, it is feasible to use the linear fit to determine an accurate estimate of input *ff*.

4.2.2 Scaled Signal Subtraction

After obtaining a value for the fat fraction the next logical step is using that information to correct the data. Our first trial was to uncover the original (i.e. without fat) signal time course from the *in silico* data using a *scaled subtraction*. This technique subtracts a fat signal that is multiplied by a scaling factor equal to *ff*. The methodology is quite simple: use the recovered *ff* and the known fat signal (S_f) to separate S_w from S in Equation 4.5. If recovered correctly, the isolated water signal will yield the correct T_2* value after fitting.

Understandably, the scaled subtraction technique is highly dependent on the accuracy of the *ff* estimation. Figure 4.14 (bottom left) illustrates the consequence of using the original (overestimated) *ff* estimate from simple two-point Dixon. The signal time course is still modulated, but now from subtracting more fat than ever existed in the signal. For *in silico* data there exists a stable linear relationship between known and estimate *ff* for two-point Dixon, as demonstrated above. We can obtain "corrected" values of *ff* using the slope and intercept. Naturally, a more accurate *ff* gives rise to a more accurate decomposition of the signal as illustrated in Figure 4.14 (bottom right). The *corrected subtraction* data are very similar to the original signal. The RMSE between the curves are 3.7×10^{-4} and 6.0×10^{-3} (in normalized signal intensity) for the simulation and model, respectively.

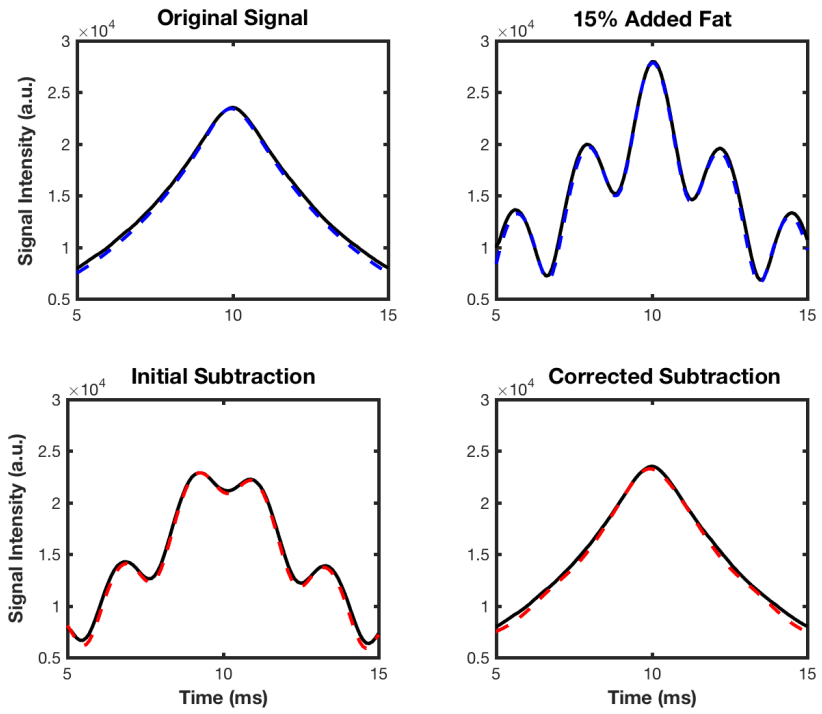

Figure 4.14: Plots to illustrate the *scaled subtraction* technique. Simulation time course is shown as a solid line, and the model is shown as a dashed line. Top left: original unmodulated signal for both simulation and model. Top right: the modulated signal from addition of fat oscillation (15%). Bottom left: Initial fat subtraction using the *ff* obtained from the initial *ff* two-point Dixon technique. Bottom right: the "corrected" subtraction that uses a corrected *ff*

This is clearly a very well defined and simple problem *in silico* since the fat signal (S_f) is known and we are able to obtain an accurate estimate of *ff*. The slope and intercept used to correct the two-point Dixon fat estimate were obtained by taking a "rough estimate" from different ζ values to emulate a (small) degree of the uncertainty found in physical experiment. However, this is a simple demonstration to illustrate the technique under ideal conditions and ζ was not varied greatly (1.3×10^{-5} to 1.7×10^{-5}).

Unfortunately, a scaled subtraction is impractical for *in vitro* and *in vivo* studies for a number of reasons. In a typical physical study, R and $\Delta\chi$ may be considered fixed parameters, but cell volume fraction is, of course, an unknown that can change appreciably. While the fat subtraction is robust to small changes in slope and intercept (from changing ζ), as demonstrated above, the fidelity of the technique will deteriorate for larger Δff. Secondly, the *ff* "correction" accounts for T_2* effect on the fat fraction, but the method neglects T_2* decay to fat signal in the subtraction itself, which may not be a reasonable assumption.

Finally, we must note that the *in silico* work is simplified greatly by the fact that S_f is well characterized and *known*. Indeed it is the same oscillation that was added initially. For *in vitro* and *in vivo* data, the signal may not be a simple composition of an unknown signal (S_w) and an ideal, known, well characterized synthetic signal (S_f).

4.2.3 Three-Point Dixon

Moving to a *three-point* implementation is normally the first step to improve upon two-point Dixon. As described in 2.8.1, using a third measurement enables one to correct for the phase error from B_o inhomogeneity. Typically, this phase correction is quite important for real data but not for *in silico* data. For *in silico* data we can assume that our magnetic field is ideal and homogenous. This assumption is clearly valid unless we are simulating or modelling B_o heterogeneity. In this work we consider an "ideal experiment" in that we are not simulating any macroscopic hardware induced B_o inhomogeneities. However, we are introducing local inhomogeneities to the voxel from the spherical perturbers. Indeed, the entire purpose of the simulation is to probe how the system responds to intentional changes.

Since we are introducing inhomogeneity, it is prudent to check how phase changes throughout the signal time course before any fat oscillation is added, as is done in Figure 4.15. A fat oscillation merely adds a periodic modulation whose amplitude depends on *ff*.

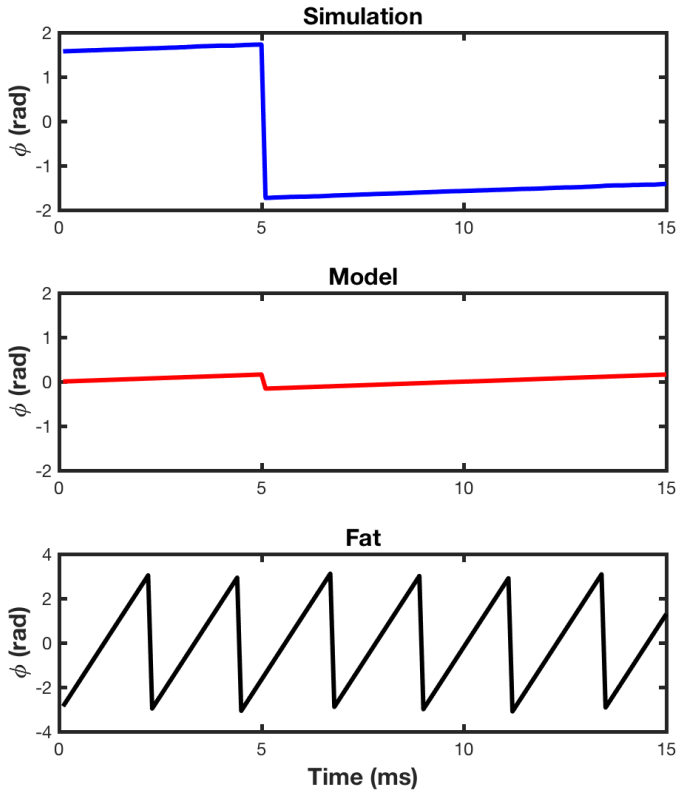

Figure 4.15: Plots of phase versus time for the Simulation (top), the Model (bottom), and the Fat signal (bottom). In the simulation, ϕ starts at $\pi/2$ from the initial 90° pulse and is tipped by π at TE/2 for the refocusing pulse. The model starts with $\phi = 0$ and the refocusing pulse appears to induce $\Delta\phi \approx \pi/10$. However after TE/2 the model and simulation phases change at approximately the same minimal rate (0.032 rad/ms). The fat signal shows $\phi = 0$ at $\approx$ 10 ms (TE) and exhibits phase wrapping.

The f^{SE} for the model includes a $e^{i(\tau-\tau_E)}$ term that depends on both time and $\delta\omega$ (and thus $\Delta\chi$) and this explains the small time dependent phase change in Figure 4.15. While there is a phase effect before the added fat oscillation, it is quite gradual (after the 180° pulse). This small effect cannot account for the errors observed in recovering known fat fractions. Therefore, we can confirm that the main effect driving Δff is

T_2* line-broadening so a phase correction alone will not significantly improve the *in silico* data.

4.3 Curve Fitting

The results in Section 4.2 demonstrate the need for combined T_2* and fat estimation in our system. Naturally, increasing the number of unknowns necessitates an increase in the number of measurements, which TurboSPI data (simulated or otherwise) are well equipped to provide. The algebraic calculations performed above become more tedious and less feasible for more equations. For this reason, curve fitting may be a superior option since TurboSPI has a high temporal resolution with many measurements available and thus points to fit.

All curve fitting was performed in Matlab using *lsqcurvefit* and the work focused on the Monte Carlo simulation data.

4.3.1 Preliminary Investigation

We start with a modified version of simple fat and water model presented in Equation 2.44.

$$S = [We^{-\Delta t/T_2*} + Fe^{i\alpha}]e^{i\phi_0} \tag{4.16}$$

The modification removes spatial dependence for application to "single voxel" simulations. Likewise, we neglect the time dependant phase term ϕ(t) that reflects B_0 inhomogeneity, since the simulation is performed under "ideal" conditions. Technically, the additional time independent, phase term ϕ_0 could be similarly removed, but we found that *ff* and T_2* results were not majorly affected by its inclusion contrary to the ϕ(t) term.

This simplified equation does not include the T_2* decay on fat that was not initially simulated nor the small phase phase effected noted in Figure 4.15. These effects will be added in the next section. Additionally, this preliminary exploration simply fits the complex data that is output from the simulation, which is helpful for visualizing the data in our familiar signal time course. This method is not robust to *in vitro/vivo* data, for which the function will need to be split into *real* and *imaginary*

parts that are fit separately.

Figure 4.16 shows an example of the preliminary fit for a time course with 15% fat from t = 10.5 ms → 12.5 ms. The simulated and function data are very agreeable over this region with an RMSE of 0.0018 and the success is well demonstrated by the corresponding *ff* and $T_2{}^*$ estimates which are similar to the input parameters (Table 4.3). Table 4.2 gives the initial estimates for each parameter. *Lsqcurvefit* does not consider bounds when fitting complex functions. However we confirmed that the parameters never took unreasonable values, in fact, the values naturally fell within the bounds used for *Real/Imaginary* fitting in the next section (Table 4.4).

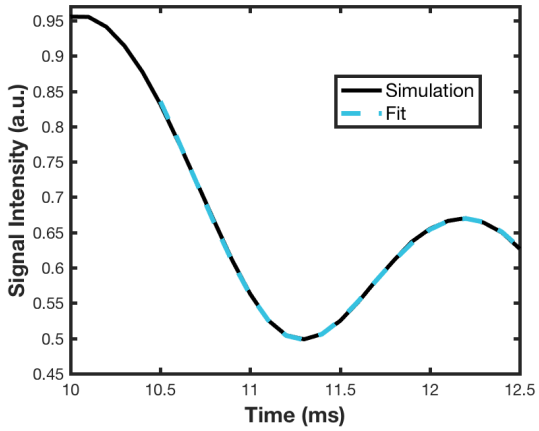

Figure 4.16: Normalized simulated data (solid black) with the corresponding fit (dashed blue) using Equation 4.16. *ff* = 0.15; $\zeta = 1.5\times10^{-5}$; R = 8μm ; $\Delta\chi$ = 0.05

Table 4.2: Initial guesses used in the optimization

	Relative Water Signal	Relative Fat Signal	$T_2{}^*$	ϕ_0
Initial Guess	0.5	0.5	10	0

Note that Figure 4.16 shows how the fit is only performed on a portion of the decay (t > 10.5 ms). This is done to steer clear of the SE peak at which there exists a time-dependant deviation from the mono-exponential behaviour that the fat-water-$T_2{}^*$ model (Equation 4.16) assumes.

In his work on the slow diffusion model [159], Kiselev describes how a non-zero

λ (i.e. the presence of diffusion) gives rise to secondary time dependent attenuation. This is seen in the extended slow diffusion function (Equation 4.11) by the time dependent function $F(\frac{\tau_E}{\tau})$ that is multiplied by λ in second term of the exponential. When we move away from TE the $F(\frac{\tau_E}{\tau})$ factor approaches one and the deviation becomes stable.

The relaxation behaviour is greatly simplified when $\lambda = 0$ by not allowing diffusion during the simulation. This is demonstrated by Figure 4.17 which shows simulated data with and without diffusion, however we will include diffusion in the simulations so that the analysis can be more scalable to realistic systems. We note that the left panel of Figure 4.17 exhibits complete signal refocusing at the echo since T_2 is long and there is no attenuation from diffusion. The right panel shows signal attenuation and non-linear-exponential behaviour when t $\approx$ TE, but the at later time points the decay is similar to that in the left panel.

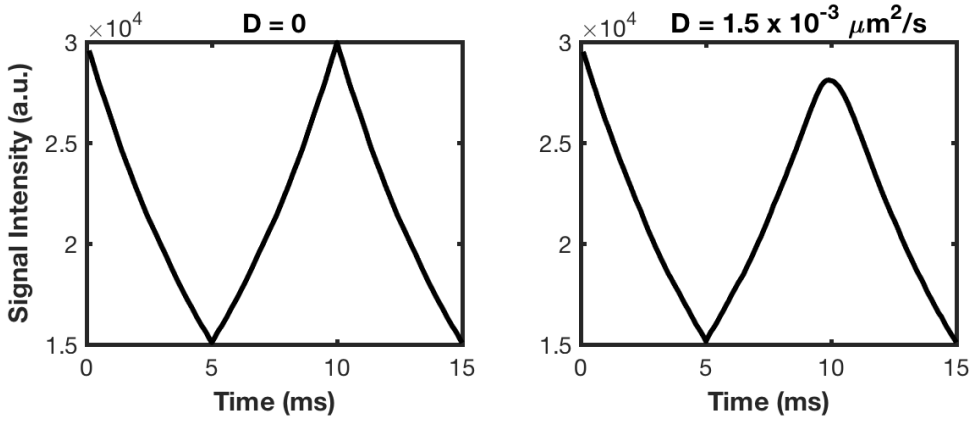

Figure 4.17: Simulated data without diffusion D = 0 μm^2/s (left) showing complete refocusing. Simulation with diffusion D = 1.5 $\times$ 10^{-3} μm^2/s (right) showing incomplete refocusing and a curved peak. Other parameters: R = 7 μm; $\zeta = 1.5 \times 10^{-5}$; $\Delta\chi = 0.03$

Since Equation 4.16 assumes a exponential T_2* decay on the water signal, it is wise to begin fitting at t > TE to limit the effect of $F(\frac{\tau_E}{\tau})$. We can compare the T_2* estimate to a value obtained from fitting a simulation without diffusion (Table 4.3). Moving away from TE will ameliorate the fit, but diffusion is still present so it is not expected that these values agree exactly.

The estimated *ff* is compared to the input *ff* as before and, more importantly,

the T_2* can be compared to a *gold standard*. The gold standard T_2* is obtained by fitting simulated data without added fat with the exponential fit used in previous TurboSPI analysis methods that don't consider fat oscillation ($Ae^{-R_{2*}t}$).

Table 4.3: Comparison of estimated *ff* to the ground truth (GT) *ff* for varied fat content and estimated T_2* to gold standard (GS) T_2* taken from the previous method applied to a simulation without fat.

GT Fat%	Fit Fat%	T_2* $\text{Fit}_{D=1.5^{-3}}$ / $\text{Fit}_{D=0}$ (ms)	T_2* $\text{GS}_{D=1.5^{-3}}$ / $\text{GS}_{D=0}$ (ms)
0	0.16	4.38 / 4.32	4.50 / 4.41
5	4.96	4.38 / 4.32	not applicable
15	15.10	4.38 / 4.32	not applicable
45	45.44	4.38 / 4.32	not applicable

The data above suggest that both the *ff* and T_2* estimates are robust to changes in fat simulated fat versus water content (with SPIO loaded "cells") . We assess the *ff* estimates by stepping through known fat fractions, performing the fit and plotting the output *ff*, as we did for the two-point method. Figure 4.18 shows the linear *estimated ff* vs *input ff* relationship with a slope and y-intercept of 1.0026 and 0.0016, respectively. These values are much closer to the identity line (slope = 1, y-intercept = 0) than those calculated from two-point Dixon (Figures 4.10 to 4.13). The RMSE between the estimate and identity line is 0.0034 giving estimated ff ± 0.3%. Maximum differences (0.5%) are observed from 57% fat to 65% fat.

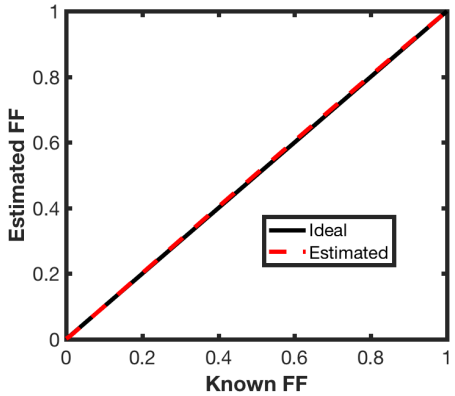

Figure 4.18: Fitted fat fraction versus input fat fraction (dashed red) with an identity line (black) for reference. Other parameters: R = 8 μm; $\zeta = 1.5 \times 10^{-5}$; $\Delta\chi = 0.05$

As we learned from the scaled signal subtraction in Section 4.2, accurate *ff* estimates are not very useful unless they correspond to improvements in T_2* fitting as well. We can assess the T_2* estimate as a function of input *ff* where success is measured by continuity. When fit properly, the water and fat terms of Equation 4.16 are separated appropriately and T_2* is invariant to *ff*. This stable behaviour is observed in most of Figure 4.19, but the fit deteriorates at $ff = 1$. Standard deviation of the measurements is 0.34 ms, however this value is heavily biased by the failure to fit T_2* decay when no "W" signal is present. If standard deviation is taken from 0 to 99 % fat, the value becomes 0.002 ms.

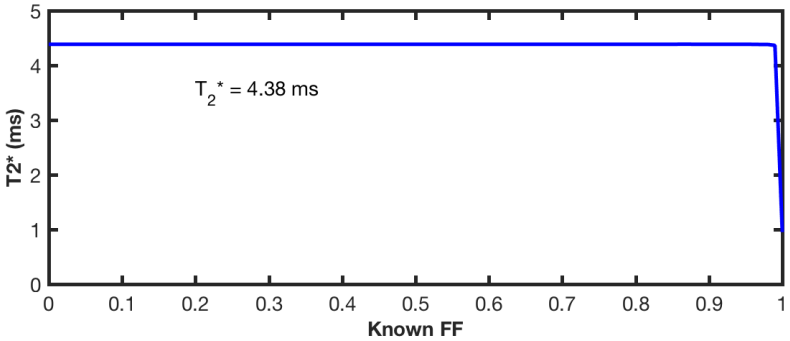

Figure 4.19: Fitted T_2* versus input fat fraction. Other parameters: R = 8 μm; $\zeta = 1.5 \times 10^{-5}$; $\Delta\chi = 0.05$

Lastly, we assess how the T_2* fit responds to different volume fractions. Does it change appropriately for different ζ values and thus differing extent of "SPIO" related dephasing?

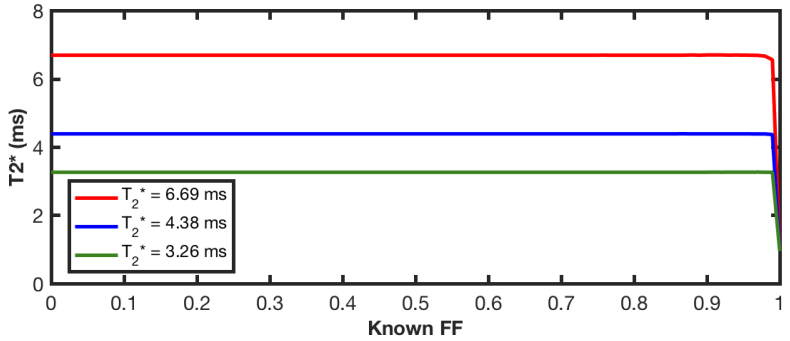

Figure 4.20: Fitted T_2* versus input fat fraction for $\zeta = 1.0 \times 10^{-5}$ (red); 1.5×10^{-5} (blue), 2.0×10^{-5} (green) . Other parameters: R = 8 μm; $\Delta\chi = 0.05$

Table 4.3 shows that the fit returns similar T_2* to the gold standard, Figure 4.19 shows that the estimate is stable across most *ff*, and Figure 4.20 demonstrates how T_2* changes appropriately for different volumes fractions (slower $T2_2$* for higher ζ, longer T_2* for lower ζ). Even in this preliminary work we find that, when fat is present, fitting *ff* and T_2* simultaneously provides better estimates of both parameters.

4.3.2 Advanced Investigation

The above work is sufficient for a proof of concept, but it requires adjustment if we want the curve fitting to be scalable to real data.

First, we introduce a T_{2F}* effect on the fat term. We allow the relaxation value to be unique to the fat isochromat, rather than using an average T_2* for the mixture as was done in the model by Glover [134]. Therefore, Equation 4.16 becomes:

$$S = [We^{-\Delta t/T_{2W}*} + Fe^{i\alpha}e^{-\Delta t/T_{2F}*}]e^{i\phi_0} \tag{4.17}$$

T_{2W}* arises from the simulation and $T_{2F}*$ is added explicitly to the fat term. To conform to literature that describes a average T_2* value for the mixture [134] we could fit a common T_2*. However, the average will clearly change with *ff* unless the decay terms are equal. We can design a common T_2* = T_{2F}* = T_{2W}*, but it is also interesting to let these species relax at different rates and analyze them separately. The *in silico* framework is well equipped to handle each of these options.

Next, we will add the time dependent phase term, $e^{i(\tau-\tau_E)}$ in f^{SE}, to be fit as well. The value will be small, as illustrated in Figure 4.15, but its inclusion may offer a more comprehensive description of the behaviour. Equation 4.17 is adapted by the inclusion of this θ_τ term:

$$S = [We^{-\Delta t/T_{2W}*}e^{i\theta_\tau \Delta t} + Fe^{i\alpha}e^{-\Delta t/T_{2F}*}]e^{i\phi_0} \tag{4.18}$$

The last adjustment does not involve adding additional fit parameters, but rather changing the way the fit is performed. As noted earlier, using bounds is not supported when fitting complex functions in Matlab. It is beneficial to move towards bounded optimization since we are both adding new parameters to fit and eventually moving towards less ideal *in vitro/vivo* data. Therefore, we have re-parameterized the fit into real and imaginary components.

$$Re = [We^{-\Delta t/T_{2W}*}\cos(\theta_w + \theta_\tau \Delta t) + Fe^{-\Delta t/T_{2F}*}\cos(\theta_f + \Delta\omega_{WF}\Delta t)] \quad (4.19)$$
$$Im = [We^{-\Delta t/T_{2W}*}\sin(\theta_w + \theta_\tau \Delta t) + Fe^{-\Delta t/T_{2F}*}\sin(\theta_f + \Delta\omega_{WF}\Delta t)]$$

Where $\theta_{w,f}$ represent the time-independent phase on water and fat, and α is re-written as $\Delta\omega_{WF}\Delta t$ (by Equation 2.45) to explicitly show its time dependence. For *in vitro* and *in vivo* data, θ_τ and ω_{WF} are allowed to vary to represent ϕ. To prepare for fitting, the simulation data are split into real and imaginary components and concatenated into a long vector to match the function that is split similarly.

Table 4.4: Initial guesses and bounds used in the optimization.

	W	F	T_{2W}*	T_{2F}*	$\theta_{w,f}$	θ_τ
Initial Guess	0.5	0.5	10	10	0	0
Lower Bound	0	0	1	3	-π	-π
Upper Bound	1	1	30	50	π	π

Figure 4.21 shows an example of a fitted real-imaginary function that matches well with the simulated data, although it is less visually intuitive as signal time course than Figure 4.16. Table 4.5 gives the corresponding T_{2W}*, T_{2F},* and *ff* estimates.

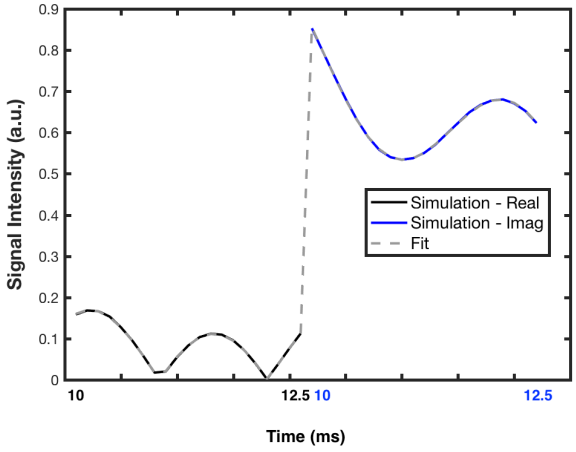

Figure 4.21: Normalized simulated data (solid black) with the corresponding fit (dashed grey) both split as [Real, Imaginary] using Equation 4.19. RMSE = 9.4 $\times 10^{-4}$. *ff* = 0.15; T_{2F}= 15 ms; $\zeta = 1.5\times10^{-5}$; R = 8μm ; $\Delta\chi = 0.05$

Table 4.5: Comparison of estimated *ff* to the GT *ff*, T_{2F}* to GT, and T_{2W}* to GS T_2*= *4.5 ms*. The second row neglects fat T_{2F}*.

GT Fat%	Fit Fat%	GT T_{2F}* (ms)	T_{2F}* (ms)	Fit T_{2W}* (ms)
15	14.2	15	*34.9*	4.31
15	15.07	/	/	4.41

While the T_{2W}* is similar to the estimate that we found previously (Table 4.3), the T_{2F}* value is much larger than the input value. This is not a catastrophic failure since we are, after all, searching for the T_2* on water and thus consistency in T_{2W}* is most important. We check consistency by plotting the T_{2W}* by input *ff* in Figure 4.22. This figure also shows the less important, but still interesting *ff* estimations and T_{2F}* behaviour.

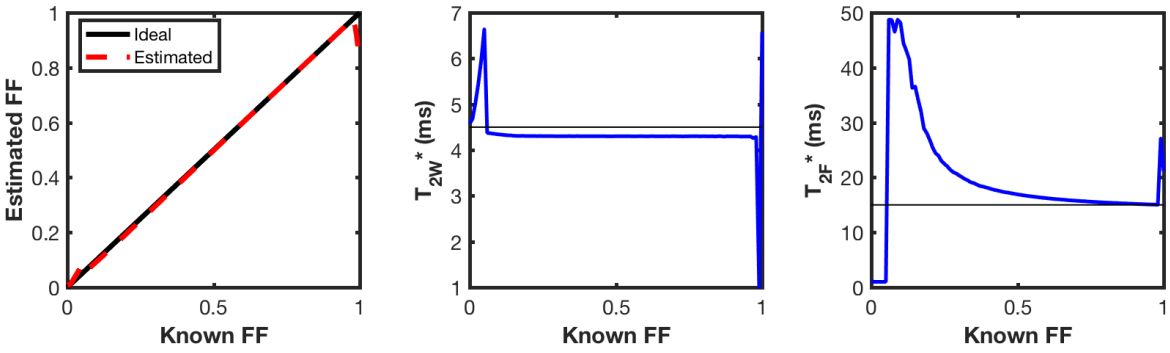

Figure 4.22: Left: Fitted fat fraction versus input fat fraction (dashed red) with an identity line (black) for reference. Middle: Fitted T_{2W}* versus input fat fraction. The fine black line indicates the gold standard T_{2W}*. Right: Fitted T_{2F}* versus input fat fraction. The fine black line indicates the ground truth T_{2F}*.

The estimated *ff* agree well with the input *ff* except for very high or low fat content. Similarly, the T_{2W}* estimate is stable over the same input *ff*. The T_{2W} data are not as consistent as they were for the preliminary fitting technique (Figure 4.19), but this is not necessarily surprising, since we have added two more parameters to the fit. The T_{2F}* fit fails for low input *ff* but trends toward the input value (15 ms) as the relative fat signal grows stronger. Fitting errors arise when either the water or fat signal goes to zero, but the estimates improve when there is adequate signal to

separate.

Letting the exponential decay go to one (i.e. T_{2F}* becomes very large) effectively neglects the T_{2F}*. The signal model becomes similar to that in the *Preliminary Work* section, although it has the time-dependent phase term $e^{i\Delta t\theta_\tau}$. This improves the T_{2W}* stability, as demonstrated by Figure 4.23. Removing T_{2F}* effect from the simulation is simple, but it may not be reasonable to ignore the fat decay in real data.

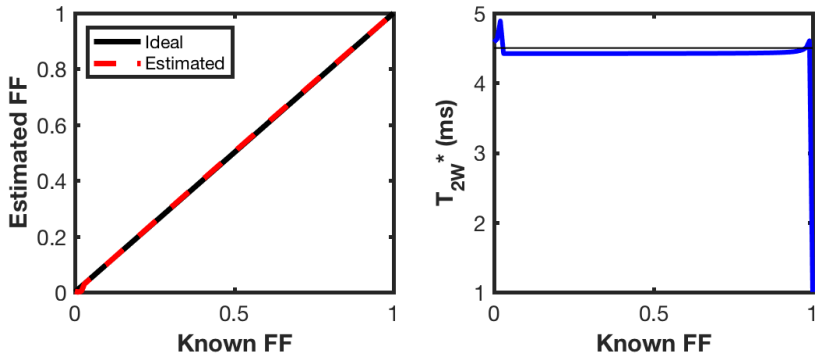

Figure 4.23: Left: Fitted fat fraction versus input fat fraction (dashed red) with an identity line (black) for reference. Right: Fitted T_{2W}* versus input fat fraction. The fine black line indicates the gold standard T_{2W}*. T_{2F}* = 10s to neglect decay.

We can also synthesize a common T_2* that should not vary considerably with fat content by letting T_{2F}* = T_{2W}*. This is done by first fitting T_{2W}* when fat decay is neglected (as is done above) and then setting T_{2F}* equal to this value. Finally, we fit with T_2 as the shared decay parameter.

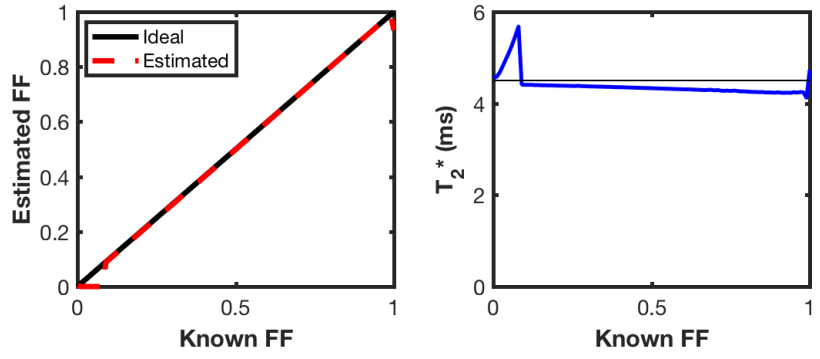

Figure 4.24: Left: Fitted fat fraction versus input fat fraction (dashed red) with an identity line (black) for reference. Right: Fitted "common" T_2* versus input fat fraction. The fine black line indicates the gold standard T_2*.

The common T_2* data are reasonably consistent, performing better at the *ff* extrema than previous fits. However, this is a simplification since it is not realistic to expect fat and water to have the same T_2* decay. If $T_{2F} \neq T_{2W}$, the "common" T_2* will be an average that changes with fat content - a feature we are trying to avoid.

4.3.3 Noise Performance

Until now, we have described ideal signal behaviour in the absence of background noise. To prepare for analyzing real data from *in vitro* or *in vivo* samples we must consider how the fitter performs for non-ideal data with low signal to noise ratio (SNR), specifically in the temporal domain.

We investigate the viability of curve fitting data with low temporal SNR (tSNR) data by adding white Gaussian noise to the total signal using the *awgn* function in Matlab. We step through low to high tSNR and observe how the estimates of *ff* and T_{2W}* respond. For each noise level we perform N fits to yield N estimates of *ff* and T_{2W}*. We calculate the mean and standard deviation of these parameters and plot as a function of tSNR. This is done for a variety of *ff* values. Figures 4.25 to 4.27 show the results for three fit types.

***1. Preliminary Investigation**: Complex fit that neglects both θ_τ and T_{2F}**

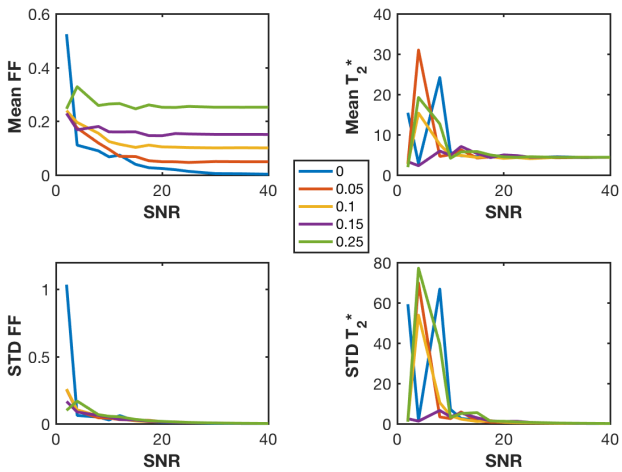

Figure 4.25: Preliminary fit. Top Left: Mean *ff* estimate by tSNR for *ff* = 0 (blue), 0.05 (orange), 0.1 (yellow), 0.15 (purple), 0.25 (green). Top right: Mean T_2 estimate by tSNR for the same *ff*. Bottom row shows corresponding standard deviation (STD) for *ff* estimate (left) and T_2* estimate (right). Means and STDs are from N = 20 estimates (from fitting N = 20 data sets with simulated noise)

For this fit type the *ff* and T_{2W}* are very stable for tSNR ≈ 13 and beyond. However, below tSNR ≈ 13, the errors between the estimate and known values are much larger than in Figure 4.26 below, perhaps due to the inability to bound complex data. Consequences of poor tSNR are most drastic for this technique, but as we will not be using it to fit *in vitro/vivo* data, this is shown for example only.

2. Advanced Investigation A*: Real/Imaginary fit that neglects T_{2F}* but includes the θ_τ term*

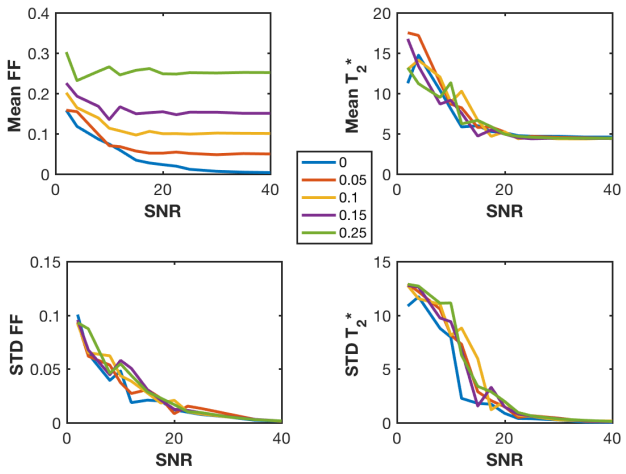

Figure 4.26: Advanced fit A. Top Left: Mean *ff* estimate by tSNR for *ff* = 0 (blue), 0.05 (orange), 0.1 (yellow), 0.15 (purple), 0.25 (green). Top right: Mean T_2 estimate by tSNR for the same *ff*. Bottom row shows corresponding standard deviation (STD) for *ff* estimate (left) and T_2* estimate (right). Means and STDs are from N = 20 estimates (from fitting N = 20 data sets with simulated noise)

This technique results in less extreme errors for low tSNR than those shown in Figure 4.25, possibly by virtue of its bounded optimization. However, contrary to the *preliminary fit*, the data do not begin to stabilize until tSNR ≈ 20. This technique is sensitive to lower noise levels, but its failures are not as dramatic.

3. Advanced Investigation B*: Real/Imaginary fit that fits separate T_{2W}* and T_{2F}* and includes the θ_τ term*

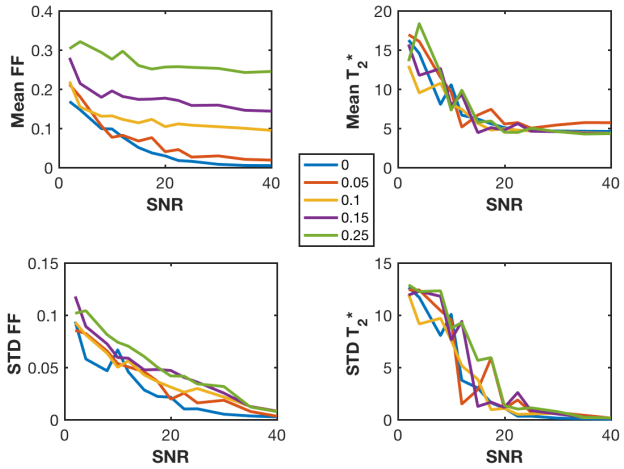

Figure 4.27: Advanced fit B. Top Left: Mean *ff* estimate by tSNR for *ff* = 0 (blue), 0.05 (orange), 0.1 (yellow), 0.15 (purple), 0.25 (green). Top right: Mean T_2 estimate by tSNR for the same *ff*. Bottom row shows corresponding standard deviation (STD) for *ff* estimate (left) and T_2* estimate (right). Means and STDs are from N = 20 estimates (from fitting N = 20 data sets with simulated noise). *The small T_2* error at ff = 0.05 matches the data in Figure 4.22*

This is our most comprehensive fit model that includes separate decay factors for water and fat, includes the small phase change θ_τ, and fits by splitting the data into real and imaginary components. As we saw in Figure 4.22, the increase in fit parameters corresponds to poorer predictive performance, especially at *ff* extrema. Nonetheless, this technique has adequate tSNR performance relative to *Advanced Investigation A* which includes one less parameter. The mean estimates plateau at tSNR $\approx$ 20, as before. However, the standard deviation of the measurements has increased for low noise data, especially for *ff*.

These plots indicate that noise performance may be an issue when fitting *in vitro* and *in vivo* data.

4.4 *In Silico* Summary and Conclusions

We investigated the effect of adding a 3.5 ppm shifted fat oscillation to simulated and modelled data, in particular how the signal time course changes for different fat fractions, volume fractions, particle size, and change in susceptibility. The extended

slow diffusion model agrees well with the simulated data over a wide range of experimental parameters.

We investigated different methods of fat correction, first through Dixon based arithmetic and a signal subtraction. Two-point Dixon overestimated *ff* relative to SPIO content and the signal subtraction was very sensitive to *ff*. Therefore, this technique was not feasible for real data. *Three-point* Dixon will only minimally help *in silico* fat estimates to a small degree, since the time-dependent phase term is small. The main culprit of poor *ff* estimation is T_2* line-broadening, which suggests that a simultaneous *ff* and T_2* estimation is best.

The extended slow diffusion model was not used to fit the time course since it would be difficult to decouple the many changing parameters. However, it did inform us to include the θ_τ term and to steer clear of fitting near the SE peak. We used an adapted Dixon signal model to fit the decay of simulated data. While we were successful in fitting the complex data, we wanted to include optimization bounds which required fitting real and imaginary components separately. Including the θ_τ term and adding T_2* decay to fat yielded a more comprehensive description, even though they increased the number of fit parameters.

We initially considered ideal data without noise, but then extended our analysis since *in vitro* and *in vivo* data will have lower tSNR. T_2* estimates were very affected by noise until tSNR = 20 after which they plateaued. Noise performance is a factor to consider as we move towards real data from SPIO-labelled cells. However, we must continue to discriminate between temporal and and spatial (image) SNR when analyzing *in vitro* and *in vivo* samples.

Simulating the effect of unintended B_o inhomogeneity was beyond the scope of this thesis, but is another consideration for translating these techniques *in vitro* or *in vivo*. As seen in Chapter 5, we will add the ϕ(t) term that arises from B_o inhomogeneity for acquired data. This will make the fitting model more robust to inevitable data imperfections. The adjustment should prepare the model to fit experimental data, starting with *in vitro* phantoms.

Chapter 5

In vitro Data

While the ultimate goal is to translate the curve fitting approach *in vivo*, that is quite a large leap in complexity from our ideal simulations. *In vitro* work offers a suitable framework to analyze real (non-simulated) data with greater control than animal studies. The aim of this experiment is to investigate the fit performance for known data acquired with the TurboSPI sequence, in the presence of B_o inhomogeneity and noise. The known data consists of phantoms with equal concentrations of labelled cells, but varying fat fractions.

This *in vitro* work serves as a "stepping stone" to future *in vivo* studies that have greater data complexity and even more factors to consider.

5.1 Materials and Methods

Solutions of SPIO-labelled cells and peanut oil were made in 5 mm NMR tubes and held in a "shotgun" case for imaging. The tubes were submerged in a water bath that was doped with $MnCl_2$ (160 $\times 10^{-6}$ M), a paramagnetic contrast agent.

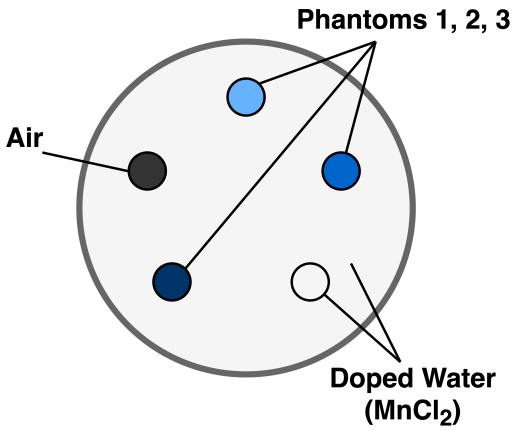

Figure 5.1: A schematic of the "shotgun" phantom case that was used to image multiple NMR tubes at once. Two reference tubes were included with air/background and $MnCl_2$ doped water

5.1.1 Sample Preparation

Nine samples were prepared with varying fat content according to Table 5.1. CD8+ cells were isolated, cultured, and loaded with SPIO using the SOP from Chapter 3 (Section A.2), however APCs were omitted to create a more homogenous mixture. Labelled cells were suspended in a polyacrylamide gel as per the following recipe.

Added in order of appearance:

- peanut oil (varying amounts - $V_{oil} + V_{H_2O} = 475$ mL)
- distilled water (varying amounts - $V_{oil} + V_{H_2O} = 475$ mL)
- 10% sodium dodecyl sulfate (SDS) 50 μL
- 40% acrylamide 250 μL
- hydroxyethyl piperazineethanesulfonic acid (HEPES) 1M 250 μL
- 10% ammonium persulfate (APS) 10 μL
- SPIO labelled cells (2×10^6)
- tetramethylethylenediamine (TEMED) (2 μL)

The surfactant (SDS) in the gel recipe enabled the oil to water mixing and we found that the polyacrylamide gel resulted in stable solutions without separation, contrary to agar which was also tested. Solutions were prepared one-by-one by first mixing in an Eppendorf tube and quickly transferring to the NMR tube. The samples included two "no cell" (NC) controls and one 0 % fat control.

The gelled suspensions were stored a refrigerator between imaging sessions, but they were stable at room temperature and did not separate during acquisition.

Table 5.1: SPIO-labelled cell and oil phantoms. A,B,C refer to sets of NMR tubes imaged together in the "shotgun" holder. A.3 through C.3 had a constant concentration of 2×10^6 cells in 1.035 mL. A.1 and A.2 were no cell (NC) controls.

	A.1	A.2	A.3	B.1	B.2	B.3	C.1	C.2	C.3
Fat %	20 NC	40 NC	20	40	30	15	10	5	0

5.1.2 Imaging

The samples were imaged in sets of three (Phantoms A, B, C) using the 2D TurboSPI sequence (Table 5.2). Since the phantoms are simple homogenous tubes the 2D data was sufficient and faster to acquire.

Table 5.2: 2D Large FOV TurboSPI Pulse Sequence Parameters

TR (ms)	TE (ms)	ETL	ESP	Matrix	FOV (mm^3)	Accel.	Time (min)
250	10	8	10	128×128	50×50	none	8:37

An ancillary objective of the *in vitro* work was to determine the efficacy of fat saturation and how it affects Dixon estimations. Therefore, the above sequence was run twice for each phantom: with and without the fat saturation pulse that is used *in vivo* (a low power version of the 90° sinc RF pulse used for initial excitation).

5.1.3 Analysis

The data were analyzed in *Relax!* as in Chapter 3. Basic Fourier reconstruction was used in lieu of the CS reconstruction since the 2D data acquisition was not accelerated by undersampling. *Relax!* was modified to include novel fat fraction estimation and R_2* mapping techniques.

Two-Point Dixon

First we tested the two-point Dixon technique as a proof-of-concept and to compare the results to *in silico* findings. In this case, the term two-point is a misnomer in that we actually used an average for each *in phase* (t = TE) and *out of phase* (t = TE + 1.1 ms) "point". These average *in phase* and *out of phase* points include two measurements prior to the time-point of interest and two after with $\Delta t = 10$ μs. While these would be quite difficult for most Dixon acquisition schemes, the high temporal resolution of TurboSPI makes it feasible.

Curve Fitting

The clear advantage of the curve fitting approach is that it can provide simultaneous estimates of fat fraction and R_2*.

While we tested multiple parameterizations of the model, most of our investigation focused on the signal equation that was developed in Chapter 4 (Equation 4.19). The main *in vitro* modification was that we considered B_o inhomogeneity. This was done through the inclusion of the ϕ term described earlier. Therefore, the *in vitro* signal equation becomes:

$$Re = [We^{-\Delta t/T_{2W}*}\cos(\theta_w + \theta_\tau \Delta t + \phi\Delta t) + Fe^{-\Delta t/T_{2F}*}\cos(\theta_f + \Delta\omega_{WF}\Delta t + \phi\Delta t)] \tag{5.1}$$

$$Im = [We^{-\Delta t/T_{2W}*}\sin(\theta_w + \theta_\tau \Delta t + \phi\Delta t) + Fe^{-\Delta t/T_{2F}*}\sin(\theta_f + \Delta\omega_{WF}\Delta t + \phi\Delta t)]$$

Again, the equation has been split into real and imaginary components to accommodate the need for optimization boundaries. To reduce the number of parameters, we define θ_{wt} and θ_{ft} to describe the time dependent phase terms since separating these features is not a priority.

$$\theta_{wt} = \theta_\tau + \phi \tag{5.2}$$
$$\theta_{ft} = \alpha + \phi$$

When fitting, θ_τ and α are used for the initial guesses and allowed to vary by ϕ.

5.2 Results and Discussion

5.2.1 *In Vitro* Signal Time Courses

Before estimating fat fractions or R_2*, we began by investigating the shape of the signal time courses for each tube. This allowed us to review the efficacy of fat saturation, specifically how it well it removed the signal modulation.

Example data are plotted for each phantom in Figures 5.2, 5.3, and 5.4. Note that the y-axis scale is not constant since the fat signal intensity is high and the maximum amplitude varies drastically with fat content. Each plot shows a time course from data that were acquired both with and without the fat saturation pulse.

Immediately we note that the tubes without any labelled cells (and therefore, without any SPIO effect) have higher relative amplitude on the side peaks (i.e. TE $\pm \approx 2.2$ ms), whereas those with labelled cells fall off faster due to T_2* dephasing. This agrees with theory and the simulated data.

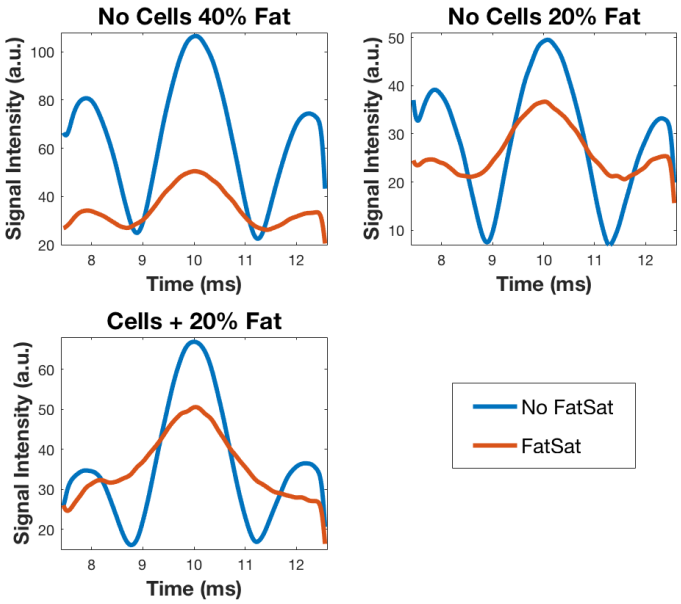

Figure 5.2: Signal time course data for Phantom A that were acquired with (orange) and without (blue) a fat saturation pulse. Phantom A has NMR tubes with 40% fat (no cells) (top left), 20% fat (no cells) (top right), and 20% fat (bottom left).

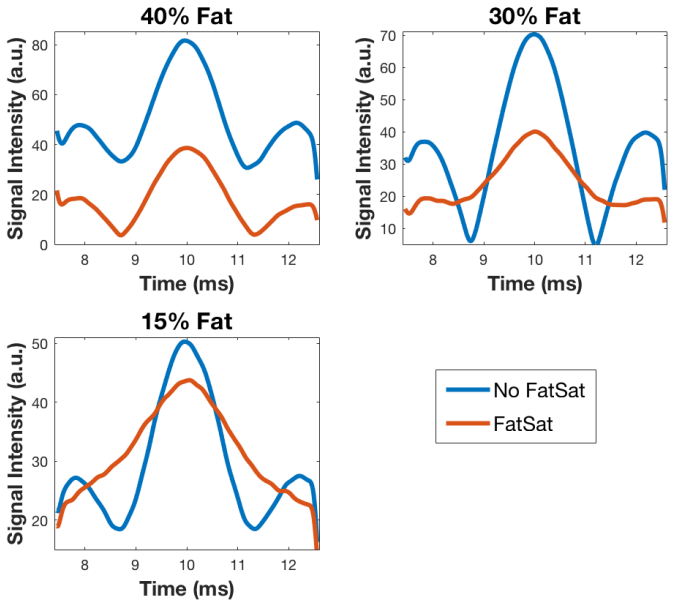

Figure 5.3: Signal time course data for Phantom B that were acquired with (orange) and without (blue) a fat saturation pulse. Phantom B has NMR tubes with 40% fat (top left), 30% fat (top right), and 15% fat (bottom left), all with cells.

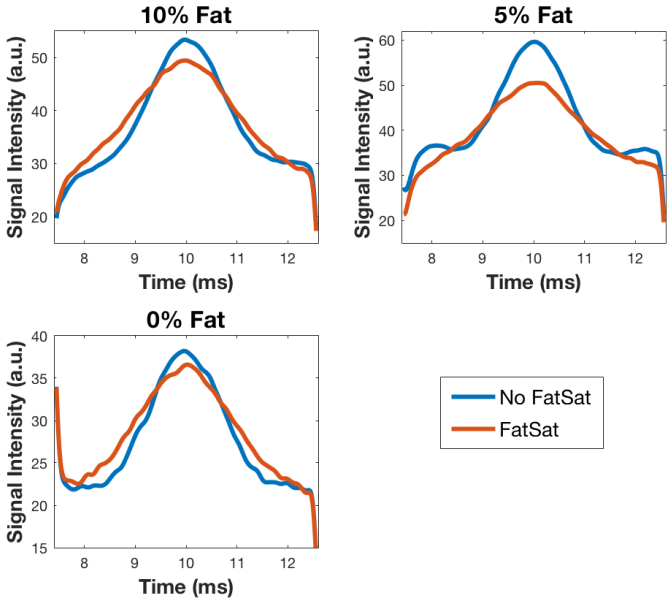

Figure 5.4: Signal time course data for Phantom C that were acquired with (orange) and without (blue) a fat saturation pulse. Phantom C has NMR tubes with 10% fat (top left), 5% fat (top right), and 0% fat (bottom left), all with cells.

These data also illustrate how difficult it would be to perform a signal subtraction similar as was done for the *in silico* data (Section 4.2). Not only because it may be difficult to determine an accurate fat fraction, but also because subtracting an appropriate fat signal with matched amplitude is not feasible. This confirms the suspicion that we we require a more elegant correction for real data.

The fat saturation pulse appears to be effective at removing the modulation from the signal time course up to 20% fat. For higher fat fractions (30% and 40%, slightly 20%) and the "no cell" tubes, the amplitude of the modulation is dampened, but the effect is still present. The amplitude of the damped signal is still within the range the water peak (signal intensity = 35 to 50) and therefore will still have deleterious effects when fitting. It is also worrisome that when the modulation is effectively removed, the amplitude at TE remains larger than that of the no-fat control. As well, there could be erroneous fits when the modulation is only partially removed, even if no SPIO labelled cells are present (e.g. 20% no cells). Lastly, the no-fat control in Figure 5.4 shows that fat saturation slightly dampens the signal from water as well.

These data show that current fat saturation techniques are ineffective and inconsistent. Line-broadening restricts the spectrally selective suppression pulses that we

can use (for fear of hitting the broadened water peak). Other fat suppression techniques do exist, such as short T_1 inversion recovery (STIR) which utilizes the short T_1 of fat [131]. While STIR may be an interesting avenue for further investigation, it is beyond the scope of this thesis which focuses on CHESS and Dixon techniques.

5.2.2 Initial R_2* Mapping Challenges

Next, we illustrate the R_2* estimation errors for the current technique. Figures 5.5, 5.6, and 5.7 display the R_2* maps for each Phantom with and without fat saturation. Regions of interest were drawn for each NMR tube in Matlab and the average R_2* results are listed in Table 5.3.

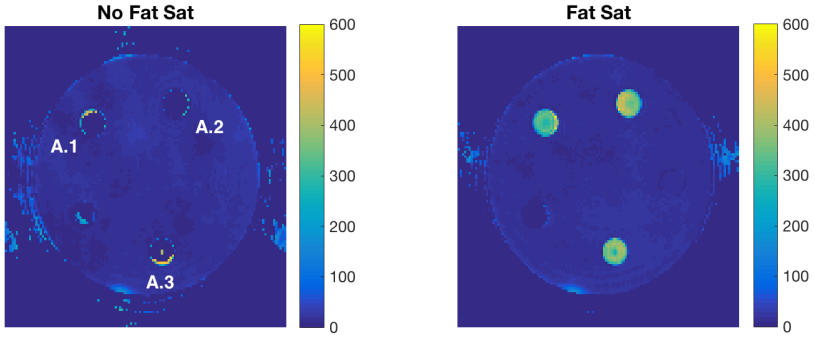

Figure 5.5: Phantom A R_2* maps (s^{-1}) for data acquired without (left) and with (right) a fat saturation pulse. R_2* maps were calculated using *Relax!* with the "Elimination" technique. Tube labels (A.1, A.2, A.3) are shown on the left panel.

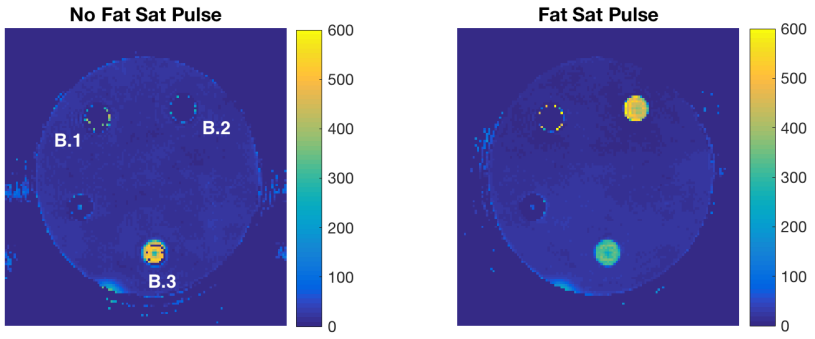

Figure 5.6: Phantom B R_2* maps (s^{-1}) for data acquired without (left) and with (right) a fat saturation pulse. R_2* maps were calculated using *Relax!* with the "Elimination" technique. Tube labels (B.1, B.2, B.3) are shown on the left panel.

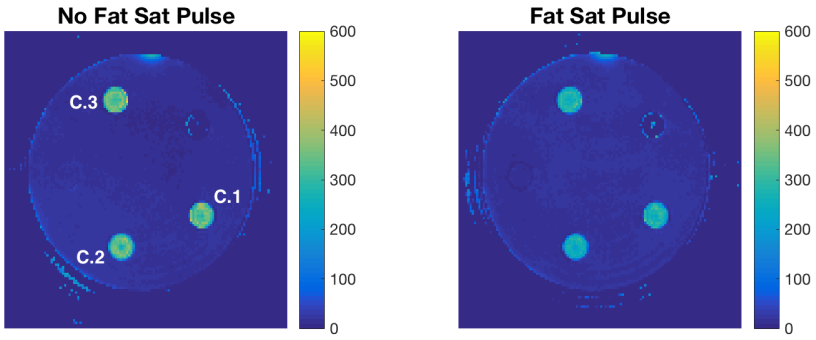

Figure 5.7: Phantom C R_2* maps (s^{-1}) for data acquired without (left) and with (right) a fat saturation pulse. R_2* maps were calculated using *Relax!* with the "Elimination" technique. Tube labels (C.1, C.2, C.3) are shown on the left panel.

Table 5.3: Table of mean and standard deviation (SD) of R_2* values for the phantoms, organized by fat content. "FS" refers to data acquired with a fat sat pulse.

	A.1	A.2	B.1	B.2	A.3	B.3	C.1	C.2	C.3
Known Fat %	20 NC	40 NC	40	30	20	15	10	5	0
Mean R_2* (s^{-1})	34	3	21	3	74	338	335	329	334
SD R_2* (s^{-1})	116	29	94	27	169	212	34	32	31
Mean R_2* (s^{-1}) FS	334	387	14	458	362	321	275	247	273
SD R_2* (s^{-1}) FS	31	41	86	30	33	29	25	24	26

These R_2* results corroborate the earlier concerns regarding the signal time course behaviour. There are numerous issues to address for both data sets with and without fat saturation.

Data without *fat saturation*

In the absence of a fat saturation pulse, data with a large fat content tend towards $R_2 = 0\ s^{-1}$ when they are mapped using the most recent "Elimination" technique in *Relax!*. This is the appropriate and intended result for tubes A.1 and A.2 which have no SPIO labelled cells. However, the R_2* in tubes B.1, B.2, and A.3 also tend towards zero. Ideally, these tubes would have an R_2* value equal to that of the no-fat control (tube C.3) to reflect their equal concentrations of labelled cells. Unfortunately, the

fat modulation overwhelms the R_2* effect and these voxels are eliminated. C.1, C.2, C.3 are consistent within their standard deviation sub-groupings, suggesting that fat content lower than 10% have negligible effects on R_2* estimation. However, we note that Tube C.1 (10%) did not mix as well homogeneously as the other tubes and thus we are less confident with that specific result.

Technically, the R_2* for tube B.3 (15%) is also consistent with the control, however the standard deviation is quite high (more than 6x that of C.1,C.2, and C.3). This is illustrated in the left panel of Figure 5.6 which shows that some voxels in the ROI go to zero, but many have a high R_2* value (500 s^{-1}), likely due to mistakenly fitting the fat modulation.

Data with *fat saturation*

The data acquired with the fat saturation pulse have a unique set of issues. Again, tubes C.1 and C.2 agree with the no-fat control, however fat suppression decreased the R_2* value considerably, even for the no-fat control. This indicates that the fat suppression pulse hits the water peak as well as the fat peak (in the frequency spectrum) and consequently reduces the R_2* decay. The reduced R_2* values are worrisome, but we notice that the reduction is, at least, consistent for tubes C.1, C.2, and C.3. However, since the cell quantification is performed using an R_2* calibration, future work could consider performing the calibration with fat saturation to improve quantification accuracy.

Results for the tubes with higher fat fractions (Phantoms A and B) are even more concerning. Deceptive errors arise when the modulation is only partially removed from the time course. This unfortunate effect is even seen when there are no SPIO labelled cells present (tubes A.1, A.2). In fact, the only tube that is effectively eliminated from the map is B.1, a tube with SPIO labelled cells and 40% fat. This is unsurprising if we consider the corresponding signal time course plot in Figure 5.3 (top left) which shows that the integrity of the *fat sat* fat modulation is maintained for B.1. While it is unfortunate that the fit did not uncover a correct R_2* for tube B.1, the deceptively high R_2* estimates for tubes A.1, A.2, B.2, and B.3 could lead to greater errors.

These results demonstrate that current R_2* mapping techniques are inadequate

when fat content rises above 10%, whether a fat saturation pulse is applied or not.

5.2.3 Two-Point Dixon: *In Vitro*

The simple two-point method serves as a proof-of-concept to show that real TurboSPI data are amenable to the Dixon techniques. Figures 5.8, 5.9, and 5.10 give the fat fraction (*ff*) maps for Phantoms A, B, and C and Table 5.4 lists the mean *ff* for each tube. Erroneous voxels in the background can be removed by thresholding the signal intensity of the TurboSPI data, but are helpful for outlining the phantom.

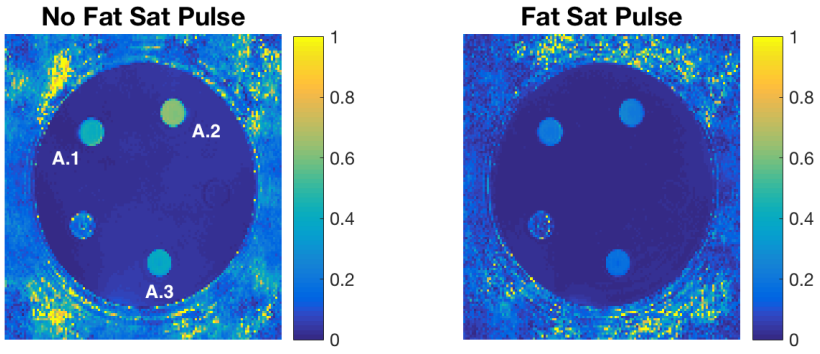

Figure 5.8: Phantom A *ff* maps for data acquired without (left) and with (right) a fat saturation pulse. The *ff* maps were calculated using *Relax!* with the two-point Dixon method. Tube labels (A.1, A.2, A.3) are shown on the left panel.

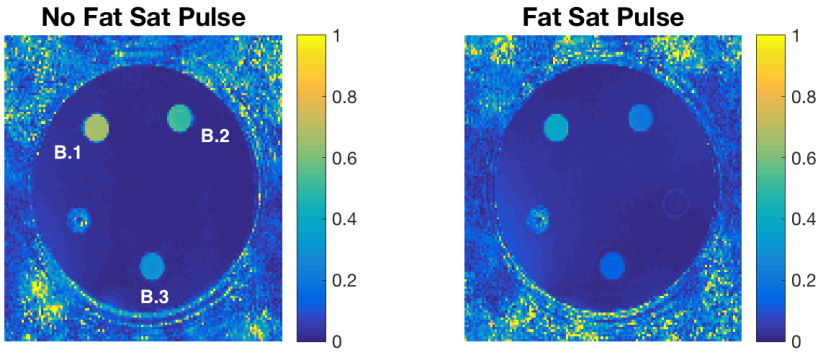

Figure 5.9: Phantom B *ff* maps for data acquired without (left) and with (right) a fat saturation pulse. The *ff* maps were calculated using *Relax!* with the two-point Dixon method. Tube labels (B.1, B.2, B.3) are shown on the left panel.

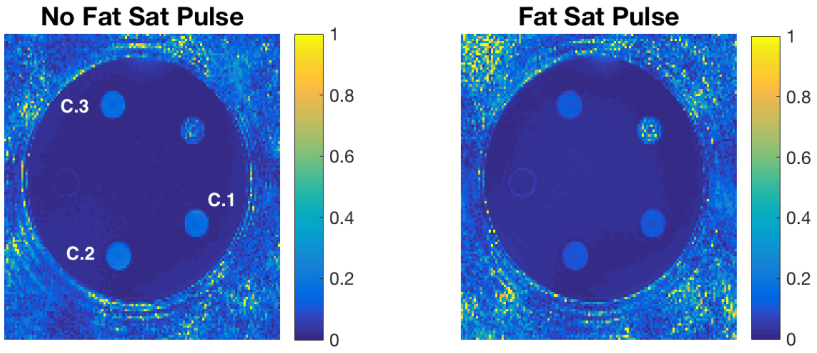

Figure 5.10: Phantom C *ff* maps for data acquired without (left) and with (right) a fat saturation pulse. The *ff* maps were calculated using *Relax!* with the two-point Dixon method. Tube labels (C.1, C.2, C.3) are shown on the left panel.

Table 5.4: Table of mean and standard deviation (SD) of *ff* values for the phantoms, organized by fat content. "FS" refers to data acquired with a fat sat pulse.

	A.1	A.2	B.1	B.2	A. 3	B.3	C.1	C.2	C.3
Known Fat %	20 NC	40 NC	40	30	20	15	10	5	0
Mean Fat %	41	61	66	50	39	29	16	18	16
SD Fat %	2	2	1	2	2	2	3	2	1
Mean Fat % FS	19	22	38	22	17	14	11	10	11
SD Fat % FS	2	2	3	4	2	2	3	3	1

Immediately, we notice that the *ff* data are more consistent (with smaller relative standard deviations) than the R_2* fits presented earlier, suggesting that two-point Dixon is precise, even if it is not accurate. *ff* estimates from data with fat saturation are appropriately lower than the corresponding data without saturation.

As with the *in silico* data, the two-point Dixon method consistently overestimates fat content for the *in vitro* samples without fat saturation. In contrast to the *in silico* work, overestimates occur even for tubes without SPIO labelled cells, albeit less so than for tubes containing the cells.

The fat fraction for the "no cell" tubes (A.1, A.2) are equal within their standard deviations (19 ± 2 versus. 22 ± 2) for the fat saturated data, but very different for the data without fat saturation. This illustrates how the fat saturation pulse is not

fully effective and suggests that 20% could be a common residual signal (after fat saturation), but this is impossible to determine without more "no cell" data.

The no-fat control has non-zero *ff* in both data sets. This suggests that some of the overestimation could arise from the labelled cells, similar to the *in silico* work which presents a no-fat Δff (estimated *ff* - known *ff*) of the same magnitude. However, this may be overshadowed by *ff* inflation from the fat itself since the Δff increased as a function of known fat content, in contrast to the *in silico* work.

At this point, we must note a slight design difference between the two-point Dixon *in silico* and two-point Dixon *in vitro* studies. Since the *in silico* study varied the signal according to S (1-*ff*)S_w + *ff*S_f (with ff = $0 \rightarrow 1$), where the S_w comes from the Monte Carlo simulation and S_f is inserted after. Therefore, when *ff* was increased, there was less relative S_w and therefore, less relative estimation error from SPIO. This did not effect the R_2* calculations since the effect is simulated and fit uniquely for the two species. For the *in vitro* study, the water content varies similarly (Total = (1-*ff*)W + *ff*F), but the cells are added separately and they are not linked specifically to the water signal. Therefore, in these data, we should not expect the offset Δff to decrease with increased fat content.

It is still interesting to plot the results as estimated *ff* versus known *ff* (Figure 5.11).

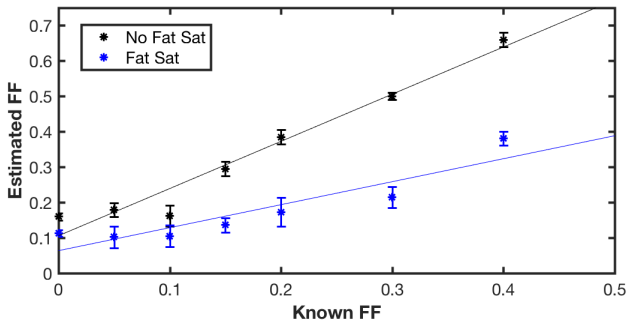

Figure 5.11: Estimated *ff* versus Known *ff* for the data given in Table 5.4 (Black: no fat saturation, Blue: fat sat). Linear fits are performed for each data set. R^2 goodness of fit values are 0.96 and 0.84 for the black and blue lines, respectively.

The "no fat sat" *ff* are linear, with an $R^2 = 0.96$. Tube C.1 (10%fat) is much lower than expected. As mentioned earlier, Tube C.1 had poor oil-water mixing and the

mixture was less homogenous than the other tubes, perhaps explaining this reduced estimate.

The *fat sat ff* are less consistently linear ($R^2 = 0.85$), which could be because the fat saturation pulse appears to be more effective for lower fat fractions ($> 20\%$).

Table 5.5 shows a brief attempt to recover corrected *ff* values using the linear fit of *no fat sat* data, as was done with *in silico* data in Section 4.2. Again, this is clearly very dependent on a fit line which will never be known *in vivo* and as such, is shown for example only.

Table 5.5: Rough *ff* estimates after the *no fat sat ff* data were scaled using the calibration with known values (Figure 5.11).

	A.1	A.2	B.1	B.2	A. 3	B.3	C.1	C.2	C.3
Known Fat %	20 NC	40 NC	40	30	20	15	10	5	0
"Corrected" Fat %	23	38	42	31	20	14	3	5	3

Even though two-point Dixon gives inaccurate (but precise) measures of fat content, these data indicate that TurboSPI data respond reasonably well to Dixon manipulations. As predicted by the *in silico* work, we should move forward to a more comprehensive Dixon model.

5.2.4 Simulataneous R_2* and *ff* Estimation

We use the decay model described in Section 5.1.3 for simultaneous estimation of multiple parameters, most relevantly T_2* and *ff*.

All data are fit twice to investigate different approaches for mapping T_2* decay in the presence of fat:

1. Separating the effects (as in Equation 5.1) to map a unique T_{2W}* on the water species.

2. Fitting a common T_2* to map an average decay constant for the two species.

Table 5.6 lists the initial parameter guesses and lower/upper bounds for the optimization. These are common for the two approaches, excluding those for T_2* which are defined separately.

Table 5.6: Initial guesses and bounds used in the optimization. $T_{2W}*$/ $T_{2F}*$ and T_2* are used for Methods 1 and 2 above.

	W	F	$T_{2W}*$	$T_{2F}*$	T_2*	θ_w	θ_f	θ_{wt}	θ_{ft}
Initial Guess	0.5	0.5	5	20	5	0	0	0	$\Delta\omega_{WF}$
Lower Bound	0	0	1	2	1	-π	-π	-2π	$\Delta\omega_{WF}$ - π
Upper Bound	1	1	30	50	50	π	π	2π	$\Delta\omega_{WF}$ + π

To conform to previous *in vitro* analyses we convert T_2* to R_2* and will continue with this convention for the duration of this section.

Method 1: Fitting unique $R_{2w}*$

Figures 5.12, 5.13, and 5.14 show the R_2* and *ff* maps for Phantoms A, B, C computed for the data acquired with and without a fat saturation pulse.

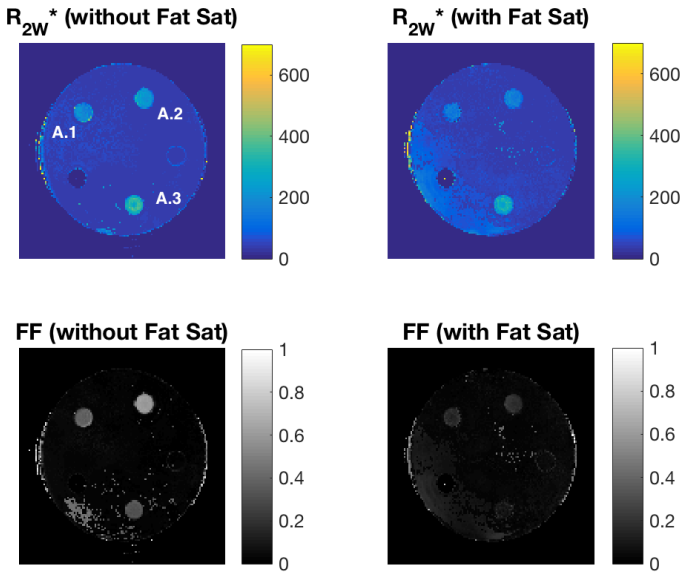

Figure 5.12: Phantom A Method 1: $R_{2W}*$ (s^{-1}) (top) and *ff* (bottom) maps for data acquired without (left) and with (right) *fat sat.* Tube labels (A.1, A.2, A.3) are top left.

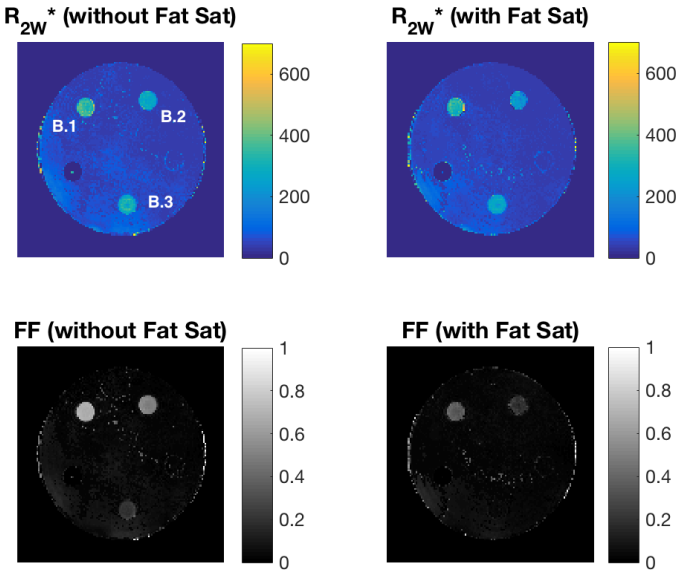

Figure 5.13: Phantom B Method 1: R_{2W}* (s^{-1}) (top) and *ff* (bottom) maps for data acquired without (left) and with (right) *fat sat*. Tube labels (B.1, B.2, B.3) are top left.

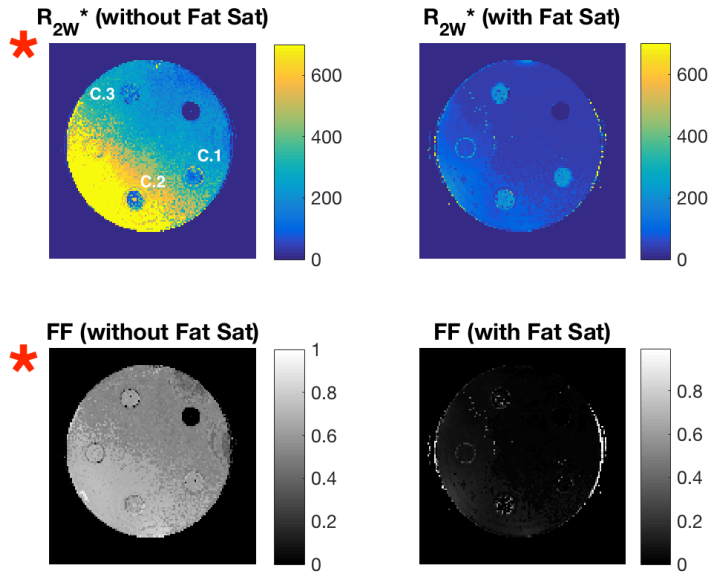

Figure 5.14: Phantom C Method 1: R_{2W}* (s^{-1}) (top) and *ff* (bottom) maps for data acquired without (left) and with (right) *fat sat*. Tube labels (C.1, C.2, C.3) are top left. The red asterisks denote unreasonable fits due to shimming errors in acquisition.

Tables 5.7 and 5.8 compare mean values for R_2* and *ff* respectively, but we describe qualitative observations of the R_2* maps first. The maps for Phantom A show that, for the first time, tubes with only fat (no labelled cells) present with significantly lower R_2* than tubes with labelled cells for data with and without *fat sat*. Ideally, these "no cell" tubes would be lower, however these results are an improvement over the mono-exponential method. The R_2* maps for Phantom B also show improvement in that the R_2* values for the three tubes are much more similar (to each other) than the previous method. Fitting Phantom C (with *fat sat*) using Method 1 performed similarly to the mono-exponential method, which is appropriate since these tubes contained little to no fat. Fitting Phantom C *no-fat-sat* failed dramatically due to large phase errors (see Figure B.1), likely to shim issues during acquisition.

Despite improvements, we note a caveat in that both the R_2* and *ff* maps are less precise than before, with more spurious fits in the water bath. However, these are still lower the baseline R_2* used for *in vivo* studies (≈ 120 s^{-1}).

Method 2: Fitting average R_2*

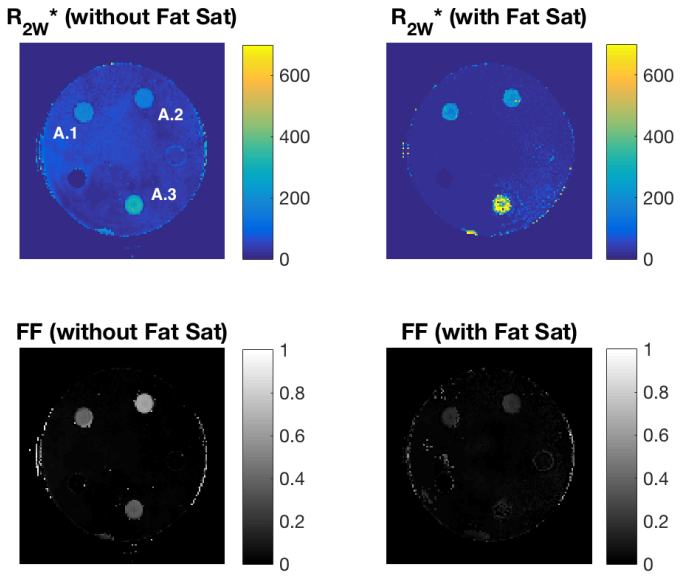

Figure 5.15: Phantom A Method 2: R_2* (s^{-1}) (top) and *ff* (bottom) maps for data acquired without (left) and with (right) *fat sat*. Tube labels (A.1, A.2, A.3) are top left.

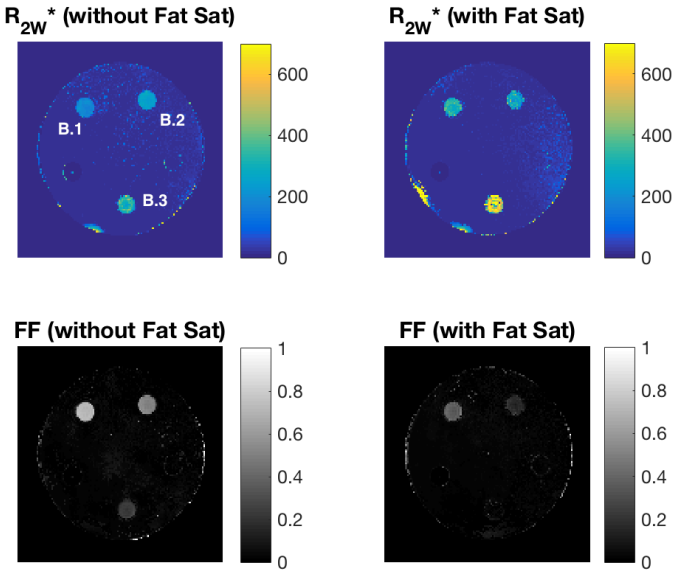

Figure 5.16: Phantom B Method 2: R_2* (s^{-1}) (top) and *ff* (bottom) maps for data acquired without (left) and with (right) *fat sat*. Tube labels (B.1, B.2, B.3) are top left.

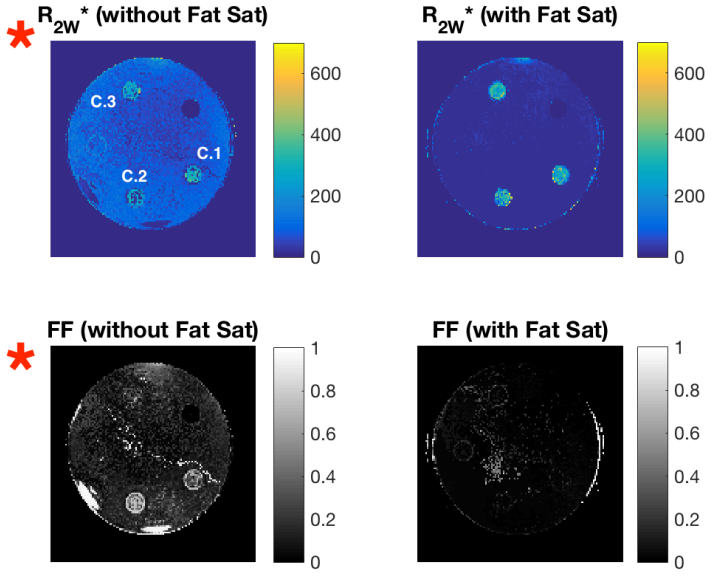

Figure 5.17: Phantom C Method 2: R_2* (s^{-1}) (top) and *ff* (bottom) maps for data acquired without (left) and with (right) *fat sat*. Tube labels (C.1, C.2, C.3) are top left. The red asterisks denote unreasonable fits due to shimming errors in acquisition.

Again, we begin with a qualitative discussion of the R_2* maps before showing the mean values from the ROI analysis. The Phantom A R_2* estimates have improved similarly to Method 1 for the data without fat saturation: tubes with no cells have appropriately lower R_2* than tubes with cells. While, this trend continues for the data with fat saturation we notice that tube A.3 (20% fat with cells) presents inflated R_2* estimates. Furthermore, the R_2* values for this data set are much noisier and less precise, as is seen in Table 5.7. The data for Phantom B show that R_2* apparently increased with decreased fat content, an undesirable effect since the tubes have equal concentrations of SPIO labelled cells. Again, the *no fat sat* data for Phantom C are unusable, but the R_2* values for the data with fat saturation are appropriately similar for the three tubes.

R_2* Comparisons

The qualitative discussion above suggests that Method 1 is superior to Method 2, especially in the case of data acquired with fat saturation. This is verified by Table 5.7 which gives the results from an ROI analysis of each tube.

Table 5.7: Estimated R_2* by Methods 1 and 2 for each data set. Method 1 calculates the unique R_{2W}* decay on the water species and Method 2 calculates the average R_2* for the mixture. Phantom C *no fat sat* data are excluded due to experimental errors that led to unrealistic fits.

	A.1	A.2	B.1	B.2	A. 3	B.3	C.1	C.2	C.3
Known Fat%	20 NC	40 NC	40	30	20	15	10	5	0
Method 1 Mean R_2* (s^{-1})	186	222	345	270	326	299	—	—	—
Method 1 SD R_2* (s^{-1})	27	35	52	33	38	38	—	—	—
Method 1 Mean R_2* (s^{-1}) FS	146	163	317	220	278	254	206	192	184
Method 1 SD R_2* (s^{-1}) FS	27	23	49	40	42	27	37	74	56
Method 2 Mean R_2* (s^{-1})	175	155	191	249	300	336	—	—	—
Method 2 SD R_2* (s^{-1})	13	8	15	17	27	54	—	—	—
Method 2 Mean R_2* (s^{-1}) FS	199	227	313	266	530	557	269	263	296
Method 2 SD R_2* (s^{-1}) FS	50	69	37	66	239	193	85	101	76

First, we notice that the *fat sat* R_2* estimates provided by Method 2 have much

larger standard deviation than those from Method 1, which indicates that this technique does not have a stable response to fat saturation. As well, both the *fat sat* and *no fat sat* estimates vary significantly with fat content, a feature that we are trying to avoid. Since Method 2 attempts to fit an average R_2* for the mixture, these variations could reflect varying R_2* contributions from the different species. In contrast, Method 1 exhibits superior inter-tube and intra-tube consistency. That is, the R_2* estimates are more similar when they should be similar (Tubes A.3 - C.3) and, in general, they have lower standard deviations for the *fat sat* data.

We have established that Method 1 surpasses Method 2 with respect to accurate R_2* fitting in the presence of fat. Next, we want to ascertain if, as suggested in the qualitative discussion above, Method 1 improves upon the previous method (basic R_2* fit with *fat elimination*). Figure 5.18 shows R_2* estimates by *ff* for Methods 1, 2, and the original technique. While the old technique is most stable for low fat content, the fitting begins to fail at 15% fat for the *no fat sat* data and 20-30% for the *fat sat* data. Method 1 estimates are most stable in general, indicating that it may be reasonable to fit R_2* with this more comprehensive signal model.

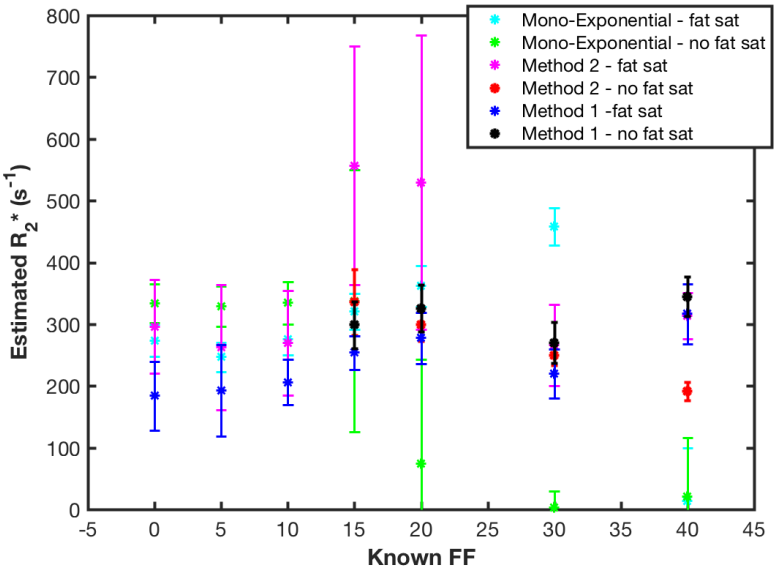

Figure 5.18: Estimated R_2* versus known mixture *ff* for *fat sat* and *no fat sat* data with fitting by Methods 1, 2, and the "old technique"

We would be remiss not to mention certain drawbacks. The dramatic failures

in fitting the *no fat sat* data from Tube C are quite alarming. Figure 5.4 does not reveal any suspicious behaviour in the signal time course and R_2* estimates from the previous fitting technique are sound. This is because the failure arises from phase errors (Figure B.1), probably from a poor shim. Since the time course shows signal magnitude versus time and the previous technique fits the magnitude decay, these data are less likely to reflect phase error. Recall that the signal model in Method one *does* have a term to describe B_o inhomogeneity, but this may not be able to handle large changes from an ineffective shim.

Without the *no fat sat* data for Tube C we cannot compare how Method 1 performs with fat saturation versus without fat saturation. The data behave similarly from 15% fat to 40% fat, but it would be valuable to compare the data for low fat content. Another future step involves performing an *in vitro* study for different cell concentrations with and without added fat.

FF Comparisons

The main goal of including a *ff* parameter in the fit is to improve R_2* estimates for voxels with fat. We are not necessarily interested in fat estimates themselves since they do not have a direct purpose in cell tracking studies. Nonetheless, it is interesting to investigate the fit performance with respect to *ff*. These data are reported in Table 5.8 and Figure 5.19.

Table 5.8: Estimated fat content by Methods 1 and 2 for each data set. Phantom C *no fat sat* data are excluded due to experimental errors that led to unrealistic fits.

	A.1	A.2	B.1	B.2	A. 3	B.3	C.1	C.2	C.3
Known Fat%	20 NC	40 NC	40	30	20	15	10	5	0
Method 1 Fat %	39	60	68	50	33	21	—	—	—
Method 1 SD Fat %	4	2	2	3	2	3	—	—	—
Method 1 Fat % FS	17	19	36	21	10	4	4	10	8
Method 1 SD Fat % FS	3	2	4	4	3	2	8	15	12
Method 2 Fat %	39	63	72	52	35	23	—	—	—
Method 2 SD Fat %	4	2	2	3	2	2	—	—	—
Method 2 Fat % FS	17	18	38	17	8	4	4	4	6
Method 2 SD Fat % FS	4	2	4	3	6	6	4	5	8

Methods 1 and 2 perform similarly for *ff* $\geq$15% for data with and without fat saturation. As expected, the estimated fat fractions are lower for the data with *fat sat* and these data also show increased intra-tube variability. Both methods exhibit a loss of linearity and large intra-tube variability for tubes with a *ff*<15. As suggested earlier by the two-point Dixon analysis (Figure 5.11) and the signal time plots (Figures 5.2, 5.3, and 5.4), the fat saturation pulse appears to be completely successful for these low *ff*.

Both methods have difficulty fitting an accurate *ff* when there is little to no fat content. The *in silico* noise performance plots (Figure 4.27) show *ff* overestimates with large variability for tSNR < 20, particularly for low (0 and 5%) *ff* data. This effect may explain poor fit performance for *in vitro* data with low *ff*. However, TurboSPI time course data are significantly denoised (as demonstrated in Ref. [158]) which markedly improves tSNR. As well, the overestimates are similar to those from simple two-point Dixon. These *ff* inaccuracies are not excessively worrisome since we are not specifically analyzing *ff* for *in vivo* cell tracking studies. However, it is an unexpected outcome that could be more fully characterized in a future study.

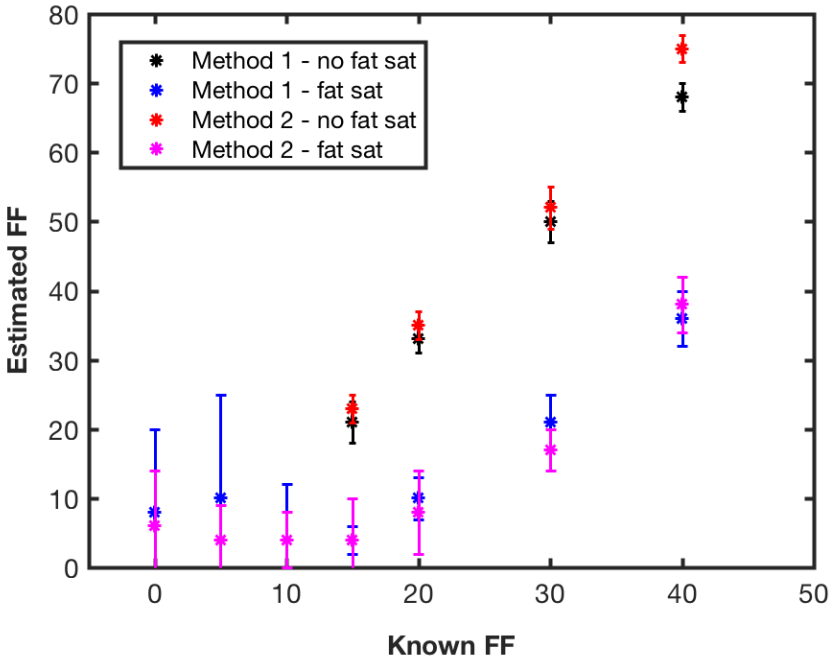

Figure 5.19: Estimated *ff* (expressed as a percentage) versus known mixture *ff* for *fat sat* and *no fat sat* data with fitting by Methods 1 and 2.

5.3 *In Vitro* Summary and Conclusions

We applied the methods developed *in silico* to *in vitro* data. This way, we could translate a curve fitting approach to real (acquired) data without the added complications associated with *in vivo* data. We tested tubes with equal concentrations of SPIO labelled cells, but varying concentrations of oil to reflect varying fat fractions.

First, we compared signal time course plots to illustrate the fat modulation for various *ff* and investigate the efficacy of the fat saturation pulse. Next, we computed R_2* maps using the former fitting technique to demonstrate challenges associated with these signal modulations. The mean R_2* estimates obtained using the former technique were consistent until 10% - 15% fat.

After the initial *in vitro* demonstration, we estimated the relevant parameters using a curve fitting approach for two different signal models. The first model fit unique R_2* decays for the water (R_{2W}*) and fat (R_{2F}*) species and reported the R_{2W}* for the quantitative map. The second model conformed to techniques found in the literature [134] [139] that suggest an average R_2* for the mixture. We found that the first model gave the most stable R_2* estimates for equal concentrations of SPIO labelled cells across all tested fat fractions (0-40%). These results suggest that, when fat is present, we could improve R_2* accuracy by using this more comprehensive signal model. These methods perform similarly to the previous technique in the absence of fat, although with slightly larger variability and lower estimates. Since the maximum signal magnitude is lower for the no-fat and low-fat data, low SNR could account for the diminished R_2*, as was seen *in silico*.

A caveat of this method is that we do not see $R_2 \rightarrow 0$ for the "no cell" tubes. Ideally, the R_2* would be very low for these tubes. This will present a challenge for applying the technique *in vivo*. On a positive note, these "no cell" R_2* values are now closer to the baseline R_2* for *in vivo* studies. However, they should be equal to or lower than baseline for this technique to reach its full potential of discriminating SPIO labelled cells from fat *in vivo*.

The *in vitro* study allowed us to test the proposed hybrid fit on data of intermediate complexity. Fitting a unique R_2* decay to the water species showed promise in removing fat contributions from R_2* maps. However, future investigations are required before we can confidently use this technique *in vivo*. First, characterizing

fit performance for various concentrations of SPIO labelled cells without any added fat. Next, reducing R_2^* in fat voxels even further such that it falls below *in vivo* baseline and, finally refining the fit to adapt to data with lower temporal SNR. To our knowledge this is the first instance of fitting unique R_{2W}^* and R_{2F}^* using the Dixon signal model. Future implementations may consider fitting an average R_2^* as long as separate base values (i.e. in the absence of SPIO) are included in the model for each species.

Chapter 6

Conclusion

6.1 Conclusions

This thesis consists of three interconnected studies: the first exposes a problem, the second investigates the problem *in silico* and proposes a solution, and the third applies the solution to more realistic data. The workflow is analogous to a *bedside to bench* approach in medical research, wherein a problem is identified in the clinic and investigated in the laboratory. Such an approach benefits from studying a highly specific and necessary problem. This is contrary to a *bench to bedside* workflow, in which a research question is hypothesized in the laboratory before translating it to a clinical setting.

In Chapter 3 we presented results from an *in vivo* study in which we compared immunotherapeutics (checkpoint inhibitor anti-PD-1, DPX-R9F vaccine, and a combination) using quantitative cell tracking by TurboSPI. This was the first large cohort, multiple treatment, *in vivo* study using TurboSPI (along with the more conventional bSSFP).

Unfortunately, we saw that signal modulations from off-resonance fat impeded our ability to perform accurate and specific R_2* mapping. These data demonstrated how fat can negatively affect the accuracy of cell quantification in *in vivo* studies. While fat is typically not directly in a region of interest (e.g. a tumour or a lymph node), these regions are often surrounded by a fat pad, which can confound analysis. Therefore, we cannot simply use anatomical context to ignore fat. As such, this chapter served to present a challenge: R_2* fitting in the presence of fat.

Chapter 4 began with a thorough investigation of the problem using *in silico* methods. We used Monte Carlo simulations and the extended slow diffusion model to generate signal time course data and added the off-resonance fat signal for different fat fractions. These data illustrated how the time course shape changes with varying amounts of added fat.

We studied different methods to estimate the fat fraction and correct for the corresponding signal oscillation. The most promising technique used a hybrid Dixon and R_2* signal model to fit the decay. This technique enabled simultaneous estimation of both fat content and R_{2W}*, the unique decay for the water species. Fat fraction estimates were accurate from 0% to 100% and R_{2W}* were stable across the same fractions, excluding poor performance at fat fraction extrema. By adding white Gaussian noise we found that the parameter estimates were stable for SNR > 20, but lower SNR resulted in fat overestimates and R_2* underestimates. Therefore, noise performance should be considered when fitting non-simulated data.

In the final chapter, we translated the new fitting approach to *in vitro* data. This approach gave us data acquired on the 3T magnet with the TurboSPI sequence, but with a larger degree of control than an *in vivo* study. Nine solutions of oil, water, and SPIO labelled cells were prepared in NMR tubes and scanned with three tubes per acquisition in a shotgun phantom holder.

The final results demonstrated that the simple mapping technique became inadequate when the fat fraction rose above 15-20% while the proposed technique provided more stable R_2* estimates for these larger fat fractions. We were successful in creating a technique that outperformed the simple model in the presence of fat. However, the hybrid technique appeared to underestimate R_2* when fat content was absent or low and continues to overestimate fat R_2*, although far less than the mono-exponential fit.

6.2 Remaining Limitations and Future Work

We have shown promising initial results for the *in vitro* samples, but more work needs to be done to improve performance and make this technique fully translatable to *in vivo* data. This includes a second *in vitro* study to characterize fit performance for various concentrations of SPIO to ascertain if the R_2* estimates vary appropriately, as they did in the *in silico* study.

While the R_2* estimates for "no cell" fat phantoms are approaching the *in vivo* baseline, preferably they would be at, or below, baseline. For this reason, the hybrid technique has not been formally tested on the *in vivo* data since "no cell" fat voxels will continue to contribute to the final R_2* map. One option is to increase the *in*

vivo baseline, however this would increase the detection threshold and thus reduce sensitivity. Therefore more work to should be done to further reduce R_2* estimates for "no cell" fat voxels.

During the *in silico* study we emulated the effect of low SNR to study noise performance. There are other factors that affect image quality, such as B_o inhomogeneity, that could also impair fit accuracy. This invites further work simulating these factors *in silico* to investigate fit performance.

Despite the challenges mentioned above, the goal is *in vivo* translation. Figure C.1 gives a preliminary *in vivo* demonstration of the hybrid technique and shows how it compares to earlier methods, but also highlights the current caveats. Earlier we noted that, when both SPIO labelled cells and fat are present, the hybrid Dixon-R_2* technique performed best for fat $> 15\%$ and the simple technique performed best for fat $< 15\%$. Ideally, we would like to improve the hybrid technique, but an adaptive approach may be acceptable in the interim. The adaptive technique would use the estimated fat fraction to indicate voxels with low fat fraction that should be re-fit with the simple technique. Fat fraction would dictate which fit model to use for each voxel in the map, thus exploiting the strengths of each technique. The hybrid technique will likely be most effective near the edges of tumours where immune cells that have poor infiltration may accumulate.

6.3 Final Summary

The principal objective of this work was to study the effect of fat modulations in TurboSPI and propose corrective methods. We addressed our goal by illustrating the problem *in vivo*, investigating the system *in silico* to develop a solution, and finally testing that solution on real data.

We were successful in developing a reliable model *in silico* that could estimate fat content and R_2* decay across various simulated conditions. Translation to physically acquired data was moderately successful. Using the proposed hybrid Dixon-R_2* technique, we obtained simultaneous estimates of fat fraction and R_2* for *in vitro* samples. When both SPIO labelled cells and fat were present, the hybrid technique performed better than the previous mono-exponential fit. There are challenges to address before *in vivo* translation is possible, specifically the fit performance when

only cells or *only fat* are present. We have, however, improved fitting for certain physical conditions. Therefore, this work is a step towards more comprehensive and robust R_2^* mapping, which will in turn give more accurate cell quantification.

Appendix A

Experimental Details: Chapter 3

A.1 Schedule for Pilot *In Vivo* Study

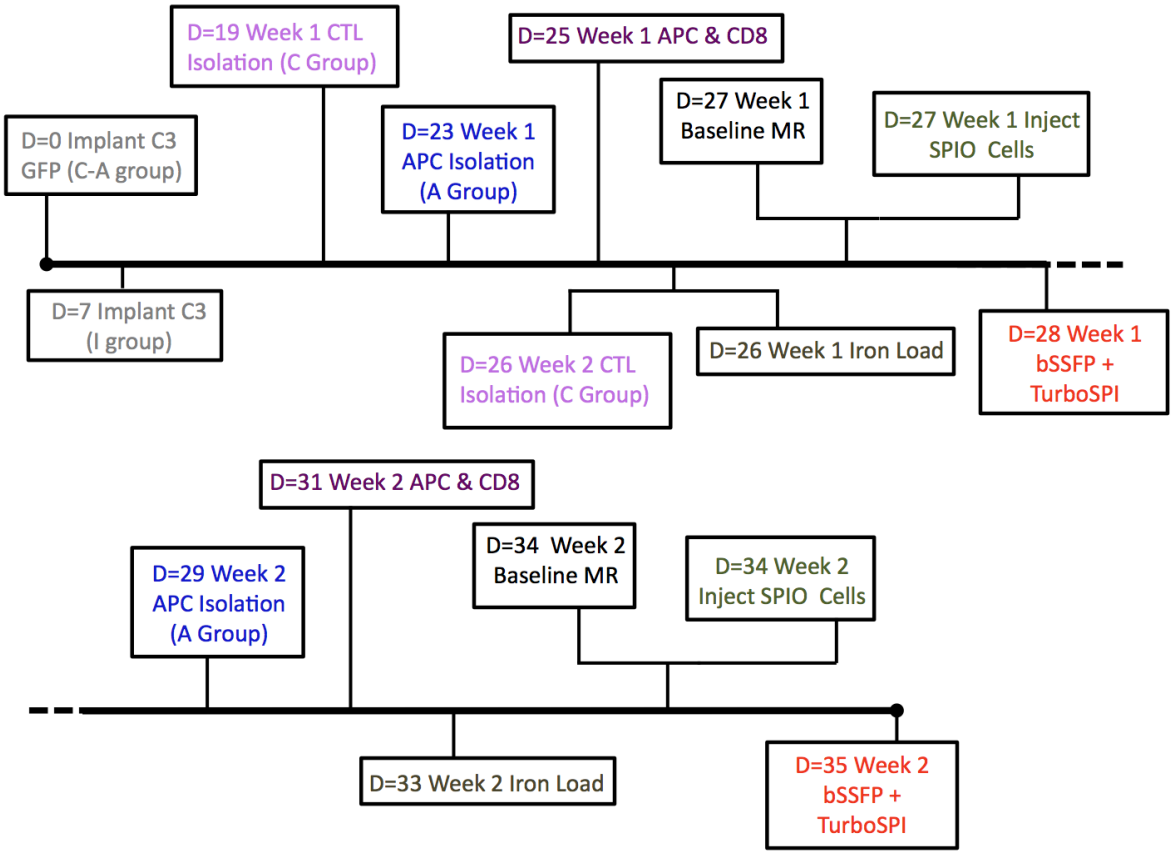

Figure A.1: Experimental timeline showing schedule for implant, cell preparation procedures, and imaging for the Untreated Group as described in Chapter 3

A.2 SOPs

Standard operating procedures (SOPs) for isolation, culture, SPIO loading, and tail vein injection of CTLs. These procedures were used for the *in vivo* cell tracking pilot study (Chapter 3) and *in vitro* cell labelling study (Chapter 5).

BIOTIC Imaging for Life		Page: **1 of 7**
		Executed by: MLT
Title: CD8+ activation and culture in the C3 cancer model		Reviewed by:
Document ID: **SOP BIO-006**	Issue: **01**	Date: 161003

1.0 Purpose: This document describes how to isolate and culture lymph node T cells to prepare cytotoxic CD8+ T cells culture for imaging.

3.0 Required Documents and References
SOP BIO-001: Preparation of trypan blue solution and cell counting

4.0 Equipment

Class II laminar airflow cabinet
Electric/rechargeable pipettor
10 ml sterile pipets
5 ml sterile pipets
15ml polypropylene tubes (Falcon, Corning or similar)
50ml polypropylene tubes
40µm cell strainer
100x 15mm petri dishes (such as Fisher, #08-757-12)
6 well plates
Scissors
Forceps

5.0 Reagents

- CD8+ cell Medium (see BIO-004):
  - 1 bottle of RPMI 1640 (Sigma, #R8758)
  - 50 mL of Fetal Bovine Serum (HyClone, SH30396.03)
  - 5 mL of Penicillin-Streptomycin solution (Gibco #15140-122)
  - 500 uL of 1M cell grade B-mercaptoethanol
- 1X Phosphate Buffered Saline (PBS) (Gibco, #10010)
- Human IL-2 cytokine (Stock $3.33x10^5$ U/mL) (Peprotech #315-03)
- 2% FBS in HBSS++ (+10mM HEPES)
- 10% FBS in HBSS++ (+10mM HEPES)
- 0.5% BSA in HBSS++
- RPMI 1640
- R9F peptide in DMSO (5mg/mL)

BIOTIC Imaging for Life		Page: **2 of 7**
		Executed by: MLT
Title: CD8+ activation and culture in the C3 cancer model		Reviewed by:
Document ID: **SOP BIO-006**	Issue: **01**	Date: 161003

6.0 Protocol

To ensure that steps 7 – 28 are done under aseptic conditions, basic guidelines are followed: Use of gloves when handling materials, autoclaved glassware/sterile plastic ware, autoclaved, filtered or sterile solutions used under the laminar flow hood.

Day -1

1. Coat a 6-well plate with 1ug/ml of 145-2C11 (hamster anti-mouse CD3) in 1 ml of PBS. Place the flask at 4^{o}C overnight or for 4-5h at R.T.; ensure flask is level and well hydrated. → _____ul
2. Coat a bacteriological petri dish (not tissue culture dish) with Goat anti rat IgG as follows:
    a. Add 8ml of sterile PBS.
    b. Add Goat anti rat IgG to obtain a final concentration of 10ug/ml in sterile PBS (80ug – from 2.5mg/ml of stock, use 37ul).
    c. Place the dish at 4^{o}C overnight

Day 0 - General

3. # of mice_____ Cage#_____

Mice identification_____

Day 0 (LN only)

4. Lymph nodes (LNs) are briefly stored in fresh sterile ELISPOT media in a microfuge tube. 1-2 tube/mouse. LNs: Inguinal, axillary, brachial, mesenteric, and submandibular.
5. A 40um cell strainer is placed on top of a 50 mL falcon tube and ~5ml of ELISPOT media is poured into it. LNs are then put in the cell strainer and crushed using a 3ml syringe plunger. Add 1 mL of media to filter cells through as the LNs are being crushed.
    a. NOTE: All LNs from the same group can be combined in one tube. Change cell strainer each 3 mice.
6. The cell strainer is rinsed with ~2-3ml of ELISPOT media.
7. Cells are centrifuged for 5 min @ 300 g (rcf). Wash with RPMI media once, resuspend, centrifuge, and add 3mL/mouse of ELISPOT media.
8. Cells are counted (1:10 in trypan blue- i.e. put 10µl of cells in 90µl of trypan blue).

BIOTIC Imaging for Life		Page: **3 of 7**
		Executed by: MLT
Title: CD8+ activation and culture in the C3 cancer model		Reviewed by:
Document ID: **SOP BIO-006**	Issue: **01**	Date: 161003

Cells counted	$\times 10^4$ (cells/mL)	D.F. (s)	Total # of cells

Discarted _____mL, kept_____cells. Only keep max of $1.5x10^8$ cells

9. Cells are resuspended in $1x10^8$ cells/ml in RPMI + 5% FBS for further purification.
10. Treat cells with:
    a. 25ug/ml rat anti-mouse CD4 (clone GK1.5 eBioscience) → _____µl (from stock 1.0mg/ml)
    b. 50ug/ml rat anti-mouse IgG1 kappa (clone 187.1) → _____µl (from stock 0.5mg/ml)
11. Incubate cells for 40 minutes at 4°C, mixing every 15 minutes. Proceed to next step immediately.
12. Rinse the anti-rat IgG coated petri dishes 4x using sterile PBS, block for 60min with 5ml of filter sterilized HBSS++ with 0.5% BSA. Take a 40min break!
13. After 40min, wash the cells twice using cold HBSS++ + 2% FBS and resuspend in 6ml HBSS++ + 10% FBS (both with 20mM HEPES).
14. Remove the blocking HBSS++ from the petri dish and add cell suspension (do not exceed 5-7x 10^7 cells/dish). Incubate for 40 minutes at 4°C. # of dishes:_____
15. Gently collect non-adherent cells and rinse the dish once with 5ml cold RPMI, centrifuge, resuspend in ~3mL of ELISPOT, then collect a small cell sample and count the cells 1:10 in trypan blue.

Cells counted	(avg)$\times 10^4$ (cells/mL)	D.F. (s)	Total # of cells

Discarted _____mL, kept_____cells. Do not need more than $6x10^6$ cells.

16. Spin the cells and resuspend them in ELISPOT media at $5x10^5$ cells/ml in 2 ml/well in a 6-well plate.
17. Add to cell suspension:
    a. **0.3 uL/mL** of human IL-2 → _____ul (100 U/ml from stock $3.33x10^5$U/mL)
    b. **10 uL/mL** of mouse IL-12 → _____ul (1ng/ml from stock 100ng/mL)
    c. **1.0uL/mL** of hamster anti-mouse CD28 → _____ul (1ug/ml from stock 0.5mg/ml) (clone 37.51 from eBioscience)
    d. **.5 uL/mL** (5ug/ml) of Gentamicin → _____ul (from stock 10mg/ml)

18. Remove unbound 145-2C11 antibody from coated flask by rinsing 3-4X with sterile PBS. Add cell suspension to the coated flasks (_____ml). Incubate at 37°C for 72 hours.

Day 3 (CD8)

Add 1 mL of warm ELISPOT media to each well.

Day 4 (CD8)

5. Warm up ELISPOT media to 37˚C
6. Collect activated CD8 cells from their plate into 15ml centrifuge tube, spin down, resuspend in 10mL of ELISPOT 0.3uL/mL (100 units/mL) of human IL-2 in one T25 flasks

5 days before injections (APC only)

5. Spleens are collected and (1 spleen per 3 mice LN CD8+ isolation) washed briefly in fresh ELISPOT media.
6. A 40um cell strainer is placed on top of a 50 mL falcon tube and ~5ml of 1x RBC lysis buffer (10X diluted to 1X in Steril water) is poured into the strainer. Spleens are then put in the cell strainer and crushed using a 3ml syringe plunger. Add ~1 mL of 1x RBC lysis buffer to filter cells through.
7. Wait 5 minutes for red blood cells to lyse then add an equal volume of RPMI media to neutralize the buffer. Centrifuge cells at 300g for 5 min and aspirate supernatant. If pellet is red, add 5mL of 1x RBC lysis buffer, re-suspend cells, and wait another 5 min. Then add C3 media in equal volume. Centrifuge. Pellet should be white/light brown.
8. The supernatant is aspirated and the pellet is resuspended in 3 ml of C3 media.
9. Filter cells again through a 40um filter to remove excess cell debris.
10. Cells were counted (1:100 in trypan blue- i.e. put 10uL of cells in 90uL of trypan blue, then take 10uL of suspension and put in fresh 90uL of trypan blue).

Cells counted	(avg)×10^4 (cells/mL)	D.F. (s)	Total # of cells

BIOTIC Imaging for Life		Page: **5 of 7**
		Executed by: MLT
Title: CD8+ activation and culture in the C3 cancer model		Reviewed by:
Document ID: **SOP BIO-006**	Issue: **01**	Date: 161003

11. Resuspended cells at $5x10^6$ cells/ml cell suspension (in C3 media) and transferred to T75 tissue culture flasks (20 ml per flask, 1 flask/spleen).
12. Incubated at 37°C for 2 hours and collected non-adherent cells, transferred to a 50ml tube.
13. Centrifuged, discarded supernatant and resuspended cells in 10mL C3 media, performed cell count (1:10 trypan blue) and adjusted to $4x10^6$ cells/ml and transferred 10ml to a small flasks.
14. Add LPS to a final concentration of 10ug/ml (stock 1mg/mL) and mix well.
15. Cultured cells for 48 hours at 37°C.

Day 5 (CD8)

5. If media is orange/discoloured and there is an obvious cell suspension, proceed to next step.
6. Dilute cells with 5mL of ELISPOT media with 0.3uL/mL added (100 U/ml) of human IL-2 a medium flask.
7. Return to incubator.

Day 6 or 7 (CD8)

5. Dilute activated CD8 cells to 30ml (+15mL) with warm ELISPOT media.
6. Add 0.3uL/mL (100 units/ml) of human IL-2
7. Return to incubator.
8. Cells will grow fast. Check flask everyday to make sure cells don't overgrow their flask by watching the discoloration of the flask.

3 days before injection

9. After LPS activation, spleen/APC cells were collected by swirling the flask to collect non-adherent cells, transferred to a 50mL tube and centrifuged, discarding the supernatant. Flask should be rinsed with fresh media to help collect the non-adherent cells.
10. Pool cells, resuspended in 20mL C3 media, take a sample for cell count (1:10 trypan blue), and centrifuged again to remove traces of LPS.

Cells counted	(avg)×10^4 (cells/mL)	D.F. (s)	Total # of cells

11. Resuspended cells at $5x10^7$ cells/mL in ELISPOT media in a 50ml tube, wrap tube in aluminum foil. Keep away from light.
12. Added _____ul mitomycin C stock (0.5 mg/mL) to cell suspension at a final concentration of 50 ug/mL.
13. Mixed and incubated for 20 minutes at 37°C, still wrapped in aluminum foil.
14. Fill tube to 50mL of ELISPOT media and centrifuge.
15. Discarded the supernatant and repeated washing cycle two more times to remove all traces of mitomycin C. (Three washes are crucial with lots of media.)
16. Resuspended cells at concentration of _____cells/mL.
17. Added APC cells to flasks at a ratio of 6:1 (CD8:APC cells). APC cells should therefore be at $0.5x10^5$ cells/ml concentration (added _____uL cells/flask).
18. Added 0.3ul/mL of human IL-2 to flask.
19. ***C3 tumors only: Add _____ of R9F to flasks (at 10 g/mL of 5 mg/mL stock solution). Return to incubator.***
20. ***Ovarian tumors only: Add _____ of Survivin to flasks (at 10 g/mL from stock solution). Return to incubator.***

16-24h before cell injections

21. Collect activated cells from the flask into 50ml centrifuge tube, spin down, resuspend and count cells.

Cells counted	(avg)×10^4 (cells/mL)	D.F. (s)	Total # of cells

22. **Take a small sample of cells (~0.5-1x10^6cells) for FACS (3 tubes: no stain, CD8CD3CD4, and CD11c)**
23. Dilute cells in fresh ELISPOT media with 100 U/ml of human IL-2 (added _____uL) to $4.0x10^6$ cells/mL in fresh small flasks. Used _____mL of ELISPOT media.
24. Add _____ of SPIO-Rhodamine B (stock solution 2 mg/mL) to flasks at concentration of 0.075 mg/mL. Ensure iron is swirled through flask. Return to incubator.

25. After four hours, add magnet under flasks (in 37°C incubator).

Injection prep

21. Collect cells in a 50mL conical tube and spin the cells down at 300g for 5 min. Place cells on ice.
22. Wash cells with ~50mL of cold (on ice) 1X PBS 2 times.
23. Wash cells with ~30mL of cold (on ice) HBSS++ 2times.
24. Resuspend cells at $40x10^6$ cells/mL (or ~$8x10^6$ cells/inj) in HBSS++ with 20mM HEPES. Keep cells on ice.

Document Revision History:

Issue	Change Initiated by	Change(s) made	Effective Date
01	MLT		161003

BIOTIC Imaging for Life	Page: 1 of 1
	Executed by: ACN
Title: Intravenous injections of immune cells	Reviewed by:
Document ID: **BMRL-09**	Date: 170727

1.0 Purpose: BMRL uses immune cell adoptive transfer to assess the migration of various populations of immune cells pre-clinically in various mouse cancer models. To ensure consistency and comparability between studies, route of administration procedures must be well defined. The purpose of this Standard Operating Procedure (SOP) is to describe approved procedures for performing intravenous injection of immune cells into the lateral tail vein of mice.

2.0 Scope: Describes the best methods for performing intravenous injections.

3.0 Materials:
- Gloves and lab coat
- 27 gauge ½ inch needle
- 0.3-1 cc syringe
- Beaker of water heated to 38-40° C
- gauze

4.0 Procedure: Prior to injections, cells are prepared at an appropriate concentration per injection (varies with cell type) in Hank's balanced salt solution (HBSS; an immunogenically inert buffer) with 20 mM HEPES. The volume of injection should not exceed 200 µL per mouse.

4.1 Place the mouse in rodent restraint device.
4.2 Dip the full tail of the mouse in warm water for 15-20 seconds to encourage vasodilation of the tail vein.
4.3 Dry the tail with gauze and use pressure to occlude the vein at the base of the tail while holding the tip of the tail to create tension.
4.4 With the injection needle in hand, locate the vessel and position the needle parallel to the tail with the bevel upwards, starting at the bottom 1/3 of the tail (can move proximally if multiple attempts are necessary).
4.5 Insert needle tip very shallowly. Release the occlusion of the vein and carefully depress the plunger. The pressure should be smooth with little resistance. If the tissue around the vein blanches, it is likely that the needle is out of position. Withdraw the needle and make another attempt at another injection site.
4.6 Following a successful injection, withdraw the needle and apply pressure to the injection site until bleeding has stopped.
4.7 Return mouse to cage for recovery.

Originally written July 27, 2017

Appendix B

Supplementary Data: Chapter 5

B.1 Phantom C *No Fat Sat* - Phase Error

Comparing phase data for the doped water in Phantom C *no fat sat* versus other phantoms reveals the dramatic phase error responsible for poor fitting in Figures 5.14 (left) and 5.17 (left). Magnitude data were unaffected which explains why the simple mono-exponential fit succeeded (since it does not consider phase).

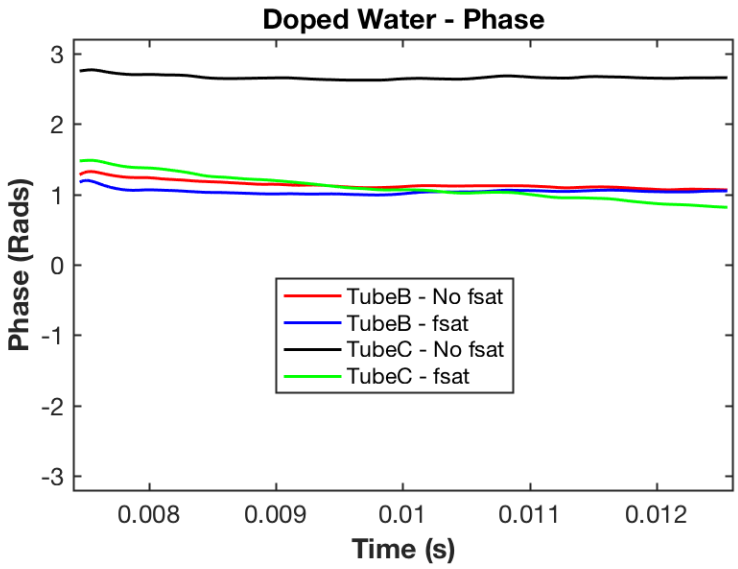

Figure B.1: Signal time course (phase) for the doped water in Phantoms B and C, acquired with and without fat saturation. The large phase offset in Phantom C *no fat sat* is quite significant. It may have resulted from a bad shim/experimental error.

Appendix C

Supplementary Data

C.1 Preliminary *In Vivo* Demonstration: R_2* Comparisons

The hybrid technique exhibits less erroneously fat voxels than the simple *mono-exponential* technique, but more than *mono-exponential with elimination*. However, it may result in fewer underestimates than fitting with strict *mono-exponential with elimination*. As indicated by *in vitro* data, the hybrid technique likely performs better for mixed voxels. Rather than fitting data solely with the hybrid technique, an interesting future direction may include an adaptive approach that uses a metric (perhaps fat fraction) to prescribe the fit method.

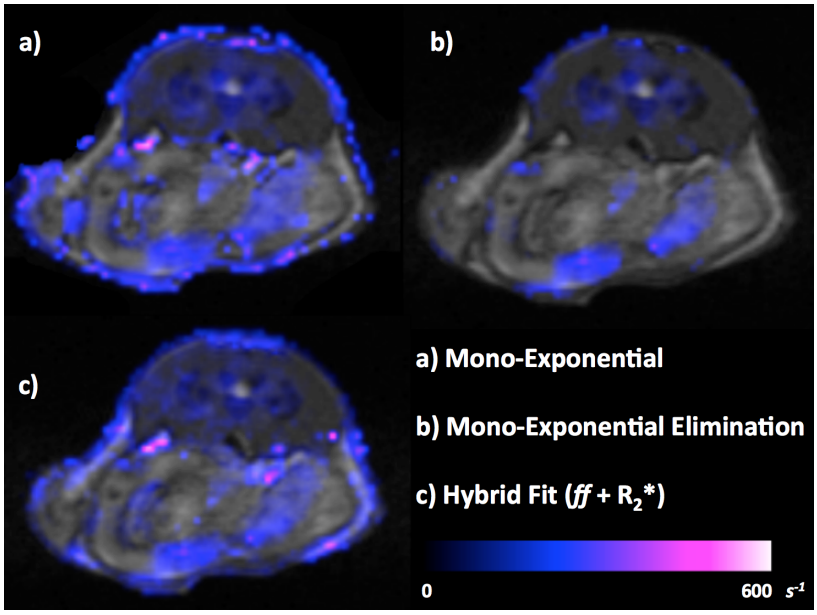

Figure C.1: Preliminary *in vivo* demonstration of the R_2* overlay produced by the hybrid technique (bottom left) with comparisons to *mono-exponential* (top left) and *mono-exponential with elimination* (top right) fitting.

Bibliography

[1] Ralph Weissleder, Brian S. Ross, Alnawaz Rehemtulla, and Sanjiv Sam Gambhir. *Molecular Imaging Principles and Practice*. People's Medical Publishing House-USA, Shelton, CT, 2010.

[2] Luisa Ottobrini, Cristina Martelli, Daria Lucia Trabattoni, Mario Clerici, and Giovanni Lucignani. In vivo imaging of immune cell trafficking in cancer. *European Journal of Nuclear Medicine and Molecular Imaging*, 38(5):949–968, 2011.

[3] PhRMA. Biopharmaceutical Research Industry Profile, 2015.

[4] Lauren Gravitz. Cancer immunotherapy. *Nature*, 504(7480):S1–S1, dec 2013.

[5] Anand Rotte and Madhuri Bhandaru. Challenges of Immunotherapy. In *Immunotherapy of Melanoma*, pages 419–434. Springer International Publishing, Cham, 2016.

[6] Peter Parham and C Janeway. *The Immune System*. Garland Science, New york, NY, 4th edition, 2014.

[7] Mark J Smyth, Gavin P Dunn, and Robert D B T Advances in Immunology Schreiber. Cancer Immunosurveillance and Immunoediting: The Roles of Immunity in Suppressing Tumor Development and Shaping Tumor Immunogenicity. In *Cancer Immunotherapy*, volume 90, pages 1–50. Academic Press, 2006.

[8] Daniel E Speiser, Ping-Chih Ho, and Grégory Verdeil. Regulatory circuits of T cell function in cancer. *Nature Reviews Immunology*, 16:599, aug 2016.

[9] Yi-Xiang J Wang. Superparamagnetic iron oxide based MRI contrast agents: Current status of clinical application. *Quantitative Imaging in Medicine and Surgery*, 1(1):35–40, dec 2011.

[10] Eric T Ahrens and Jeff W M Bulte. Tracking immune cells in vivo using magnetic resonance imaging. *Nature reviews. Immunology*, 13(10):10.1038/nri3531, oct 2013.

[11] John F. Schenck. The role of magnetic susceptibility in magnetic resonance imaging: MRI magnetic compatibility of the first and second kinds. *Medical Physics*, 23(6):815–850, jun 1996.

[12] Chris V. Bowen, Xiaowei Zhang, George Saab, Paula J. Gareau, and Brian K. Rutt. Application of the static dephasing regime theory to superparamagnetic iron-oxide loaded cells. *Magnetic Resonance in Medicine*, 48(1):52–61, jul 2002.

[13] Hannes Dahnke, Wei Liu, Daniel Herzka, Joseph A Frank, and Tobias Schaeffter. Susceptibility Gradient Mapping (SGM): A New Postprocessing Method for Positive Contrast Generation Applied to Superparamagnetic Iron Oxide Particle (SPIO)-Labeled Cells. *Magnetic resonance in medicine : official journal of the Society of Magnetic Resonance in Medicine / Society of Magnetic Resonance in Medicine*, 60(3):595–603, sep 2008.

[14] Werner Krause. *Contrast Agents I.* Springer-Verlag Berlin Heidelberg New York, Germany, 2002.

[15] M.A. Hayat. *Cancer Imaging: Lung and Breast Carcinomas, Volume 1.* Elsevier Academic Press, Burlington, MA, 2008.

[16] Michel Modo, Mathias Hoehn, and Jeff W M Bulte. Cellular MR Imaging. *Molecular Imaging*, 4(3):15353500200505145, jul 2005.

[17] Andre S. Merbach, Lothar Helm, and Eva Toth. *The Chemistry of Contrast Agents in Medical Magnetic Resonance Imaging.* John Wiley & Sons, Ltd., West Sussex, 2nd edition, 2013.

[18] Michel Mathias Jeannot Joseph. Modo and Jeff W. M. Bulte. *Molecular and cellular MR imaging.* CRC Press, 2007.

[19] Ali S Arbab, Branislava Janic, Jodi Haller, Edyta Pawelczyk, Wei Liu, and Joseph A Frank. In Vivo Cellular Imaging for Translational Medical Research. *Current medical imaging reviews*, 5(1):19–38, feb 2009.

[20] Ali M. Rad, Ali S. Arbab, A.S.M. S M Iskander, Quan Jiang, and Hamid Soltanian-Zadeh. Quantification of Superparamagnetic Iron Oxide (SPIO)-labeled Cells Using MRI. *Journal of magnetic resonance imaging : JMRI*, 26(2):366–374, aug 2007.

[21] Andrew Elias and Andrew Tsourkas. Imaging circulating cells and lymphoid tissues with iron oxide nanoparticles. *Hematology. American Society of Hematology. Education Program*, 2009(1):720–6, 2009.

[22] D J Widder, W L Greif, K J Widder, R R Edelman, and T J Brady. Magnetite albumin microspheres: a new MR contrast material. *American Journal of Roentgenology*, 148(2):399–404, feb 1987.

[23] Lee Josephson, Jerome Lewis, Paula Jacobs, Peter F Hahn, and David D Stark. The effects of iron oxides on proton relaxivity. *Magnetic Resonance Imaging*, 6(6):647–653, sep 1988.

[24] D Stark, R Weissleder, G Elizondo, P F Hahn, S Saini, L E Todd, J Wittenberg, and J T Ferrucci. Superparamagnetic iron oxide: clinical application as a contrast agent for MR imaging of the liver. *Radiology*, 168(2):297–301, aug 1988.

[25] R Weissleder, P F Hahn, D D Stark, G Elizondo, S Saini, L E Todd, J Wittenberg, and J T Ferrucci. Superparamagnetic iron oxide: enhanced detection of focal splenic tumors with MR imaging. *Radiology*, 169(2):399–403, nov 1988.

[26] S Majumdar, S Zoghbi, C F Pope, and J C Gore. Quantitation of MR relaxation effects of iron oxide particles in liver and spleen. *Radiology*, 169(3):653–658, dec 1988.

[27] S. Majumdar, S. Zoghbi, C. F. Pope, and J. C. Gore. A quantitative study of relaxation rate enhancement produced by iron oxide particles in polyacrylamide gels and tissue. *Magnetic Resonance in Medicine*, 9(2):185–202, feb 1989.

[28] S. Majumdar, S. S. Zoghbi, and J. C. Gore. The influence of pulse sequence on the relaxation effects of superparamagnetic iron oxide contrast agents. *Magnetic Resonance in Medicine*, 10(3):289–301, jun 1989.

[29] Sebastian Cerdan, Hans Ruedi Lötscher, Basil Künnecke, and Joachim Seelig. Monoclonal antibody-coated magnetite particles as contrast agents in magnetic resonance imaging of tumors. *Magnetic Resonance in Medicine*, 12(2):151–163, nov 1989.

[30] R Weissleder, D D Stark, B L Engelstad, B R Bacon, C C Compton, D L White, P Jacobs, and J Lewis. Superparamagnetic iron oxide: pharmacokinetics and toxicity. *American Journal of Roentgenology*, 152(1):167–173, jan 1989.

[31] P A Hardy and R M Henkelman. Transverse relaxation rate enhancement caused by magnetic particulates. *Magnetic Resonance Imaging*, 7(3):265–275, 1989.

[32] R Weissleder, G Elizondo, J Wittenberg, C A Rabito, H H Bengele, and L Josephson. Ultrasmall superparamagnetic iron oxide: characterization of a new class of contrast agents for MR imaging. *Radiology*, 175(2):489–493, may 1990.

[33] A K Fahlvik, E Holtz, and J Klaveness. Relaxation efficacy of paramagnetic and superparamagnetic microspheres in liver and spleen. *Magnetic resonance imaging*, 8(4):363–9, 1990.

[34] R. L. Magin, G. Bacic, M. R. Niesman, J. C. Alameda, S. M. Wright, and H. M. Swartz. Dextran magnetite as a liver contrast agent. *Magnetic Resonance in Medicine*, 20(1):1–16, jul 1991.

[35] D Pouliquen, J J Le Jeune, R Perdrisot, A Ermias, and P Jallet. Iron oxide nanoparticles for use as an MRI contrast agent: Pharmacokinetics and metabolism. *Magnetic Resonance Imaging*, 9(3):275–283, 1991.

[36] D. Pouliquen, H. Perroud, F. Calza, P. Jallet, and J. J. Le Jeune. Investigation of the magnetic properties of iron oxide nanoparticles used as contrast agent for MRI. *Magnetic Resonance in Medicine*, 24(1):75–84, mar 1992.

[37] Peter Reimer, Kenneth K. Kwong, Robert Weisskoff, Mark S. Cohen, Thomas J. Brady, and Ralph Weissleder. Dynamic signal intensity changes in liver with superparamagnetic MR contrast agents. *Journal of Magnetic Resonance Imaging*, 2(2):177–181, mar 1992.

[38] R. Weissleder and P. Reimer. Superparamegnetic iron oxides for MRI. *European Radiology*, 3(3):198–212, 1993.

[39] R Weissleder, H C Cheng, A Bogdanova, and A Bogdanov. Magnetically labeled cells can be detected by MR imaging. *Journal of magnetic resonance imaging : JMRI*, 7(1):258–63, 1997.

[40] U Schoepf, E M Marecos, R J Melder, R K Jain, and R Weissleder. Intracellular magnetic labeling of lymphocytes for in vivo trafficking studies. *BioTechniques*, 24(4):642–6, 648–51, apr 1998.

[41] S J Dodd, M Williams, J P Suhan, D S Williams, A P Koretsky, and C Ho. Detection of single mammalian cells by high-resolution magnetic resonance imaging. *Biophysical Journal*, 76(1 Pt 1):103–109, jan 1999.

[42] Vincent Dousset, Christophe Delalande, Lucrecia Ballarino, Bruno Quesson, Danielle Seilhan, Monique Coussemacq, Eric Thiaudiére, Bruno Brochet, Paul Canioni, and JeanMarie Caillé. In vivo macrophage activity imaging in the central nervous system detected by magnetic resonance. *Magnetic Resonance in Medicine*, 41(2):329–333, feb 1999.

[43] J W M Bulte, S-C Zhang, P van Gelderen, V Herynek, E K Jordan, I D Duncan, and J A Frank. Neurotransplantation of magnetically labeled oligodendrocyte progenitors: Magnetic resonance tracking of cell migration and myelination. *Proceedings of the National Academy of Sciences of the United States of America*, 96(26):15256–15261, dec 1999.

[44] Anna Moore, Edgardo Marecos, Alexei Bogdanov, and Ralph Weissleder. Tumoral Distribution of Long-circulating Dextran-coated Iron Oxide Nanoparticles in a Rodent Model. *Radiology*, 214(2):568–574, feb 2000.

[45] Maïté Lewin, Nadia Carlesso, Ching-Hsuan Tung, Xiao-Wu Tang, David Cory, David T. Scadden, and Ralph Weissleder. Tat peptide-derivatized magnetic nanoparticles allow in vivo tracking and recovery of progenitor cells. *Nature Biotechnology*, 18(4):410–414, apr 2000.

[46] Martin Rausch, Andre Sauter, Johannes Fröhlich, Ute Neubacher, Ernst W. Radü, and Markus Rudin. Dynamic patterns of USPIO enhancement can be

observed in macrophages after ischemic brain damage. *Magnetic Resonance in Medicine*, 46(5):1018–1022, nov 2001.

[47] Christopher H Dodd, Hui-Chen Hsu, Wen-Jang Chu, Pingar Yang, Huang-Ge Zhang, John D Mountz, Kurt Zinn, John Forder, Lee Josephson, Ralph Weissleder, James M Mountz, and John D Mountz. Normal T-cell response and in vivo magnetic resonance imaging of T cells loaded with HIV transactivator-peptide-derived superparamagnetic nanoparticles. *Journal of Immunological Methods*, 256(1):89–105, 2001.

[48] Paula Foster-Gareau, Chris Heyn, Andrew Alejski, and Brian K. Rutt. Imaging single mammalian cells with a 1.5 T clinical MRI scanner. *Magnetic Resonance in Medicine*, 49(5):968–971, may 2003.

[49] Erik M Shapiro, Stanko Skrtic, Kathryn Sharer, Jonathan M Hill, Cynthia E Dunbar, and Alan P Koretsky. MRI detection of single particles for cellular imaging. *Proceedings of the National Academy of Sciences of the United States of America*, 101(30):10901–10906, jul 2004.

[50] Paul C Wang and Liang Shan. Essential Elements to Consider for MRI Cell Tracking Studies with Iron Oxide-based Labeling Agents. *Journal of basic and clinical medicine*, 1(1):1–6, 2012.

[51] Rebecca Kuhlpeter, Hannes Dahnke, Lars Matuszewski, Thorsten Persigehl, Angelika von Wallbrunn, Thomas Allkemper, Walter L Heindel, Tobias Schaeffter, and Christoph Bremer. R2 and R2* Mapping for Sensing Cell-bound Superparamagnetic Nanoparticles: In Vitro and Murine in Vivo Testing. *Radiology*, 245(2):449–457, nov 2007.

[52] Qingguo Wang, Kangan Li, Qimeng Quan, and Guixiang Zhang. R2* and R2 mapping for quantifying recruitment of superparamagnetic iron oxide-tagged endothelial progenitor cells to injured liver: tracking in vitro and in vivo. *International Journal of Nanomedicine*, 9:1815–1822, apr 2014.

[53] Gyula Kotek, Sandra T. van Tiel, Piotr A. Wielopolski, Gavin C. Houston, Gabriel P. Krestin, and Monique R. Bernsen. Cell quantification: evolution of compartmentalization and distribution of iron-oxide particles and labeled cells. *Contrast Media & Molecular Imaging*, 7(2):195–203, mar 2012.

[54] Stephan Metz, Gabriel Bonaterra, Martina Rudelius, Marcus Settles, Ernst J Rummeny, and Heike E Daldrup-Link. Capacity of human monocytes to phagocytose approved iron oxide MR contrast agents in vitro. *European Radiology*, 14(10):1851–1858, 2004.

[55] Yuyu Yao, Yuanyuan Wang, Yi Zhang, Yefei Li, Zulong Sheng, Song Wen, Genshan Ma, Naifeng Liu, Fang Fang, and Gao-Jun Teng. In Vivo Imaging of Macrophages during the Early-Stages of Abdominal Aortic Aneurysm Using High Resolution MRI in ApoE(/) Mice. *PLoS ONE*, 7(3):e33523, mar 2012.

[56] Christoper M Long and Jeff W M Bulte. In vivo tracking of cellular therapeutics using magnetic resonance imaging. *Expert opinion on biological therapy*, 9(3):293–306, mar 2009.

[57] Jeff W M Bulte, Piotr Walczak, Bernhard Gleich, Jürgen Weizenecker, Denis E Markov, Hans C J Aerts, Hans Boeve, Jörn Borgert, and Michael Kuhn. MPI Cell Tracking: What Can We Learn from MRI? *Proceedings of SPIE–the International Society for Optical Engineering*, 7965:79650z–79650z, 2011.

[58] Wei Liu and Joseph A Frank. Detection and Quantification of Magnetically Labeled Cells by Cellular MRI. *European journal of radiology*, 70(2):258–264, may 2009.

[59] Gerben M van Buul, Gyula Kotek, Piotr A Wielopolski, Eric Farrell, P Koen Bos, Harrie Weinans, Anja U Grohnert, Holger Jahr, Jan A N Verhaar, Gabriel P Krestin, Gerjo J V M van Osch, and Monique R Bernsen. Clinically Translatable Cell Tracking and Quantification by MRI in Cartilage Repair Using Superparamagnetic Iron Oxides. *PLoS ONE*, 6(2):e17001, feb 2011.

[60] Arthur Taylor, Katie M Wilson, Patricia Murray, David G Fernig, and Raphael Levy. Long-term tracking of cells using inorganic nanoparticles as contrast agents: are we there yet? *Chemical Society Reviews*, 41(7):2707–2717, 2012.

[61] Mangala Srinivas, Penelope A. Morel, Lauren A. Ernst, David H. Laidlaw, and Eric T. Ahrens. Fluorine-19 MRI for visualization and quantification of cell migration in a diabetes model. *Magnetic Resonance in Medicine*, 58(4):725–734, oct 2007.

[62] Mangala Srinivas, Arend Heerschap, Eric T Ahrens, Carl G Figdor, and I Jolanda M de Vries. (19)F MRI for quantitative in vivo cell tracking. *Trends in biotechnology*, 28(7):363–370, jul 2010.

[63] Matthew S Fox, Jeffrey M Gaudet, and Paula J Foster. Fluorine-19 MRI Contrast Agents for Cell Tracking and Lung Imaging. *Magnetic Resonance Insights*, 8(Suppl 1):53–67, mar 2015.

[64] Edward J Delikatny and Harish Poptani. MR techniques for in vivo molecular and cellular imaging. *Radiologic Clinics*, 43(1):205–220, sep 2017.

[65] Jacob W Aptekar, Maja C Cassidy, Alexander C Johnson, Robert A Barton, Menyoung Lee, Alexander C Ogier, Chinh Vo, Melis N Anahtar, Yin Ren, Sangeeta N Bhatia, Chandrasekhar Ramanathan, David G Cory, Alison L Hill, Ross W Mair, Matthew S Rosen, Ronald L Walsworth, and Charles M Marcus. Silicon Nanoparticles as Hyperpolarized Magnetic Resonance Imaging Agents. *ACS Nano*, 3(12):4003–4008, dec 2009.

[66] Nicholas Whiting, Jingzhe Hu, Niki M Zacharias, Ganesh L R Lokesh, David E Volk, David G Menter, Rajesha Rupaimoole, Rebecca Previs, Anil K Sood, and Pratip Bhattacharya. Developing hyperpolarized silicon particles for in vivo MRI targeting of ovarian cancer. *Journal of Medical Imaging*, 3(3):36001, jul 2016.

[67] Kimberly D Brewer, Olivia Stanely, Christa B Davis, Iulia Dude, Genevieve Weir, Mohan Karkada, Marc Mansour, and Chris Bowen. Tracking SPIO-Labeled Effector and Regulatory Cell Migration with MRI. In World Molecular Imaging Society, editor, *World Molecular Imaging Congress*, page Poster 076, Georgia, USA, 2013.

[68] Kimberly D Brewer, Kerry Lake, Nicole Pelot, Marianne M Stanford, Drew R DeBay, Andrea Penwell, Genevieve M Weir, Mohan Karkada, Marc Mansour, and Chris V Bowen. Clearance of depot vaccine SPIO-labeled antigen and substrate visualized using MRI. *Vaccine*, 32(51):6956–6962, dec 2014.

[69] Chris Heyn, Chris V. Bowen, Brian K. Rutt, and Paula J. Foster. Detection threshold of single SPIO-labeled cells with FIESTA. *Magnetic Resonance in Medicine*, 53(2):312–320, feb 2005.

[70] Chris Heyn, John A. Ronald, Lisa T. Mackenzie, Ian C. MacDonald, Ann F. Chambers, Brian K. Rutt, and Paula J. Foster. In vivo magnetic resonance imaging of single cells in mouse brain with optical validation. *Magnetic Resonance in Medicine*, 55(1):23–29, jan 2006.

[71] Lisa M. Bernas, Paula J. Foster, and Brian K. Rutt. Imaging iron-loaded mouse glioma tumors with bSSFP at 3 T. *Magnetic Resonance in Medicine*, 64(1):23–31, jul 2010.

[72] Emeline J. Ribot, Tom J. Duriez, Aurélien J. Trotier, Eric Thiaudiere, Jean-Michel Franconi, and Sylvain Miraux. Self-gated bSSFP sequences to detect iron-labeled cancer cells and/or metastases in vivo in mouse liver at 7 Tesla. *Journal of Magnetic Resonance Imaging*, 41(5):1413–1421, may 2015.

[73] Kimberly D Brewer, Drew R DeBay, Iulia Dude, Christa Davis, Kerry Lake, Cathryn Parsons, Rajkannan Rajagopalan, Genevieve Weir, Marianne M Stanford, Marc Mansour, and Chris V Bowen. Using lymph node swelling as a potential biomarker for successful vaccination. *Oncotarget*, 7(24):35655–35669, jun 2016.

[74] Erik H J G Aarntzen, Mangala Srinivas, Caius G Radu, Cornelis J A Punt, Otto C Boerman, Carl G Figdor, Wim J G Oyen, and I Jolanda M de Vries. In vivo imaging of therapy-induced anti-cancer immune responses in humans. *Cellular and Molecular Life Sciences*, 70(13):2237–2257, 2013.

[75] João Conniot, Joana M Silva, Joana G Fernandes, Liana C Silva, Rogério Gaspar, Steve Brocchini, Helena F Florindo, and Teresa S Barata. Cancer immunotherapy: nanodelivery approaches for immune cell targeting and tracking. *Frontiers in Chemistry*, 2:105, nov 2014.

[76] Moritz F Kircher, Jennifer R Allport, Edward E Graves, Victoria Love, Lee Josephson, Andrew H Lichtman, and Ralph Weissleder. In VivoHigh Resolution Three-Dimensional Imaging of Antigen-Specific Cytotoxic T-Lymphocyte Trafficking to Tumors. *Cancer Research*, 63(20):6838 LP – 6846, oct 2003.

[77] I Jolanda M de Vries, W Joost Lesterhuis, Jelle O Barentsz, Pauline Verdijk, J Han van Krieken, Otto C Boerman, Wim J G Oyen, Johannes J Bonenkamp, Jan B Boezeman, Gosse J Adema, Jeff W M Bulte, Tom W J Scheenen, Cornelis J A Punt, Arend Heerschap, and Carl G Figdor. Magnetic resonance tracking of dendritic cells in melanoma patients for monitoring of cellular therapy. *Nat Biotech*, 23(11):1407–1413, nov 2005.

[78] Heike E Daldrup-Link, Reinhardt Meier, Martina Rudelius, Guido Piontek, Morand Piert, Stephan Metz, Marcus Settles, Christoph Uherek, Winfried Wels, Jürgen Schlegel, and Ernst J Rummeny. In vivo tracking of genetically engineered, anti-HER2/neu directed natural killer cells to HER2/neu positive mammary tumors with magnetic resonance imaging. *European Radiology*, 15(1):4–13, 2005.

[79] Paula J Foster, Elizabeth A Dunn, Kristina E Karl, Jonatan A Snir, Colleen M Nycz, Alfred J Harvey, and Ron J Pettis. Cellular Magnetic Resonance Imaging: In Vivo Imaging of Melanoma Cells in Lymph Nodes of Mice. *Neoplasia (New York, N.Y.)*, 10(3):207–216, mar 2008.

[80] Rakesh K Jain and Neil S Forbes. Can engineered bacteria help control cancer? *Proceedings of the National Academy of Sciences*, 98(26):14748–14750, dec 2001.

[81] S Ganai, R B Arenas, J P Sauer, B Bentley, and N S Forbes. In tumors Salmonella migrate away from vasculature toward the transition zone and induce apoptosis. *Cancer Gene Ther*, 18(7):457–466, jul 2011.

[82] M Soltani and P Chen. Numerical Modeling of Fluid Flow in Solid Tumors. *PLOS ONE*, 6(6):e20344, jun 2011.

[83] Luca Persano, Elena Rampazzo, Alessandro Della Puppa, Francesca Pistollato, and Giuseppe Basso. The Three-Layer Concentric Model of Glioblastoma: Cancer Stem Cells, Microenvironmental Regulation, and Therapeutic Implications. *The Scientific World Journal*, 11:1829–1841, oct 2011.

[84] Mark S. Jacobson, Raymond A. Steichen, and Patrick J. Peller. PET Radiochemistry and Radiopharmacy. In Patrick Peller, Rathan Subramaniam, and Ali Guermazi, editors, *PET-CT and PET-MRI in Oncology: A Practical Guide*, pages 19–30. Springer-Verlag, 2012.

[85] Brad Kemp. PET Physics and Instrumentation. In Patrick Peller, Rathan Subramaniam, and Ali Guermazi, editors, *PET-CT and PET-MRI in Oncology: A Practical Guide*, pages 3–17. Springer-Verlag, 2012.

[86] S Ahmad Sarji. Physiological uptake in FDG PET simulating disease. *Biomedical Imaging and Intervention Journal*, 2(4):e59, oct 2006.

[87] Neil Sebire. *Oncology: Histopathology and imaging in the future*, volume 41. Springer-Verlag, may 2011.

[88] Takaaki Beppu, Kazunori Terasaki, Toshiaki Sasaki, Shunrou Fujiwara, Hideki Matsuura, Kuniaki Ogasawara, Koichiro Sera, Noriyuki Yamada, Noriyuki Uesugi, Tamotsu Sugai, Kohsuke Kudo, Makoto Sasaki, Shigeru Ehara, Ren Iwata, and Yoshihiro Takai. Standardized Uptake Value in High Uptake Area on Positron Emission Tomography with 18F-FRP170 as a Hypoxic Cell Tracer Correlates with Intratumoral Oxygen Pressure in Glioblastoma. *Molecular Imaging and Biology*, 16(1):127–135, 2014.

[89] Steven D Beyea, Bruce J Balcom, Igor V Mastikhin, Theodore W Bremner, Robin L Armstrong, and Patrick E Grattan-Bellew. Imaging of Heterogeneous Materials with a Turbo Spin Echo Single-Point Imaging Technique. *Journal of Magnetic Resonance*, 144(2):255–265, 2000.

[90] Steven D Beyea, Bruce J Balcom, Pablo J Prado, Albert R Cross, Christopher B Kennedy, Robin L Armstrong, and Theodore W Bremner. Relaxation Time Mapping of ShortT*2Nuclei with Single-Point Imaging (SPI) Methods. *Journal of Magnetic Resonance*, 135(1):156–164, 1998.

[91] James A Rioux, Kimberly D Brewer, Steven D Beyea, and Chris V Bowen. Quantification of superparamagnetic iron oxide with large dynamic range using TurboSPI. *Journal of Magnetic Resonance*, 216:152–160, 2012.

[92] James A Rioux, Steven D Beyea, and Chris V Bowen. 3D single point imaging with compressed sensing provides high temporal resolution R 2* mapping for in vivo preclinical applications. *Magnetic Resonance Materials in Physics, Biology and Medicine*, 30(1):41–55, 2017.

[93] Paul T. Callaghan. *Principles of nuclear magnetic resonance microscopy*. Clarendon Press, 1993.

[94] D.J. Griffiths. *Introduction to Quantum Mechanics*. Pearson Prentice Hall, Upper Saddle River, NJ, 2nd edition, 2005.

[95] Robert C Smith and C Lange, Robert. *Understanding Magnetic Resonance Imaging*. CRC Press LLC, Boca Raton, FL, 1998.

[96] Walter Fox. Smith. *Waves and oscillations : a prelude to quantum mechanics*. Oxford University Press, 2010.

[97] Jerrold T Bushberg, Anthony J Seibert, Edwin M Leidholdt, and John M Boone. *The Essential Physics of Medical Imaging*. Lippincott Williams & Williams, Philadelphia, PA, third edit edition, 2012.

[98] E Mark Haacke. *Magnetic resonance imaging : physical principles and sequence design*. New York : Wiley, New York, 1999.

[99] J P Hornak. *The Basics of MRI*. Rochester Institute of Technology, 1996.

[100] F Bloch, W W Hansen, and Martin Packard. Nuclear Induction. *Physical Review*, 69(3-4):127, feb 1946.

[101] E M Purcell, H C Torrey, and R V Pound. Resonance Absorption by Nuclear Magnetic Moments in a Solid. *Physical Review*, 69(1-2):37–38, jan 1946.

[102] Matt Bernstein, Kevin King, and Xiaohong Zhou. *Handbook of MRI Pulse Sequences*. Elsevier Academic Press, Burlington, MA, 1 edition, 2004.

[103] Ray H. Hashemi, William G. Bradley, and Christopher J. Lisanti. *MRI : the basics*. Lippincott Williams & Wilkins, 2010.

[104] Takeshi Yokoo, Won C Bae, Gavin Hamilton, Afshin Karimi, James P Borgstede, Brian C Bowen, Claude B Sirlin, Christine B Chung, John V Crues, William G Bradley, and Graeme M Bydder. A Quantitative Approach to Sequence and Image Weighting. *Journal of Computer Assisted Tomography*, 34(3):317–331, 2010.

[105] Zhi-Pei Liang, Paul C. Lauterbur, and IEEE Engineering in Medicine and Biology Society. *Principles of magnetic resonance imaging : a signal processing perspective*. SPIE Optical Engineering Press, 2000.

[106] Giuseppe. Placidi. *MRI : essentials for innovative technologies*. CRC Press, 2012.

[107] E L Hahn. Spin Echoes. *Physical Review*, 80(4):580–594, nov 1950.

[108] E. L. Hahn. Free nuclear induction. *Physics Today*, 6(11):4–9, nov 1953.

[109] H Y Carr and E M Purcell. *Effect of Diffusion on Free Precession in Nuclear Magnetic Resonance Experiments*, volume 94. Physical, may 1954.

[110] Pietro Carretta and Alessandro Lascialfari. *NMR-MRI uSR and Mossbauer Spectroscopies in Molecular Magnets*. Springer-Verlag Italia, Milano, 2007.

[111] A D Elster. Gradient-echo MR imaging: techniques and acronyms. *Radiology*, 186(1):1–8, jan 1993.

[112] Jacob. Beutel, Harold L. Kundel, Richard L. Van Metter, and Society of Photo-optical Instrumentation Engineers. *Handbook of medical imaging. Volume 1, Physics and psychophysics*. SPIE, 2000.

[113] Deborah Burstein. Stimulated echoes: Description, applications, practical hints. *Concepts in Magnetic Resonance*, 8(4):269–278, jan 1996.

[114] J Frahm, K D Merboldt, W Hänicke, and A Haase. Stimulated echo imaging. *Journal of Magnetic Resonance (1969)*, 64(1):81–93, 1985.

[115] Mushbbar A. Syed, Subha V. Raman, and Orlando P. Simonetti. *Basic Principles of Cardiovascular MRI*. Springer International Publishing, Switzerland, 2015.

[116] Klaus Scheffler. A pictorial description of steady-states in rapid magnetic resonance imaging. *Concepts in Magnetic Resonance*, 11(5):291–304, 1999.

[117] Govind B Chavhan, Paul S Babyn, Bhavin G Jankharia, Hai-Ling M Cheng, and Manohar M Shroff. EDUCATION EXHIBIT Steady-State MR Imaging Sequences: Physics, Classification, and Clinical Applications. *RadioGraphics*, 28(4):1147–1160, 2008.

[118] Klaus Scheffler and Stefan Lehnhardt. Principles and applications of balanced SSFP techniques. *European Radiology*, 13(11):2409–2418, nov 2003.

[119] Thomas Kahn and Harald Busse. *Interventional Magnetic Resonance Imaging*. Springer-Verlag Berlin Heidelberg, Germany, 2012.

[120] Klaus Scheffler and Jürgen Hennig. Is TrueFISP a gradient-echo or a spin-echo sequence? *Magnetic Resonance in Medicine*, 49(2):395–397, feb 2003.

[121] S Gravina and D G Cory. Sensitivity and Resolution of Constant-Time Imaging. *Journal of Magnetic Resonance, Series B*, 104(1):53–61, 1994.

[122] Wolfgang. Birkfellner and Michael. Figl. *Applied medical image processing : a basic course*. CRC Press, 2014.

[123] Terry M. Peters and Jackie. Williams. *The Fourier Transform in Biomedical Engineering*. Birkhauser Boston, 1998.

[124] Nadine Smith and Andrew Webb. *Introduction to medical imaging : physics, engineering and clinical applications*. Cambridge University Press, 2011.

[125] Michael Lustig, David Donoho, and John M Pauly. Sparse MRI: The application of compressed sensing for rapid MR imaging. *Magnetic Resonance in Medicine*, 58(6):1182–1195, dec 2007.

[126] Joseph K. T. Lee. *Computed body tomography with MRI correlation Volume 1*. Lippincott Williams & Wilkins, 2006.

[127] Maureen N Hood, Vincent B Ho, James G Smirniotopoulos, and Jerzy Szumowski. Chemical Shift: The Artifact and Clinical Tool Revisited. *RadioGraphics*, 19(2):357–371, mar 1999.

[128] L Brateman. Chemical shift imaging: a review. *American Journal of Roentgenology*, 146(5):971–980, may 1986.

[129] Andrew J Dwyer, Richard H Knop, and D I Hoult. Frequency Shift Artifacts in MR Imaging. *Journal of Computer Assisted Tomography*, 9(1), 1985.

[130] E E Babcock, L Brateman, J C Weinreb, S D Horner, and R L Nunnally. Edge artifacts in MR images: chemical shift effect. *Journal of computer assisted tomography*, 9(2):252–7, 1985.

[131] John R. Leyendecker, Jeffrey J. Brown, and Elmar M. Merkle. *Practical guide to abdominal and pelvic MRI*. Wolters Kluwer/Lippincott Williams & Wilkins Health, second edition, 2010.

[132] Thorsten A Bley, Oliver Wieben, Christopher J François, Jean H Brittain, and Scott B Reeder. Fat and water magnetic resonance imaging. *Journal of Magnetic Resonance Imaging*, 31(1):4–18, jan 2010.

[133] Jingfei Ma. Dixon techniques for water and fat imaging. *Journal of Magnetic Resonance Imaging*, 28(3):543–558, sep 2008.

[134] Gary H Glover. Multipoint dixon technique for water and fat proton and susceptibility imaging. *Journal of Magnetic Resonance Imaging*, 1(5):521–530, sep 1991.

[135] W T Dixon. Simple proton spectroscopic imaging. *Radiology*, 153(1):189–194, oct 1984.

[136] G H Glover and E Schneider. Three-point dixon technique for true water/fat decomposition with B0 inhomogeneity correction. *Magnetic Resonance in Medicine*, 18(2):371–383, apr 1991.

[137] Bernard D Coombs, Jerzy Szumowski, and William Coshow. Two-point Dixon technique for water-fat signal decomposition with B0 inhomogeneity correction. *Magnetic Resonance in Medicine*, 38(6):884–889, dec 1997.

[138] Scott B Reeder, Angel R Pineda, Zhifei Wen, Ann Shimakawa, Huanzhou Yu, Jean H Brittain, Garry E Gold, Christopher H Beaulieu, and Norbert J Pelc. Iterative decomposition of water and fat with echo asymmetry and least-squares estimation (IDEAL): Application with fast spin-echo imaging. *Magnetic Resonance in Medicine*, 54(3):636–644, sep 2005.

[139] Huanzhou Yu, Charles A. McKenzie, Ann Shimakawa, Anthony T. Vu, Anja C.S. Brau, Philip J. Beatty, Angel R. Pineda, Jean H. Brittain, and Scott B. Reeder. Multiecho reconstruction for simultaneous water-fat decomposition and T2* estimation. *Journal of Magnetic Resonance Imaging*, 26(4):1153–1161, oct 2007.

[140] Mariet C W Feltkamp, Henk L Smits, Michel P M Vierboom, René P Minnaar, Barteld M De Jongh, Jan Wouter Drijfhout, Jan Ter Schegget, Cornelis J M Melief, and W Martin Kast. Vaccination with cytotoxic T lymphocyte epitope-containing peptide protects against a tumor induced by human papillomavirus type 16-transformed cells. *European Journal of Immunology*, 23(9):2242–2249, sep 1993.

[141] Kent A Smith, Brenna L Meisenburg, Victor L Tam, Robb R Pagarigan, Raymond Wong, Diljeet K Joea, Liz Lantzy, Mayra A Carrillo, Todd M Gross, Uriel M Malyankar, Chih-Sheng Chiang, Diane M Da Silva, Thomas M Kündig, W Martin Kast, Zhiyong Qiu, and Adrian Bot. Lymph Node-Targeted Immunotherapy Mediates Potent Immunity Resulting in Regression of Isolated or Metastatic HPV-Transformed Tumors. *Clinical cancer research : an official journal of the American Association for Cancer Research*, 15(19):6167–6176, oct 2009.

[142] Genevieve M Weir, Olga Hrytsenko, Marianne M Stanford, Neil L Berinstein, Mohan Karkada, Robert S Liwski, and Marc Mansour. Metronomic cyclophosphamide enhances HPV16E7 peptide vaccine induced antigen-specific and cytotoxic T-cell mediated antitumor immune response. *Oncoimmunology*, 3(8):e953407, nov 2014.

[143] Genevieve M Weir, Olga Hrytsenko, Tara Quinton, Neil L Berinstein, Marianne M Stanford, and Marc Mansour. Anti-PD-1 increases the clonality and activity of tumor infiltrating antigen specific T cells induced by a potent immune therapy consisting of vaccine and metronomic cyclophosphamide. *Journal for Immunotherapy of Cancer*, 4:68, oct 2016.

[144] S V Graham. Human papillomavirus: gene expression, regulation and prospects for novel diagnostic methods and antiviral therapies. *Future microbiology*, 5(10):1493–1506, oct 2010.

[145] Li-Li Li, He-Rong Wang, Zhi-Yi Zhou, Jing Luo, Xiao-Li Wang, Xiang-Qian Xiao, Yu-Bai Zhou, and Yi Zeng. C3-Luc Cells Are an Excellent Model for Evaluation of Cellular Immunity following HPV16L1 Vaccination. *PLoS ONE*, 11(2):e0149748, feb 2016.

[146] Mohan Karkada, Genevieve M Weir, Tara Quinton, Leeladhar Sammatur, Lisa D Macdonald, Alecia Grant, Robert Liwski, Ridas Juskevicius, Gomathinayagam Sinnathamby, Ramila Philip, and Marc Mansour. A Novel Breast/Ovarian Cancer Peptide Vaccine Platform That Promotes Specific Type-1 but not Treg/Tr1-type Responses. *J Immunother*, 33(3):250–261, 2010.

[147] Marie-Laurence Tremblay, Christa Davis, Chris V Bowen, Olivia Stanley, Cathryn Parsons, Genevieve Weir, Mohan Karkada, Marianne M Stanford, and Kimberly D Brewer. Using MRI cell tracking to monitor immune cell recruitment in response to a peptide-based cancer vaccine. *Magnetic Resonance in*

Medicine, (Online Version of Record published before inclusion in an issue), 2017.

[148] Chrisann Kyi and Michael A. Postow. Checkpoint blocking antibodies in cancer immunotherapy. *FEBS Letters*, 588(2):368–376, jan 2014.

[149] Drew M Pardoll. The blockade of immune checkpoints in cancer immunotherapy. *Nat Rev Cancer*, 12(4):252–264, apr 2012.

[150] Sabrina Ceeraz, Elizabeth C Nowak, Christopher M Burns, and Randolph J Noelle. Immune checkpoint receptors in regulating immune reactivity in rheumatic disease. *Arthritis Research & Therapy*, 16:469, oct 2014.

[151] Abdul K. Abbas, Andrew H.H. Lichtman, and Pillai Shiv. *Basic Immunology: Functions and Disorders of the Immune System*. Elsevier Saunders, Philadelphia, PA, 4th edition, 2014.

[152] Frederick O Stephens and Karl Reinhard Aigner. *Basics of Oncology*. Springer-Verlag Berlin Heidelberg, Heidelberg, 1st edition, 2009.

[153] Tong Seng Lim, Valerie Chew, Je Lin Sieow, Siting Goh, Joe Poh-Sheng Yeong, Ai Ling Soon, and Paola Ricciardi-Castagnoli. PD-1 expression on dendritic cells suppresses CD8(+) T cell function and antitumor immunity. *Oncoimmunology*, 5(3):e1085146, mar 2016.

[154] Neil L Berinstein, Mohan Karkada, Michael A Morse, John J Nemunaitis, Gurkamal Chatta, Howard Kaufman, Kunle Odunsi, Rita Nigam, Leeladhar Sammatur, Lisa D MacDonald, Genevieve M Weir, Marianne M Stanford, and Marc Mansour. First-in-man application of a novel therapeutic cancer vaccine formulation with the capacity to induce multi-functional T cell responses in ovarian, breast and prostate cancer patients. *Journal of Translational Medicine*, 10:156, aug 2012.

[155] Sunita Awate, Lorne A Babiuk, and George Mutwiri. Mechanisms of Action of Adjuvants. *Frontiers in Immunology*, 4:114, may 2013.

[156] S. A. Patterson, S D Beyea, and C V Bowen. FMRI using high flip-angle alternating steady state balanced SSFP supported by Monte Carlo studies. In *ISMRM 19th Meeting and Scientific Exhibition*, page 3112, Montreal, QC, 2011.

[157] J A Rioux, C V Bowen, and VG Kiselev. Relaxation with Diffusion near Magnetic Particles and Cells: Analytical Description and Experiment. In *ISMRM 20th Meeting and Scientific Exhibition*, page 1712, Melbourne, AUS, 2012.

[158] James A Rioux. *Quantitative Magnetic Resonance Imaging of Cellular Density With TurboSPI*. PhD thesis, Dalhousie, 2012.

[159] V.G. Kiselev and S. Posse. Analytical model of susceptibility-induced MR signal dephasing: Effect of diffusion in a microvascular network. *Magnetic Resonance in Medicine*, 41(3):499–509, mar 1999.

[160] Malvin H. Kalos and Paula A. Whitlock. *Monte Carlo methods*. Wiley-Blackwell, 2008.

[161] David P. Landau and Kurt Binder. *A guide to Monte Carlo simulations in statistical physics*. Cambridge University Press, 2009.

[162] Robert Weisskoff, Chun S Zuo, Jerrold L Boxerman, and Bruce R Rosen. Microscopic susceptibility variation and transverse relaxation: Theory and experiment. *Magnetic Resonance in Medicine*, 31(6):601–610, jun 1994.

[163] Dmitriy A Yablonskiy and E Mark Haacke. Theory of NMR signal behavior in magnetically inhomogeneous tissues: The static dephasing regime. *Magnetic Resonance in Medicine*, 32(6):749–763, dec 1994.

[164] Jerrold L Boxerman, Leena M Hamberg, Bruce R Rosen, and Robert M Weisskoff. Mr contrast due to intravascular magnetic susceptibility perturbations. *Magnetic Resonance in Medicine*, 34(4):555–566, oct 1995.

[165] C Richard Fisel, Jerome L Ackerman, Richard B Buxton, Leoncio Garrido, John W Belliveau, Bruce R Rosen, and Thomas J Brady. MR Contrast Due to Microscopically Heterogeneous Magnetic Susceptibility: Numerical Simulations and Applications to Cerebral Physiology. *Magnetic Resonance in Medicine*, 17(2):336–347, feb 1991.

[166] Peter Hardy and R Mark Henkelman. On the Transverse relaxation rate enhancement induced by diffusion of spins through inhomogeneous fields. *Magnetic Resonance in Medicine*, 17(2):348–356, feb 1991.

[167] Robert N Muller, Pierre Gillis, Francis Moiny, and Alain Roch. Transverse relaxivity of particulate MRI contrast media: From theories to experiments. *Magnetic Resonance in Medicine*, 22(2):178–182, dec 1991.